AFRL-AFOSR-VA-TR-2021-0016

NANOSCALE EXCITON-MECHANICAL SYSTEMS (NEXMS)

Deotare, Parag
REGENTS OF THE UNIVERSITY OF MICHIGAN
230 W 41ST STREET FL 7
NEW YORK, NY, 48109-1340
US

02/18/2021
Final Technical Report

Air Force Research Laboratory
Air Force Office of Scientific Research
Arlington, Virginia 22203
Air Force Materiel Command

REPORT DOCUMENTATION PAGE

Form Approved
OMB No. 0704-0188

1. REPORT DATE *(DD-MM-YYYY)*	**2. REPORT TYPE**	**3. DATES COVERED** *(From - To)*
18-02-2021	Final	15 May 2017 - 31 Aug 2020

4. TITLE AND SUBTITLE
NANOSCALE EXCITON-MECHANICAL SYSTEMS (NEXMS)

5a. CONTRACT NUMBER

5b. GRANT NUMBER
FA9550-17-1-0208

5c. PROGRAM ELEMENT NUMBER

6. AUTHOR(S)
Parag Deotare

5d. PROJECT NUMBER

5e. TASK NUMBER

5f. WORK UNIT NUMBER

7. PERFORMING ORGANIZATION NAME(S) AND ADDRESS(ES)
REGENTS OF THE UNIVERSITY OF MICHIGAN
230 W 41ST STREET FL 7
NEW YORK, NY 48109-1340
US

8. PERFORMING ORGANIZATION REPORT NUMBER

9. SPONSORING/MONITORING AGENCY NAME(S) AND ADDRESS(ES)
AF Office of Scientific Research
875 N. Randolph St. Room 3112
Arlington, VA 22203

10. SPONSOR/MONITOR'S ACRONYM(S)
AFRL/AFOSR RTB2

11. SPONSOR/MONITOR'S REPORT NUMBER(S)
AFRL-AFOSR-VA-TR-2021-0016

12. DISTRIBUTION/AVAILABILITY STATEMENT
A Distribution Unlimited: PB Public Release

13. SUPPLEMENTARY NOTES

14. ABSTRACT
The kernel of the work was to instigate progress towards our understanding of exciton with mechanics. The report is divided into five chapters. The first two chapter describe our findings related to transport in organic and inorganic semiconductors under static strain. Chapter 3 describes the extension of the understanding developed in Chapter 1 and 2 to dynamic strain. Chapter 4 describes the exciton transfer and transport at hybrid organic/inorganic interface. Such hybrid interfaces have the potential to overcome the poor diffusivity of amorphous organic semiconductor thin films and are a viable solution to achieve strain assisted transport. Finally, we describe some potential application based on the fundamental understanding and material platform that were developed under this program. We believe that the results from this work will not only influence current excitonic research but also provide important groundwork for next generation optoexcitonic devices.

15. SUBJECT TERMS

16. SECURITY CLASSIFICATION OF:			**17. LIMITATION OF ABSTRACT**	**18. NUMBER OF PAGES**	**19a. NAME OF RESPONSIBLE PERSON**
a. REPORT	**b. ABSTRACT**	**c. THIS PAGE**			KENNETH CASTER
U	U	U	UU	69	**19b. TELEPHONE NUMBER** *(Include area code)* 0000 0000

NANOSCALE EXCITON-MECHANICAL SYSTEMS (NEXMS)

16RT1256, Final Report 15th May 2017 – 31st August 2020

Summary of Achievements under the AFOSR Young Investigator Program:

- 13 journal manuscript expected (eight published, one accepted, one under review, and three under preparation).
- 2 patents filled.
- 1 book chapter under preparation (Elsevier).
- 15 conference invited and contributed talks.
- Supported three graduate students over three years.

IMPORTANT RESEARCH ACHIEVEMENTS

- First comprehensive report on effect of doping (guest-host system) on strain sensitivity of excitonic orientation polarizability.
- Resolved the large discrepancy in reported value of Young's modulus of organic thin films by introducing a non-destructive technique based on excitons.
- First direct visualization of exciton transport (spatial visualization) under strain gradient.
- Developed excitonic bar code using strain engineering.
- First reported study on FRET energy transfer across a hybrid organic/transition metal dichalcogenide (TMD) interface.
- First systematic study of the nonlinear ultrafast transport of hybrid charge transfer excitons (HCTEs) at organic/TMD hybrid interfaces.
- Provided insight into the phonon bottleneck that results in prolonged (>100 ps) *hot* HCTE transport.
- The results show that translational mass of HCTE is smaller than excitons in individual material system.
- Hybrid interfaces can overcome the poor diffusivity of amorphous organic semiconductor thin films and are a viable solution to achieve strain assisted transport.
- Utilized efficient energy transfer from organic to inorganic semiconductor to introduce a hybrid platform for sensitive photodetectors (UV – visible).

Table of Contents

The kernel of the work was to instigate progress towards our understanding of exciton with mechanics. The report is divided into five chapters. The first two chapter describe our findings related to transport in organic and inorganic semiconductors under static strain. Chapter 3 describes the extension of the understanding developed in Chapter 1 and 2 to dynamic strain. Chapter 4 describes the exciton transfer and transport at hybrid organic/inorganic interface. Such hybrid interfaces have the potential to overcome the poor diffusivity of amorphous organic semiconductor thin films and are a viable solution to achieve strain assisted transport. Finally, we describe some potential application based on the fundamental understanding and material platform that were developed under this program. We believe that the results from this work will not only influence current excitonic research but also provide important groundwork for next generation optoexcitonic devices.

1 Strain effects on excitonic properties in organic semiconductors:

Knowledge of the bathochromatic shift in energy levels due to external strain on potential excitonic materials is essential to achieve interactions between excitonic energy states and mechanical energy states. The two materials under study i.e. organic thin films and TMD monolayers have physcially different morphologies and hence require different approaches to study the effect of strain. In this section, we report the results for organic semiconductors.

Over time, various techniques and methods have been employed to study strain effect of organic thin films on exciton dynamics. We explored two approaches for studying organic thin films. The first approach was based on utilizing the internal stress in thin films to buckle suspended microbeams to achieve controlled strain in overlying thin films. The second approach was using micro electromechanical systems (MEMS) to induce tunable strain in a thin film.

In the first approach, we use the residual stress in silicon dioxide (SiO_2) thin films to generate controlled axial strain on an overlying organic thin film. Residual stress is generated due to differential thermal expansion of the substrate and the thin film during the growth phase. The microbeams were patterned on

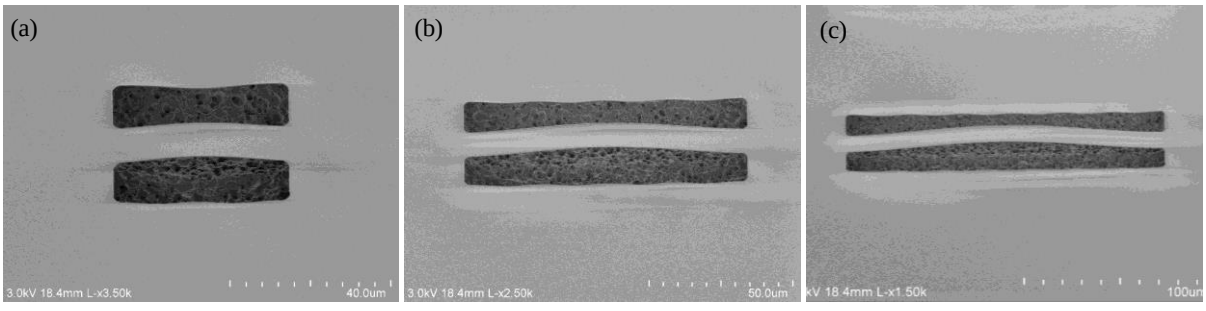

Figure 1: SEM images of self-strained silicon oxide beams after release using 3 cycles of XeF_2 etching for different beam lengths: (a) 40 um; (b) 90 um; (c) 160 um.

the substrates using optical lithography, followed by reactive ion etching and released from the substrate using a gas-phase etching process, followed by the evaporation of the organic thin film. SEM images of some of the released microbeams are shown in Figure 1. The axial strain along the microbeam axis was measured using white light interferometry and polynomial fitting of the out-of-plane deflection of the microbeam. The 2D surface map of a representative microbeam obtained using white light interferometry is shown in Figure 2(a). The maximum out-of-plane deflection and tensile strain at the point of maximum deflection for different beam lengths are shown in Figure 2(b). Although, out-of-plane microbeam deflection increases as the beam length increases, the resulting axial strain at the maximum deflection point decreases with beam length. The measurements show that the microbeam geometry can generate an axial strain of about 0.9% at the position of maximum deflection. In addition, the generated axial strain is lower than the strain applied in most bucking based methods as well as the reported yield point for small-molecule

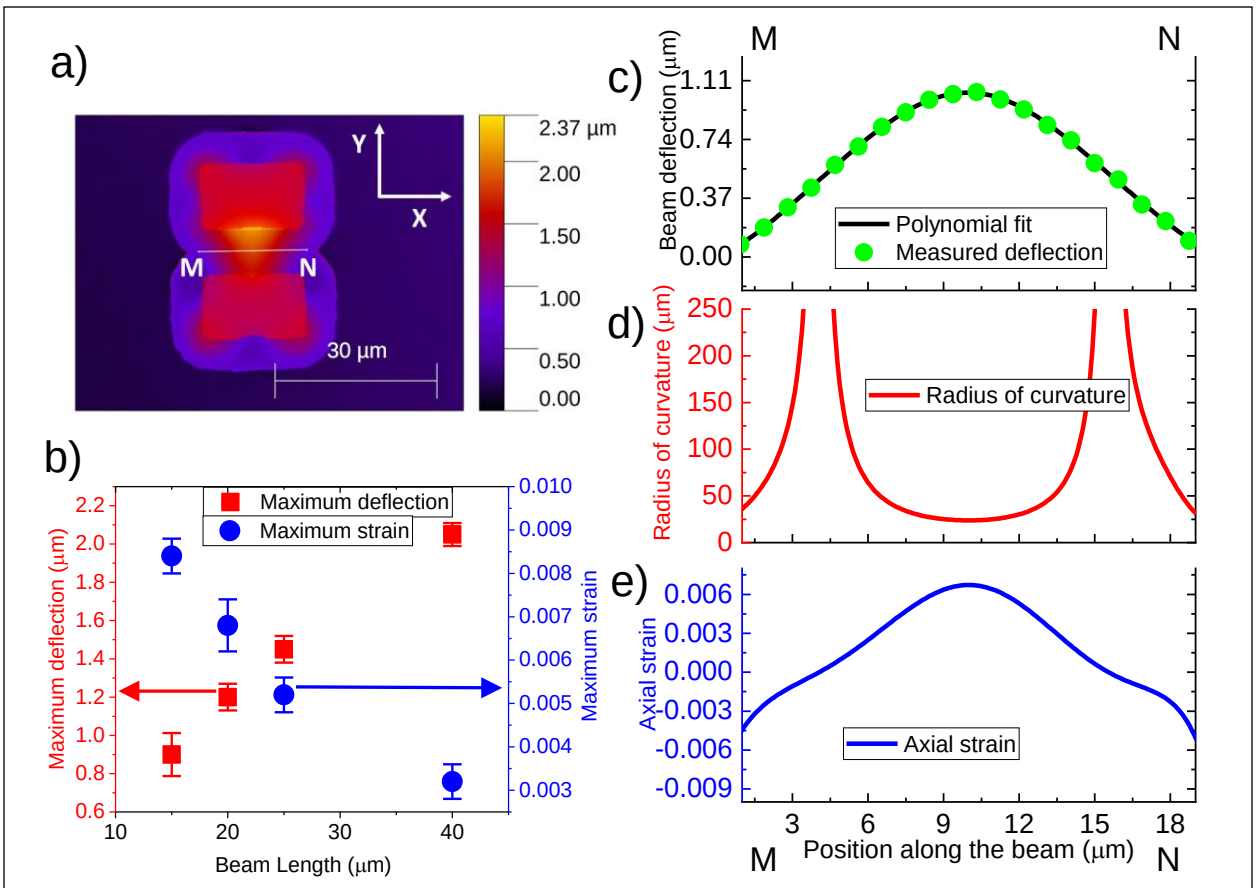

Figure 2: Axial strain on buckled SiO_2 microbeam: (a) Surface profile of a doubly supported SiO_2 microbeam released by gas-phase XeF_2 etching step. The surface profile is extracted using non-contact white light interferometry. (b) Maximum deflection of buckled microbeam, and the corresponding axial strain measured at the maximum defection point for different beam lengths. The axial strain at maximum deflection point decreases with increased beam length. (c) Deflection profile of the buckled microbeam shown in (a), along a linear section labeled M-N, through the middle of the buckled beam. The figure also shows a polynomial fit of the extracted surface profile along the linear section. (d) Radius of curvature extracted from the fitted deflection profile. (e) Axial strain profile calculated from the radius of curvature using the formulation discussed in supplementary information (section 1). The axial strain at the center of the buckled microbeam can reach as high as 0.7%.

organic materials [1–4]. Since the maximum strain applied in this work is within the yield limit of the thin film under study, the mechanical properties of the organic thin-film in this work are expected to be governed by the linear regime of the stress-strain relationship. We note that in addition of the generated strain being lower than the yield point of the thin film, we estimate the axial tensile strain to be insufficient to cause any change in the molecular bonds (please refer to supplementary information section 5 for more discussion). Figure 2(c) – (e) shows the out-of-plane deflection (obtained from 2D surface map and polynomial fitting), the radius of curvature and the axial tensile strain respectively, along the linear section labeled M – N in Figure 2(a).

We choose to work with Tris-(8-hydroxyquinoline) aluminum (Alq_3) and 4-(Dicyanomethylene)-2-methyl-6-(4-dimethylaminostyryl)-4H-pyran (DCM) as a representative of a guest: host system of organic semiconductors. Alq_3 is widely used as an electron transport layer as well as an active emission layer in organic light emitting diodes (OLEDs)[5]. Further, the emission wavelength and the electroluminescence efficiency of Alq_3 based OLEDs can be modulated by introducing small molecule dopant materials in specific concentrations and thereby changing the non-radiative energy transfer from host Alq_3 molecules to guest dopant molecules[6]. In this regard, DCM has been widely used as a luminescent red dopant in Alq_3 host matrix due to high Förster energy transfer efficiency[7, 8].

The axial strain on the SiO_2 microbeam increases gradually from the clamped ends towards the center where the deflection is maximum. Therefore, the local molecular density and the local electric field decrease along the beam towards the maximum deflection position. We performed PL measurements on microbeams with two different lengths – 15 μm and 20 μm. A 450 nm continuous wave (CW) excitation laser was used to excite only the guest DCM molecules [9, 10]. Figure 3(a) shows the axial tensile strain along a 15 μm long beam (width 8 μm) on which PL measurements are performed. Figure 3(b) shows the PL centroid extracted from our measurements along the microbeam axis. The PL centroid profile shows a gradual blue-shift as we approach the position of maximum deflection from the clamped end of the beam. We observe a PL centroid shift of about 5-6 nm for generated tensile strain of about 0.9%. The observed blue-shift is consistent with solid-state solvation effect in solid state organic thin films. Figure 3(c) shows the normalized PL intensity spectrum measured at different positions along the microbeam in 1 μm steps which also shows a gradual blueshift from the clamped end of the beam towards the maximum deflection position at the center. Figure 3(d) shows the normalized PL spectrum at three different positions of the beam labeled as - positions M and N, where the extracted tensile strain on the beam is found to be zero and position P, where the tensile strain is maximum. At zeros strain positions (position M and N in Figure 3(c)) on the microbeam, there appears to be no spectral shift in the normalized PL profile. However, at the position of maximum tensile strain (position P in Figure 3(c)) a clear blueshift is observed with respect to the zero strain positions.

The solvatochromic spectral shift due to solute-solvent interaction in a dielectric medium is generally represented by the Lippert- Mataga equation[11, 12]:

$$\upsilon_a - \upsilon_f = \frac{2}{hc}\left(\frac{\varepsilon - 1}{2\varepsilon + 1} - \frac{n^2 - 1}{2n^2 + 1}\right)\frac{(\mu_E - \mu_G)^2}{a^3} + C \qquad (1.1)$$

Here, υ_a and υ_f refer to the peak absorption and emission wavenumbers of solute molecule in cm^{-1}, ε and n refer to the dielectric constant and refractive index of the surrounding solid-state solvent medium respectively, h and c refer to the Planck's constant and the speed of light respectively, μ_E and μ_G refer to the dipole moment of the solute molecules in the excited and ground-state respectively, a is the radius of the cavity from Onsager reaction field theory[13], and C refers to a constant that represents the unperturbed spectral shift of the solute emission. The term $\frac{\varepsilon-1}{2\varepsilon+1} - \frac{n^2-1}{2n^2+1}$ generally referred to as the orientational polarizability[14], represents the local dielectric polarization of the medium. The first term $\frac{\varepsilon-1}{2\varepsilon+1}$ represents

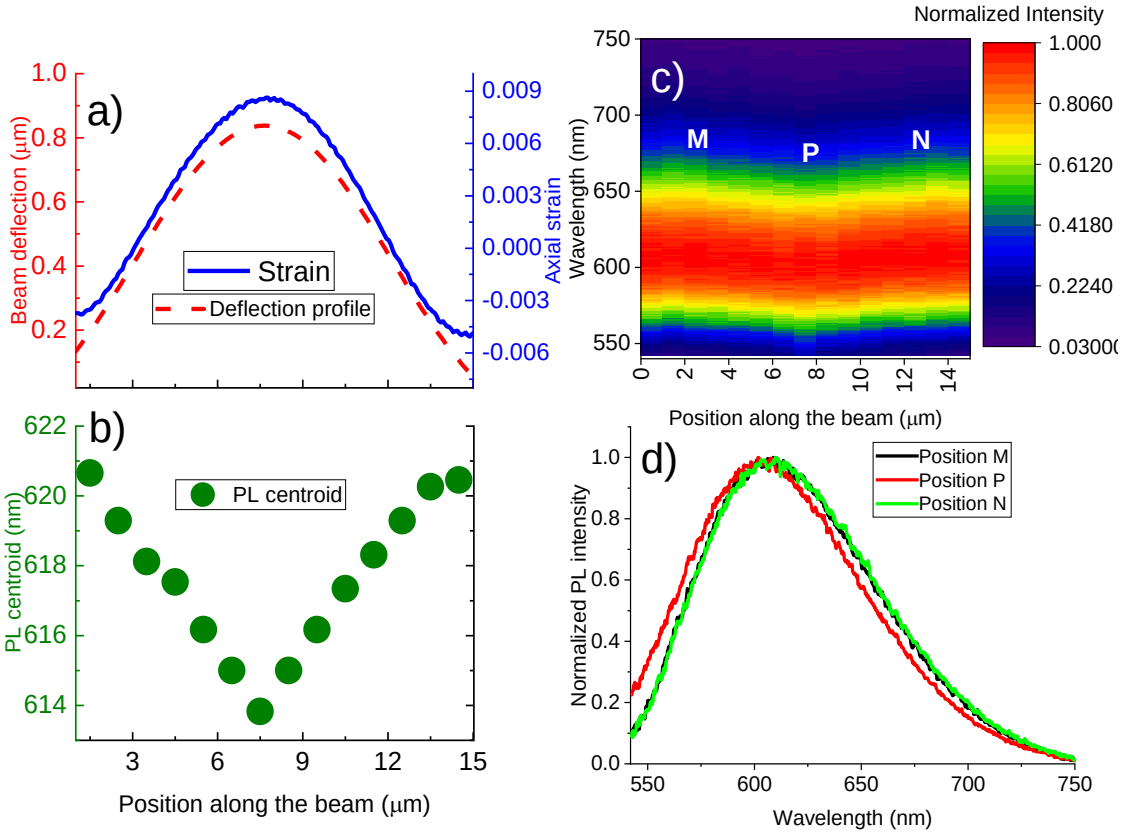

Figure 3: Solid state solvation in strained Alq_3:DCM thin film: (a) Axial strain profile extracted from out-of-plane deflection of a 15 μm microbeam on which the PL measurement is performed. 2D surface map of the beam and the deflection profile can be found in the supporting information (Figure S8). (b) Centroid of the PL spectra extracted from measurements on the strained organic film along the beam axis. (c) Normalized PL spectra at different positions along the beam. With increased tensile strain towards the center of the beam, we observed a blueshift in the emission spectrum. (d) Normalized PL spectrum at three different positions along the beam- zero strain positions: position M and N, and maximum strain position at the center of the beam: position P. With respect to the zero strain positions on the beam, a blue-shift is observed in the normalized PL spectrum at the position of maximum tensile strain.

the effect on Stokes shift due to both electronic and molecular reorientation of the solvent dipoles around the excited solute molecules. On the other hand, the second term $\frac{n^2-1}{2n^2+1}$represents the high-frequency response due to electronic reorientation. Therefore, the difference between the two terms accounts for the net dielectric polarization due to molecular reorientation in a solute-solvent medium. In solid-state doped thin films, orientational polarizability increases as the concentration of polar guest molecules in a relatively non- polar background host matrix is increased.

From the measured peak PL emission, one can extract the local orientational polarization (Δf) along the strained thin films for different DCM doping concentrations. We rewrite equation. (1.1) as:

$$\upsilon_a - \upsilon_f = m\Delta f + C \qquad (1.2)$$

where,

$$m = \frac{2}{hc}\frac{(\mu_E - \mu_G)^2}{a^3} \qquad (1.3)$$

$$\Delta f = \frac{\varepsilon - 1}{2\varepsilon + 1} - \frac{n^2 - 1}{2n^2 + 1} \qquad (1.4)$$

We use the reported values of m and C of $7.94X10^3$ cm^{-1} and $2.74X10^3$ cm^{-1} respectively[15, 16] and the DCM absorption peak wavelength of 480 nm[17] to extract the orientational polarizability based on the measured PL emission peaks. We assume a negligible change in the absorption spectrum of DCM due to axial tension on the thin film. The solvatochromic shift due to molecular reorientation takes place over a long time scale (~10^{-9} s) compared to light absorption(~10^{-15} s), justifying the assumption[18]. The orientational polarizability decreases gradually from the zero-strain position and reaches its minimum value at the maximum tensile

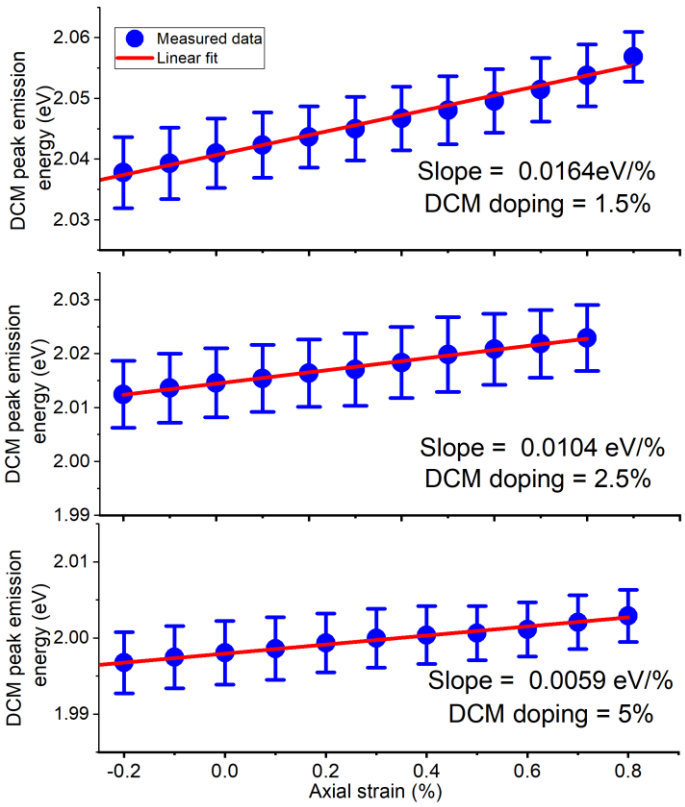

Figure 4: Linear fit of DCM peak emission energy with axial strain at for different DCM doping. (a) 1.5%; (b) 2.5%; (c) 5% DCM doping concentrations. Even though DCM peak emission energy shift consistently follows a linear relationship with axial strain, the range of peak emission energy modulation under strain decreases with DCM doping. The error bar in the figures represents the range of DCM peak emission energies from different samples.

strain position on the microbeam. Based on the results, ~9% change in the orientational polarization was estimated under axial tension of 0.9 %.

From our measurement, we observe a linear relationship between the peak DCM emission energy and the axial tensile strain for different DCM doping concentrations as shown in Figure 4. However, the rate of a solvatochromic shift under strain was different at different DCM doping concentrations. We observed the highest slope of 0.016 eV/% in the 1.5 % doped film, reducing to 0.006 eV/% for 5% doped film. To understand the relationship of DCM peak emission energy to external axial strain, we use Claussius-Mossoti relation that relates the dielectric response of a homogeneous medium, $\frac{\varepsilon-1}{\varepsilon+2}$with molecular polarizability, α as[19]:

$$\frac{\varepsilon-1}{\varepsilon+2}=\frac{n\alpha}{3\varepsilon_0} \tag{1.5}$$

Here, *n* refers to the molecular density of the medium (*N/V* where we assume the number of molecules dispersed in volume *V* is *N*), and ε_0 refers to the free space dielectric constant. Since the high-frequency refractive index is not affected by axial tension on the thin film, any effect on the dielectric polarizability under external strain must be due to changes in the dielectric function, $\Delta f(\varepsilon)=\frac{\varepsilon-1}{2\varepsilon+1}$.

Under strain, the thin film undergoes local volumetric change (Δv) that modulates the molecular density at a specific doping level. We estimate the volumetric change under axial tension by considering a small volumetric segment of the thin film as shown in Figure 5(a). The length, width, and height of the segment are presented as X, Y, and Z. The out-of-plane deflection of the microbeams elongates the thin-film uniaxially (along the *x*-direction in Figure 5(a)) and therefore, due to the Poisson effect, the thin film is compressed along *y* and *z* directions. We represent the elongation of the thin film along the microbeam axis as Δx and the orthogonal compression as Δy and Δz. Defining the Poisson ratio of the thin film as ν, the orthogonal compressions can be written as $\Delta y=-\nu Y\varepsilon_x$and $\Delta z=-\nu Z\varepsilon_x$.

Therefore, under uniaxial strain, the volumetric change in the thin film (Δv) due to small axial elongation under strain, can be related to the initial volume, *V* as[20]*:*

$$V+\Delta v=XYZ(1+\varepsilon_x)(1-\nu\varepsilon_x)^2$$
$$\Rightarrow 1+\frac{\Delta v}{V}=(1+\varepsilon_x)(1-2\nu\varepsilon_x)+\nu^2\varepsilon_x^2(1+\varepsilon_x)$$
$$\Rightarrow \frac{\Delta v}{V}=(1-2\nu)\varepsilon_x$$

To the first order, the dielectric polarizability under tensile strain, $\Delta f(\varepsilon)$ is related to the volumetric change by the following linear relationship:

$$\Delta f(\varepsilon) \approx \frac{N\alpha}{3\varepsilon_0(V+\Delta v)} \approx \frac{N\alpha}{3\varepsilon_0 V(1+\frac{\Delta v}{V})} \approx \frac{N\alpha}{3\varepsilon_0 V}(1-\frac{\Delta v}{V}) \approx M(1-(1-2\nu)\varepsilon_x) \quad (1.6)$$

where M is a proportionality constant. Therefore, for a specific DCM doping, under small volumetric deformation, the local dielectric property in the thin film is linearly proportional to the axial strain. This leads to a linear shift in solvatochromic energy in the DCM emission under mechanical strain.

Strain tuned dielectric polarization at different DCM doping

We define the strain sensitivity of orientational polarization as the fractional change in orientational polarization per unit axial strain i.e. $\frac{\Delta f(\varepsilon)-\Delta f(0)}{\Delta f(0)}$where $\Delta f(0)$ is the orientational polarization of an unstrained thin film. Figure 5(b) shows the estimated strain sensitivity of orientational polarization of Alq_3: DCM thin films at different DCM doping concentrations. As the DCM doping increases, orientational polarizability and the resulting solvatochromic shift in the thin film becomes less sensitive to the external uniaxial strain.

The observed trend in strain sensitivity of orientational polarization for different doping concentrations can be explained by the physical origin of the solvatochromic shift in the host: guest Alq_3: DCM system. At very low concentrations, the emission properties of organic fluorophores are strongly affected by the electric field from surrounding fluorophores in a host: guest medium[21]. The increase in DCM doping reduces the intermolecular separation between DCM dipoles, enhances the dielectric polarization and the

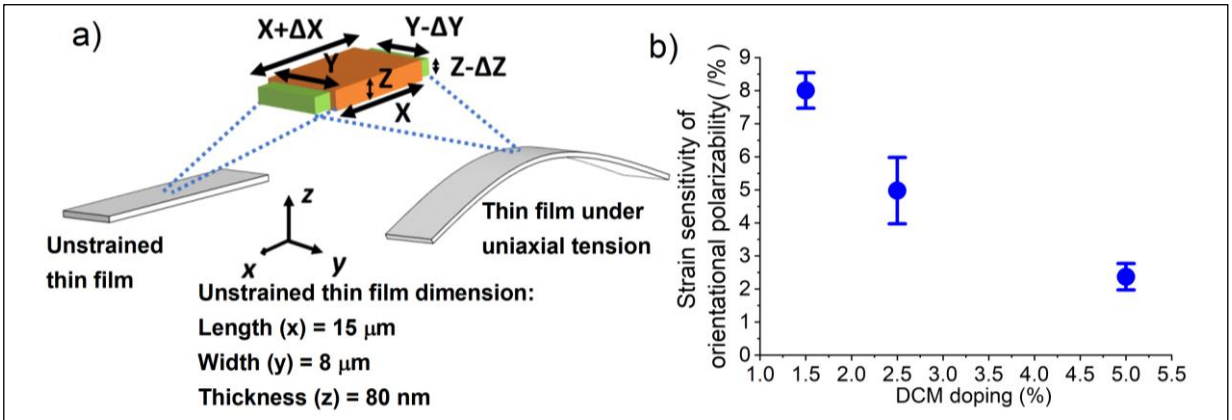

Figure 5: (a) Simple schematic representation of an organic thin film under axial tensile strain. While the dimensions of the unstrained thin film are mentioned in the figure, the figure is not drawn to scale. (b) Strain sensitivity of the orientational polarization in Alq_3: DCM host: guest medium at different DCM doping. The error bars represent the range of strain sensitivity extracted from PL measurements on microbeams at different DCM doping.

net local field on a molecular dipole. This leads to an increase in the energy required for molecular orientation after photoexcitation and a stronger stabilization of the excited state. In our experiment, the mechanical properties of the system are dominated by the host Alq_3 matrix. Therefore, under uniaxial tensile strain, the intermolecular distance between neighboring DCM molecules dispersed in Alq_3 matrix increases. Besides, as the thin film is uniaxially elongated, compression due to the Poisson effect also reduces intermolecular distance orthogonal to the elongation axis. These two mechanisms result in a net molecular density and net dielectric polarizability in the medium that governs the energy shift due to solvatochromism. At low DCM doping level, due to low molecular density and large intermolecular distance, uniaxial elongation of the thin film leads to a reduction in net molecular density and reduces the net local electric field on a molecular dipole. Therefore, we observe a larger modulation of the orientational polarizability under strain at lower DCM doping concentration. . However, as the DCM doping increases, due to reduced intermolecular separation, orthogonal compression of the thin film due to the Poisson effect counteracts the change in orientational polarization due to elongation under axial tensile strain. This results in lower net change in orientation polarization, thereby reducing the strain sensitivity. We note that aggregation of molecules at high concentrations could also contribute to the reduction in the sensitivity. To confirm this, we performed PL measurements on 5% DCM doped compressively strained organic thin films and observed a similar trend in the orientational polarizability and peak DCM emission. Thus, we conclude that the observed change in the orientational polarizability (and in turn dielectric polarizability) is indeed due external strain and has negligible contribution from molecular aggregation. Our observation of solvatochromic shift under strain, therefore, reveals the critical role of molecular doping in the modulation of dielectric polarizability of host: guest medium under external mechanics.

Our findings show that the spectral shift due to solvation at different doping concentrations of the guest molecule follows a linear relationship with applied strain. From the solvatochromic spectral shift, using Lippert- Mataga equation we show that the dielectric polarizability of the host: guest medium shows greater sensitivity at low guest molecule doping. As the dielectric nature of the medium is externally increased by guest molecular doping, short-range intermolecular interactions strongly dominate the solvation properties in the medium and the dielectric properties of the medium become less sensitive to external mechanical stimuli. The reported results can greatly aid in the design of wearable and large-scale flexible optoelectronic devices based on the excitonic modulation under external mechanical stimuli.

Determination of Young's Modulus Using Solvatochromic Shift:

The elastic modulus of the organic thin film can be extracted by fitting a model based on solid-state solvation with the observed shift in the photoluminescence (PL) spectrum of the strained organic thin films. We believe that estimation of mechanical properties of such a representative system using an optical non-

contact approach could be helpful for flexible optoelectronic device applications. From our PL measurements along the self-strained microbeam, we can formulate a relationship between the change in the transition energy of the DCM molecules with applied tensile strain. According to the Ooshika-Lippert-Mataga (OLM) framework, it is possible to relate the change in transition energy during fluorescence, ΔE of solute molecules in a polarizable solvent using the following equation[12, 16, 22]:

$$\Delta E = -\frac{1}{a^3}\Delta\vec{\mu}.(f(\varepsilon)\vec{\mu}_e + f(n^2)\vec{\mu}_g) \quad (1.7)$$

where the solute molecule is assumed to be within a spherical cavity of radius 'a'. $\vec{\mu}_e$ and $\vec{\mu}_g$ refers to excited state and ground-state dipole moment of the solute molecule and $\Delta\vec{\mu} = \vec{\mu}_g - \vec{\mu}_e$. In addition, $f(\varepsilon)$ represents the low-frequency nuclear reorientation term that corresponds to the time scale of the excited state lifetime. $f(n^2)$ refers to the high-frequency electronic reorientation term that remains fairly unchanged with solvent polarizability and changes over the same time scale as photon absorption and emission process[23].

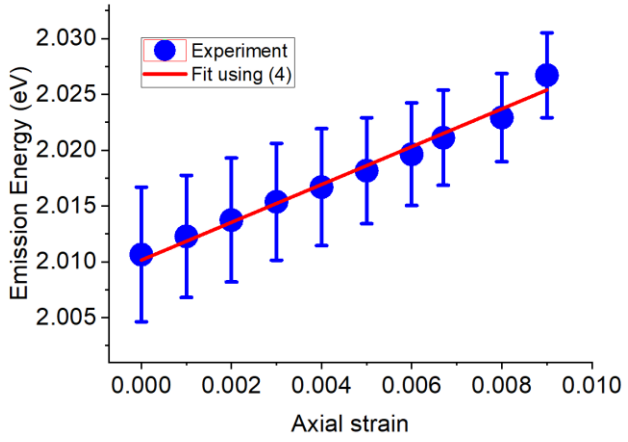

Figure 6: Fitting of the DCM emission energy with error bar, calculated from the centroid of the measured PL spectra as a function of the axial tensile strain or equivalent change in local dielectric environment along buckled SiO_2 microbeam. Since tensile strain reduces local molecular density along the microbeam, a blueshift is observed in the DCM emission energy. Here, the error bar represents the total range of DCM emission energy calculated from PL measurements along different microbeam samples. The filled circles represent the median value of the calculated DCM emission energies under different tensile strain along the microbeam.

Neglecting the high-frequency terms and following the principal formulation described in Madigan et al.[23], we fit the change in transition energy of the DCM molecules obtained from our PL measurements along the beam with a linear relationship:

$$E_{PL} = B\varepsilon + D \quad (1.8)$$

Here, B and D are fitting parameters and εrepresents the tensile strain along the microbeam, and E_{PL}denotes the PL emission energy from DCM molecules. The fitting parameter D effectively corresponds to the transition energy at zero strain position along the microbeam. The fitting parameter B, on the other hand, corresponds to the changes in the local dielectric environment or polarizability of the surrounding amorphous medium in response to the tensile strain along the beam. From the linear fit shown in Figure 6, we extract the values of B and D as 1.69±0.09 eV and 2.01±5.23e-4 eV respectively. The results shown in Figure 6, correspond to a 1.5% DCM doped thin film.

Since equations (1.7) and (1.8) represent the modulation of emission energy of an organic fluorophore under axial strain below yield point, we can equate the absolute value of the slopes of these equations to extract Young's modulus as:

$$Y = \frac{B}{\alpha A} \qquad (1.9)$$

Using the values of parameters A= 0.55 eV and α = 1.1±0.5 GPa^{-1} reported in literature[24] and using the value of parameter B extracted from our measurements, we estimate the Young's modulus to be 2.81±1.28 GPa.

Microelectromechanical Systems (MEMS) for tunable strain:

We further verify the estimated value by dynamically tuning the tensile strain on the organic thin film using a MEMS device fabricated on a low stress, low-pressure chemical vapor deposited (LPCVD) silicon nitride (Si_3N_4) platform. Since the axial strain generated on the self-strained silicon oxide microbeams changes gradually along the beam axis, the MEMS platform accurately portray the dynamic behavior of a strained organic thin film. We numerically modeled the dynamic actuation behavior of the MEMS thin film membrane device structure under applied electrostatic force using COMSOL Multiphysics[25] and extracted the device dimensions for fabrication.

Figure 7(a) shows the SEM micrograph of a representative MEMS membrane device fabricated on low-stress Si_3N_4. The fabrication process can be found in the published work. A higher magnification SEM micrograph of the area of the device structure where axial tensile strain is generated is also shown. As the proof mass structure deflects downward due to electrostatic actuation, tensile strain is generated along the microbeams AA´ and BB´ . Under electrostatic actuation, each of the microbeams AA´ and BB´ acts as a cantilever beam under point load applied at the free end. For a cantilever beam under point load, the maximum axial tensile strain is generated at the fixed end[26]. The fixed end position of beam AA´ is marked as F. To determine the position of maximum tensile strain along the beam (the fixed end position of the microbeam), we performed PL scan at 1 µm steps along the microbeam under applied electrical bias of 0 V to 150 V and extracted the DCM emission energy from the centroid of the measured PL spectra. From the evolution of DCM emission energy with applied bias voltage, measured at different positions along the microbeam, we estimated the position of the maximum tensile strain. Figure 7(b) shows a schematic drawing of the MEMS thin film device structure (not drawn to scale). The electrostatic actuation of the proof mass generates axial strain (ε) along of the support beam (beam AA´ in Figure 7(a)) with the maximum strain generated at the fixed end position (position F in Figure 7(a)).

Figure 7(c) shows the centroid of the measured PL spectra (1.5 % DCM doped thin film) at the position of the maximum tensile strain on the microbeam at different applied voltages along with the axial tensile strain simulated using COMSOL Multiphysics[25]. As the axial tensile strain increases with applied voltage, the PL centroid shows a gradual blueshift due to reduction in local molecular density. The dimensions extracted from fabricated devices were used for the simulation of axial tensile strain profile shown in Figure 7(c) and Figure 7(d). Upon fitting the change in emission energy of DCM molecules with simulated axial tensile strain, the values of parameters B and D were extracted to be 2.35±0.14 eV and 2.06±2.72e-4 eV respectively. Using equation (1.9), the value of elastic modulus of the thin film was estimated to be 3.88±1.78 GPa. The fitting of DCM emission energy from the measurements with simulated axial tensile strain is shown in Figure 7(d). Figure 7(e) shows the normalized PL intensity at the position of maximum tensile strain under two different applied voltages – 0V and 150V. The normalized PL intensity at 150 V applied voltage shows a clear blue shift due to tensile train.

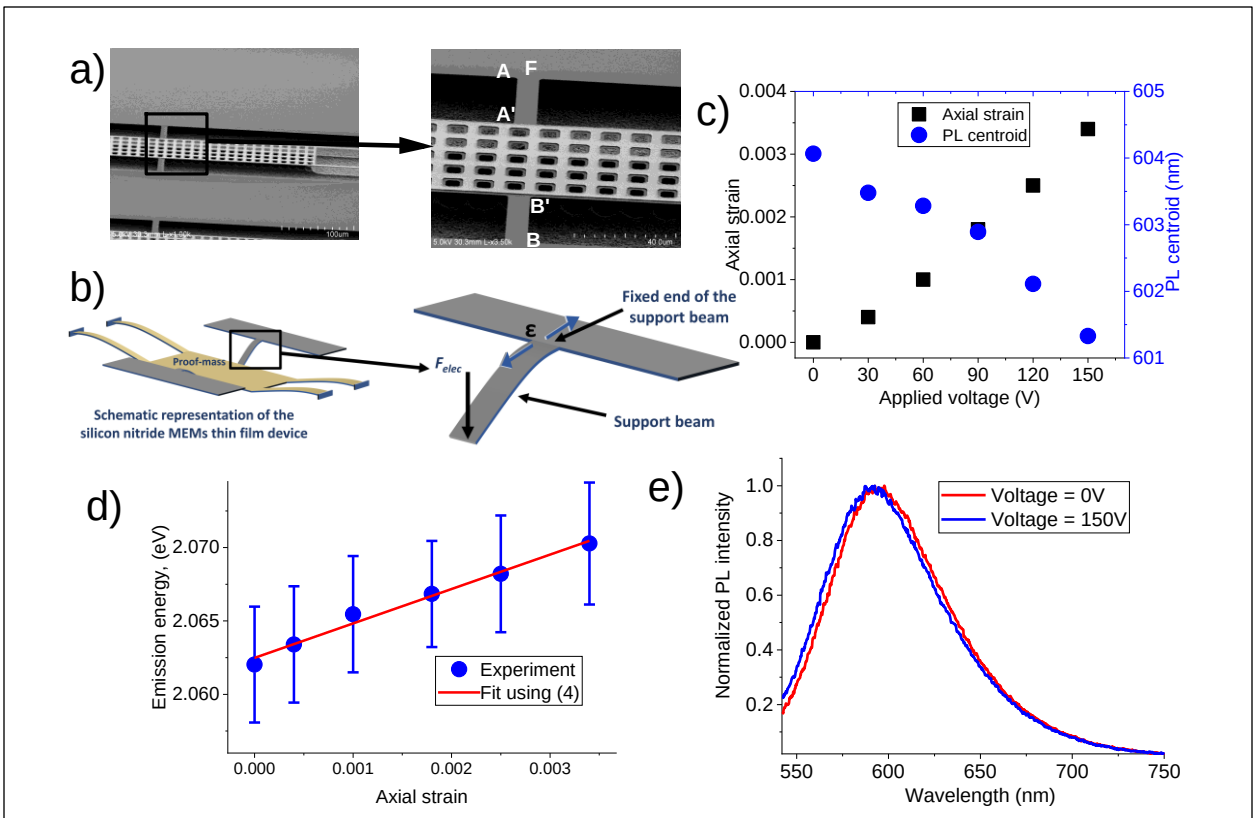

Figure 7: Dynamic strain on organic thin film using a MEMS thin film membrane actuator: (a) SEM micrograph of a representative MEMS membrane device used in this work. The higher magnification figure shows microbeams AA´ and BB´ along which axial tensile strain is generated under applied voltage. The fixed end position of microbeam AA´ is marked by F. (b) Schematic drawing of the MEMS device (not drawn to scale) under electrostatic actuation showing the position of axial strain (ε) generation. (c) Axial tensile strain at the fixed end positions from COMSOL simulation and measured PL centroid under applied voltage. The PL centroid shows a gradual blue-shift under applied voltage due to increasing axial tensile strain. (d) Fitting of DCM emission energy under applied voltage with simulated tensile strain at maximum strain position with error bar. Here error bar represents the range of DCM emission energy from PL measurement at maximum strain position. (e) Normalized PL intensity profile at the measurement position in (c) at two different applied bias voltages: 0V and 150V that shows a blueshift under applied voltage due to tensile strain.

We estimate the Young's modulus of Alq_3 thin film using two different approaches to be 2.81±1.28 GPa (self-strained SiO_2 microbeams) and 3.88±1.78 GPa (dynamic strain using Si_3N_4 MEMS devices). We attribute the uncertainties in our estimation (~45% in both the approaches) to the uncertainties in the reported value of parameter α. In the solvatochromic approach, the estimated value of Young's modulus depends on the values of parameters A and α reported in literature[23, 24]. For a fixed luminescent emitter molecule, the value of A has been reported to be identical in different solvent environments and doped thin guest: host thin films[23]. Since the value of parameter α[24] is reported to have a much wider range of uncertainty(~50%) than A[23], the results estimated using the solvatochromic approach are expected to be more strongly affected by the uncertainty in α. Therefore, large uncertainty in the reported value of parameter α leads to uncertainties in our estimation of Young's modulus. For instance, the uncertainty in Young's modulus reduces to ~ 6% without any uncertainty in α.

The value of Young's modulus extracted using the solvatochromic shift appears to be slightly higher than those reported using buckling method for Alq_3 thin film[27] although they are of the same order of magnitude. The estimated values are also in the same order of magnitude as other amorphous organic materials[2],[28]. However, the reported values are much smaller than the one reported using nano-indentation that overestimates the elastic modulus due to substrate-indenter interaction[29]. Such non-invasive approach based on local electric field properties of molecular thin films is extremely beneficial for on-chip determination of elastic properties and could be extended for extraction of other relevant mechanical properties. We note that the reported technique is generic and can be used to measure mechanical properties of other material systems, provided the parameter α used in equation (**Error! R eference source not found.**) is estimated experimentally [24], or using molecular dynamic simulation. In addition, such methods of on-chip straining are also compatible with current processing technologies and can be used to tune optical response of organic semiconductor thin films for optoelectronic and photovoltaic applications.

In summary, the use of self-strained SiO_2 microbeams and MEMS thin film devices fabricated on Si_3N_4 platform enable non-contact and hence non-destructive method to measure the mechanical properties of organic thin films by changing the local dielectric properties. The microstructures allow application of controlled tensile strain on the overlying thermally evaporated organic guest: host thin film. The resulting shift in the emission spectrum of the organic thin-film is modeled using solid-state solvation effect in doped guest: host system that takes into account the changes in local molecular density under tensile strain. From our study on the spectral tuning of the emission profile using two approaches, we have successfully extracted the Young's modulus of the organic thin film to be within 2.81-3.88 GPa. Such strain-based optical non-contact method can be used for accurately measuring the elastic modulus of organic

semiconductor thin films for flexible and wearable nanoscale devices for optoelectronic and photovoltaic applications. The method described in this work can be extremely useful for on-chip characterization of elastic properties of small molecule organic semiconductor thin films and can be extended for estimating other relevant nanoscale mechanical properties as well as precise and dynamic tuning of nanoscale exciton energy transfer in organic thin film devices.

2 Strain effect on excitonic properties in transition metal dichalcogenides (TMDs) monolayers:

TMDs have received special attention in the last decade due to their potential to enable optoelectronic devices with novel functionalities[30–32]. In addition, the ability to tune their band structures via strain along with their room-temperature stable excitonic resonances makes these materials outstanding candidates for studying exciton-mechanics effects.

Monolayer WSe_2 samples were prepared via mechanical exfoliation[33] and were transferred over SiO_2 nanopillars on a Si substrate. The resulting strain profiles on the WSe_2 monolayers were obtained by measuring the local PL spectrum across an area strained by a SiO_2 pillar. Figure 8(a) shows an optical image a WSe_2 monolayer over a ~1.5 μm diameter, ~250 nm tall SiO_2 pillar, and Figure 8(b) shows the monolayer's integrated PL spectra from the area enclosed by the square on the optical image. The PL spectra were integrated between 622 nm-881 nm since the peak intensity of WSe_2 occurs typically at around 750 nm. The integrated spectra were normalized with respect to their maximum value within the enclosed area to emphasize the effect of the pillar.

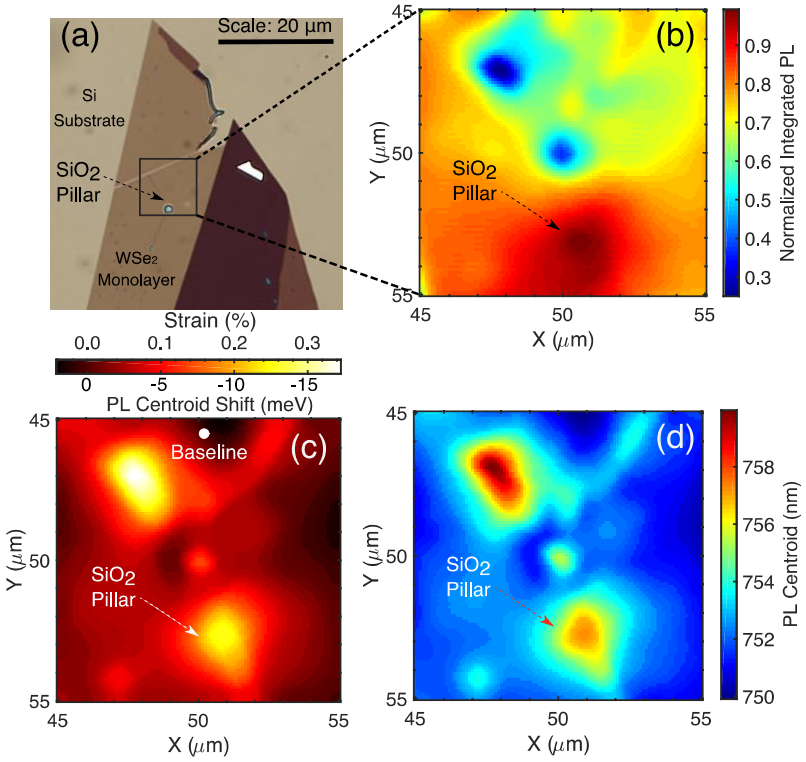

Figure 8: (a) Optical image of a WSe_2 monolayer transferred over a ~1.5 μm diameter, ~250 nm tall SiO_2 pillar on a Si substrate. (b) Normalized integrated PL spectra of the WSe_2 monolayer strained by the SiO_2 pillar. The monolayer's scanned area is enclosed by the square shown in (a). The local PL spectra were integrated between 622 nm-881 nm and they were normalized with respect to the maximum integrated PL value within the enclosed area. (c) Bandgap energy shift/strain map of the monolayer. The white dot on the strain map indicates the location of the baseline spectrum where the monolayer is assumed to be unstrained. (d) Local PL spectra's centroid map. The excitation laser used for mapping the strain field was a 532 nm, CW diode laser.

The direct bandgap of monolayer TMDs is expected to decrease (increase) linearly with tensile (compressive) strain[34] which should be evidenced by red (blue) shifts in their PL spectra. Moreover, an enhancement of their PL intensity at high tensile strain points is expected due to the funneling of excitons towards the lower bandgap energy (red-shifted) regions of the monolayer. Such an enhancement in the

WSe_2 monolayer's local PL intensity is observed in Figure 8(b) around the SiO_2 pillar, which is consistent with the funneling of excitons towards the points of highest tensile strain. The additional high strain points on the strain map shown in Figure 8(c) could be the result of substrate roughness[35] or polymer residue from the fabrication process. The strain field on the WSe_2 monolayer was estimated by calculating the shift of the local PL spectra's centroids with respect to an unstrained point on the monolayer. The spectral shifts were converted to bandgap energy shifts and strain using the sensitivity of WSe_2's direct bandgap to strain (-55 meV/%) from reference[34]. Figure 8(c) shows the WSe_2 monolayer's bandgap shift as a result of the applied strain. The white dot indicates the location of the unstrained PL spectrum baseline.

The transport of excitons on an unstrained point of the WSe_2 monolayer was visualized first to set a reference for the transport of excitons on the strained portion of the monolayer. A map of the time-dependent exciton density as a function of position was constructed using the technique from references[36, 37]. The spatial information is obtained by scanning a detector across the PL emission spot resulting from a pulsed excitation while the temporal information is obtained via time-correlated single photon counting. Figure 9(b) shows the exciton density as a function of time and position where the excitation was fixed at an unstrained point as indicated by the cross on Figure 9(a). The normalized exciton density was fitted with Gaussians to extract the time-dependent mean-squared displacement (MSD) of the exciton density.

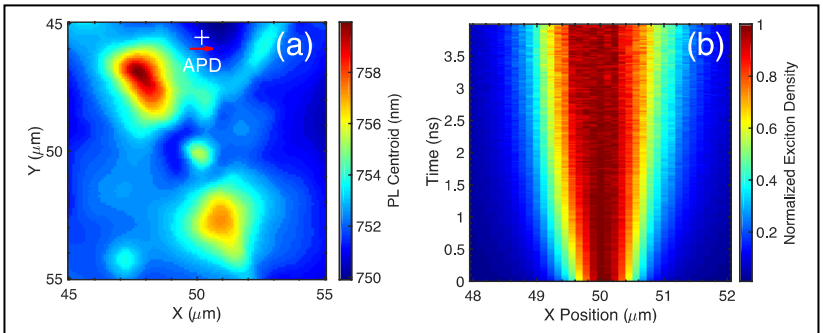

Figure 9: (a) Local PL centroid map showing the point of excitation on the WSe_2 monolayer indicated by the plus (+) sign. (b) Normalized exciton density as a function of position and time obtained with an avalanche photodiode detector (APD) and time-correlated single photon counting (TCSPC).

On the other hand, when the excitation was positioned at a strained point on the monolayer near the SiO_2 pillar, the exciton density's peak did not remain localized. Specifically, when the excitation was positioned just above the high tensile strain point on top of the pillar (Figure 10(a)) and the PL beam was monitored from top to bottom, the exciton density's peak shifted down and towards the high tensile strain point on the monolayer as shown in Figure 10(b). Similarly, when the excitation was placed just to the left of the high tensile strain point on top of the pillar and the PL beam was monitored from left to right, the exciton density's peak shifted to the right and towards the high tensile strain point as shown in Figure 10(c). A shift in the exciton density's peak position is expected to occur due to the strain gradient on the monolayer. Figure 10(d) shows the PL spectra measured at three positions along the *x*-axis near the SiO_2 pillar.

To explain our observations, we developed a model that encompasses the diffusion, drift, and relaxation of the exciton density of the WSe_2 monolayer based on Boltzmann's transport theory with the relaxation time approximation, and assuming a uniform exciton mobility[38–40]. The resulting differential equation describing the exciton dynamics is given by

$$\frac{\partial}{\partial t}n(x,t) = -\frac{n(x,t)}{\tau} + D(t)\left[\frac{\partial^2}{\partial x^2}n(x,t)\right] + \mu_\epsilon \frac{\partial}{\partial x}\left[n(x,t)\ \frac{\partial}{\partial x}\epsilon(x)\right] \qquad (2.1)$$

where the first, second, and third terms to the right-hand side of the equal sign respectively represent the relaxation of the exciton density denoted by $n(x,t)$ with relaxation time τ; the diffusion of the exciton density with time-varying diffusion coefficient $D(t)$; and the drift of the exciton density with strain mobility μ_ϵ due to the strain gradient $\partial\epsilon(x)/\partial x$. The strain mobility is simply defined as $\mu_\epsilon \equiv \left|\mu\left(\partial E_g/\partial\epsilon\right)\right| = |\mathrm{v}_d[\partial\epsilon(x)/\partial x]^{-1}|$, where μ is the traditional mobility, $\partial E_g/\partial\epsilon$ represents the sensitivity of the monolayer's direct bandgap to strain, and v_d denotes the density's drift velocity due to the applied strain gradient. Note that $\partial E_g/\partial\epsilon < 0$ since monolayer WSe_2's direct bandgap decreases with tensile strain[34]. The units of the strain mobility are length squared per unit time and percent strain, typically expressed in $cm^2s^{-1}\%^{-1}$. The traditional mobility is defined as $\mu \equiv \bar{t}/m^*$, where $\bar{t}$ is the mean free time of the excitons, and m^* is their effective mass[41].

In our case, the strain mobility is not uniform throughout the WSe_2 monolayer because the non-uniform strain field modifies the monolayer's band structure, affecting the excitons' effective mass[42] and their mean free time. We observed such non-uniformity after extracting the drift velocity from our measurements of the excitonic density as a function of position and time. We calculated the peak position's shift of the exciton density as a function of time, which essentially represents

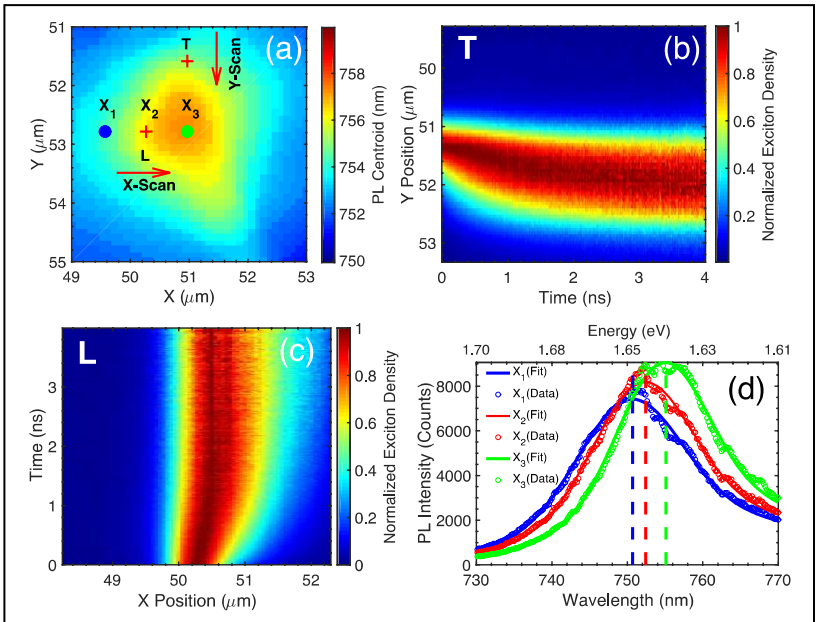

Figure 10: (a) PL centroid map of the WSe_2 monolayer zoomed in around the SiO_2 pillar and showing the excitation positions indicated by the plus (+) signs. (b) Normalized exciton density as a function of position and time when the excitation was placed above the pillar and the APD was scanned along the vertical direction from top to bottom and (c) along the horizontal direction from left to right. (d) PL spectra of the WSe_2 monolayer measured at the positions labeled by X_1 (blue), X_2 (red), and X_3 (green) in (a). The dashed vertical lines indicate the peak wavelengths of each PL spectrum. The tensile strain caused by the SiO_2 pillar is evidenced by the red-shifts, and the enhancement of the PL peak intensity as the strain increases. The PL spectra were fit with two Gaussians as WSe_2 typically shows exciton and trion resonances.

the drift velocity of the exciton density due to the applied strain gradient. The exciton density appears to reach drift velocities as large as 250 m/s and drift distances as large as 500 nm.

In summary, we showed that the motion of excitonic energy in monolayer WSe_2 can be controlled via strain gradients and we require about 0.2% strain to achieve the directed energy transport. The sensitivity of WSe_2's direct bandgap to strain enabled the creation of local excitonic potentials that resulted in the directional drift of exciton densities towards high-tensile strain points.

3 Exciton energy transport under dynamic strain:

Aspects of energy transport in organic semiconductors:

Organic semiconductors consist of carbon atoms that are covalently bonded by sp^2 hybridization that also form unhybridized out-of-plane P_z orbitals. Spatial overlap between these unhybridized P_z orbitals results in the molecular π- orbital system where the electrons remain delocalized. The π- molecular orbital can either form an extended electron cloud over the whole molecular backbone of the material or can be concentrated at one particular region in a conjugated molecule.

Excitons are electrically neutral bound electron-hole pairs that can have a net spin of zero (singlet excitons (S_1)) or one (triplet excitons (T_1)). In organic solids, excitons are strongly localized at the molecular sites due to weak interaction between adjacent molecules. The low dielectric constant of the molecular organic medium leads to reduced screening and high electrostatic attraction between the oppositely charged electron and hole and hence high binding energy of molecular excitons. The reported binding energy of excitons in molecular semiconductors ranges from 0.3 eV to 0.5 eV for singlet excitons [43, 44]. Triplet excitons have higher binding energy due to attractive exchange interaction between electron and hole of the same spin configuration[45].

Even though excitons in organic molecular systems are strongly localized, they can get relocated from one molecular (donor molecule in the excited state) site to another (acceptor molecule in the ground state) by radiative or non-radiative energy transfer schemes. The radiative energy transfer process depends strongly on the spectral overlap between the donor emission spectra and the acceptor absorption spectra. The efficiency of energy transfer also varies with the intermolecular distance between the donor and the acceptor molecules, d as d^{-6}. This energy transfer process is called Förster resonant energy transfer and dominates energy transfer between molecules separated less than 10 nm[46, 47]. Although mostly observed between singlet exciton species, Förster energy transfer can also take place from triplet excitons in phosphorescent donors [48–51].

On the contrary, the Dexter energy transfer process involves the physical transfer of an electron from a molecule in the excited state to another molecule in the ground state. This energy transfer process takes place in an extremely short-range (< 1 nm) and requires a strong overlap between donors and acceptor molecular orbitals. The efficiency of such an energy transfer process decreases exponentially with the intermolecular distance between donor and acceptor molecules [52].

The process of energy transfer in organic semiconducting medium takes place in the form of exciton diffusion. In particle physics diffusion refers to a process of the random walk where particles spread from a high concentration to a low concentration regime and is represented by the following equation:

$$\frac{dn}{dT} = D\nabla^2 n - \frac{n}{\tau} \quad (3.1)$$

Here, n is the particle density, τ is the particle lifetime, and D is the diffusivity. The diffusion length of the particle L_D can be written as:

$$L_D = \sqrt{ZD\tau} \quad (3.2)$$

Where Z takes the value of 1, 2, 3 depending on the dimensionality of the diffusion process i.e. diffusion in one dimension, two dimensions, or three dimensions, respectively.

In an organic semiconductor, the process of exciton diffusion is strongly affected by an energetic disorder that results from molecular aggregation, inhomogeneity that results from molecular reorientation in the solid thin film during the growth phase, molecular conjugation and other physical processes. This energetic disorder results in a two-step diffusion process in amorphous organic medium- downhill energy relaxation or thermalization and thermally activated hopping[53, 54]. The downhill energy migration process dominates at low temperatures (<150 K) and leads to a nearly temperature-independent diffusion length and diffusivity. Here the excitons reach the low energy tail of the Gaussian density of states and recombine, leading to redshift in the emission spectrum at low temperatures. Strongly suppressed exciton-phonon coupling at lower temperatures results in a nearly temperature-independent diffusive transport regime. On the contrary, at higher temperatures (> 150K), the exciton diffusion is dominated by thermally assisted hopping between the molecular sites with similar energy, and an increase in diffusivity and diffusion length is observed. Similar regimes of energy transfer in amorphous disordered medium have also been observed and reported in the literature[55–60].

Energetic disorder in solid films also affects the energy transfer process by modulation of intermolecular separation as[61]:

$$d_{eq} = [n_{eq}]^{1/3} = [N_0\, exp(-\frac{\sigma^2}{2(KT)^2})]^{1/3} \quad (3.3)$$

Therefore, a molecular system with high energetic disorder (σ) at a particular temperature would have large effective intermolecular separation and so, less efficient energy transfer process [62]. At the same time, at low temperatures, the intermolecular separation may reach the same order as the Förster radius of the molecule in a homogeneous medium and so, the energy transfer process becomes less efficient.

As the intermolecular energy transfer process in organic semiconductors is mostly Förster transfer assisted, we primarily focus on the discussion of the aspects of this radiative energy transfer process. The rate of Förster resonant energy transfer, k_{FRET} is represented by the following equation[63–65]:

$$k_{FRET} = \frac{1}{\tau_{hop}} = \frac{1}{\tau_0}(\frac{R_0}{d})^6 \quad (3.4)$$

Here, τ_{hop} is the hopping time between the donor and acceptor molecular sites, d is the intermolecular separation, τ_0 is the exciton lifetime.

The Förster radius of the molecule, R_0 can be written as:

$$R_0^6 = \frac{9\phi_{PL}\kappa^2 J}{128\pi^5 n^4} \quad (3.5)$$

$$J = \int \lambda^4 F_D(\lambda)\sigma_A(\lambda)d\lambda \quad (3.6)$$

Here, J refers to the overlap integral between the donor emission spectrum and the acceptor absorption spectrum. The generalized diffusivity, D can be defined as[66]:

$$D = \frac{A}{\tau_0}\sum_N d^2 k_{ET} \quad (3.7)$$

Here, A is a term that represents the disorder in the solid-state thin film, d refers to the distance for a single hop, k_{ET} is the energy transfer rate from one site to surrounding N sites on the lattice. If one considers hopping between only the nearest neighbors, the generalized diffusivity reduces to:

$$D = \frac{Ad^2}{6\tau_{hop}} = \frac{A}{\tau_0}\frac{R_0^6}{6d^4} \quad (3.8)$$

Therefore, from eq. 3.5 and 3.6, the diffusivity in an amorphous semiconducting medium is affected by the spectral overlap factor J, the dipole-dipole orientation factor κ^2, the photoluminescence quantum yield Φ_{PL}, refractive index of the medium n and intermolecular separation d. Among the discussed parameters, the spectral overlap factor J and optimization of fluorescence quantum yield Φ_{PL} may have a greater impact on the energy transfer process. In an amorphous film with completely randomized dipole orientation, κ^2 is approximated by a value of 0.476[65, 67] and the most effective orientation of the dipoles in the medium would yield an increase in diffusivity of about 1.7 times (and consequent increase in diffusion length by 2.9 times)[68, 69]. Therefore, to achieve highly diffusive excitonic species, donor-acceptor molecular combinations with strong fluorescence yield and larger spectral overlap factor J are required.

Strain assisted energy transfer process in organic system:

As the energy transfer process in an organic semiconductor is strongly affected by intermolecular separation, such a process is expected to be strongly modulated by mechanical excitation i.e. application of external mechanical strain. Under hydrostatic pressure, the charge transport properties of crystalline organic materials show dramatic change and near band-like transport characteristics[70–73]. Externally applied

pressure has been utilized to trigger enhanced spectral diffusion in lightly doped Alq_3: DCM2 guest: host system. The authors report a strong spectral modulation under the application of external compression and spectral tuning of 20 nm has been reported[24]. Our more recent work report modulation of the emission spectrum of a similar guest: host system under tensile strain[74]. This spectral response can be explained by the widely reported and studied solid-state solvation effect triggered by a change in the local dielectric environment under applied strain[75, 76].

We first explore the exciton transport dynamics in organic semiconductors under static strain. Therefore we numerically solve a modified form of eq. (2.1) incorporating the effect of solid-state solvation in amorphous organic medium and change in Forster energy transfer rate under applied external mechanical stimuli[24]. According to Chang et al. [24], under externally applied pressure and assuming single dipole-dipole interaction, the Forster energy transfer rate shows a monotonic increase with pressure i.e. compressive strain:

$$k_{F,\varepsilon} = k_F * (\frac{1}{1-\alpha Y \varepsilon})^2 \tag{3.9}$$

Here, $k_{F,e}$ and k_F refer to the Förster rate of a thin film under applied external compressive strain and no strain respectively, α refers to a fitting parameter that relates the change in the local dielectric constant of the organic thin-film per unit of external pressure, Y is Young's modulus of the thin film, and ε is the applied external strain. From the relationship between the diffusivity and Forster rate we can write the diffusivity of the organic thin-film under external pressure, D_ε by the following equation:

$$D_\varepsilon = D(\frac{1}{1-\alpha Y \varepsilon})^{\frac{4}{3}} \tag{3.10}$$

Therefore, taking into account the effect of external mechanical stimuli, we can write:

$$\frac{dn(x,t)}{dt} = \frac{d^2(D_\varepsilon(x)n(x,t))}{dx^2} - \frac{n(x,t)}{\tau} - \frac{d}{dx}(n(x)v(x))$$

$$\Rightarrow \frac{dn(x,t)}{dt} = \frac{d^2(D_\varepsilon(x)n(x,t))}{dx^2} - \frac{n(x,t)}{\tau} - \frac{d}{dx}(n(x)\mu_e \frac{dU(x)}{dx})$$

$$\frac{dn(x,t)}{dt} = \frac{d^2(D_\varepsilon(x)n(x,t))}{dx^2} - \frac{n(x,t)}{\tau} - \frac{d}{dx}(\mu_e n(x) \frac{dU(x)}{d\varepsilon(x)} \frac{d\varepsilon(x)}{dx}) \tag{3.11}$$

where,

$$Gaussian\ energy\ gap\ profile: U(x) = U_0\ exp(-\frac{(x-b)^2}{2\sigma^2})$$

$$Gaussian\ strain\ profile: \varepsilon(x) = \varepsilon_0\ exp(-\frac{(x-b)^2}{2\sigma^2})$$

Here we model the transport dynamics by a Gaussian external strain profile. For the simplest of approximation, we assume that the energy gap will be modulated by a similar gaussian profile according to Chang et al. [24]. Therefore, according to eq. (3.11) under static strain, the spatial diffusivity can be modeled by a gaussian profile.

As an archetype system, we model the exciton dynamics in lightly doped Alq_3: DCM guest: host system. We first extract the change in diffusivity and energy gap modulation under externally applied strain according to eq. (3.11). The results are shown in Figure 11. As seen from Figure 11(a), the diffusivity shows an increase under externally applied pressure. As the organic thin film is compressed, the inter-molecular distance decreases, which lead to an increase in the hopping rate between two neighboring sites and so an increase in diffusivity is observed. Figure 11(b) shows the variation in the energy gap under external mechanical stimuli. According to the solid-state solvation effect, compressive (tensile) stress leads to an increase (decrease) in the local dielectric constant, and therefore, the solvation energy of the excited molecules increases (decreases), triggering a redshift (blueshift) in the emission spectrum and so an increase (decrease) in the energy gap profile is observed. From our extracted diffusivity and energy gap modulation under static strain, we assume a static strain amplitude of 5 % that corresponds to about 100 meV redshift in the emission profile of the organic fluorophore and a corresponding 1.3 times increase in the diffusivity of the molecules in the thin film (please refer to Figure 11).

We numerically solve eq. (3.11) to study the exciton dynamics under static strain in a lightly doped Alq_3: DCM thin film under static strain where the gaussian strain profile is assumed to be centered at 10 nm (From the calculated exciton diffusivity under compression we calculate exciton diffusion length $L_D = (D\tau)^{1/2} \approx$ 16 nm). From our simulation results shown in Figure 12, we observe no drift like feature in the exciton dynamics under static strain as experimentally observed for strained WSe_2 monolayer in Figure 10.

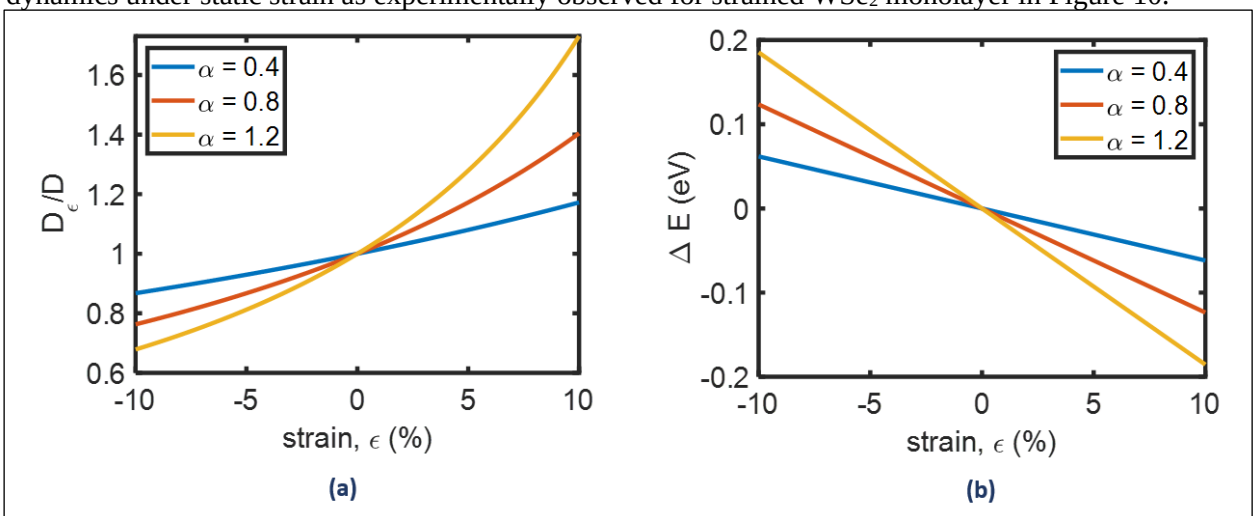

*Figure 11:*Variation in diffusivity and energy gap under externally applied strain for 1% doped Alq3: DCM thin film. (a) Variation in energy gap. (b) Variation in the energy gap. Here compressive strain has been assumed to be positive.

We attribute the absence of drift in the exciton dynamics in the strained organic thin film to the nature of the chemical bond in the material[77]. In crystalline inorganic semiconductors, the atoms are bound together by strong ionic bond, covalent bond, or a mix between the two. Such materials are characterized by a strong well-defined band structure and a bandgap that separates the valance band and the conduction band of the semiconductor. In the bulk form, these materials also show a continuum of energy states from the valance band maxima to lower energies and conduction band minima to higher energies. Therefore, the carrier transport properties of these materials show band-like transport properties and carriers can reach mobilities up to a few thousand $cm^2/V/s$. On the contrary, in the organic semiconductor molecules, the atoms share covalent bonds among themselves and the intermolecular forces are electrostatic in nature i.e. the intermolecular forces in these materials consist of dipole-dipole, dipole-induced dipole, induced dipole - induced dipole interaction forces. The molecules are randomly oriented and show very weak interaction among themselves. As a result, such materials do not form a well-defined band structure and instead of having a bandgap, organic semiconductors are characterized by an energy gap between the frontier orbitals known as the highest occupied molecular orbital (HOMO) and lowest unoccupied molecular orbital

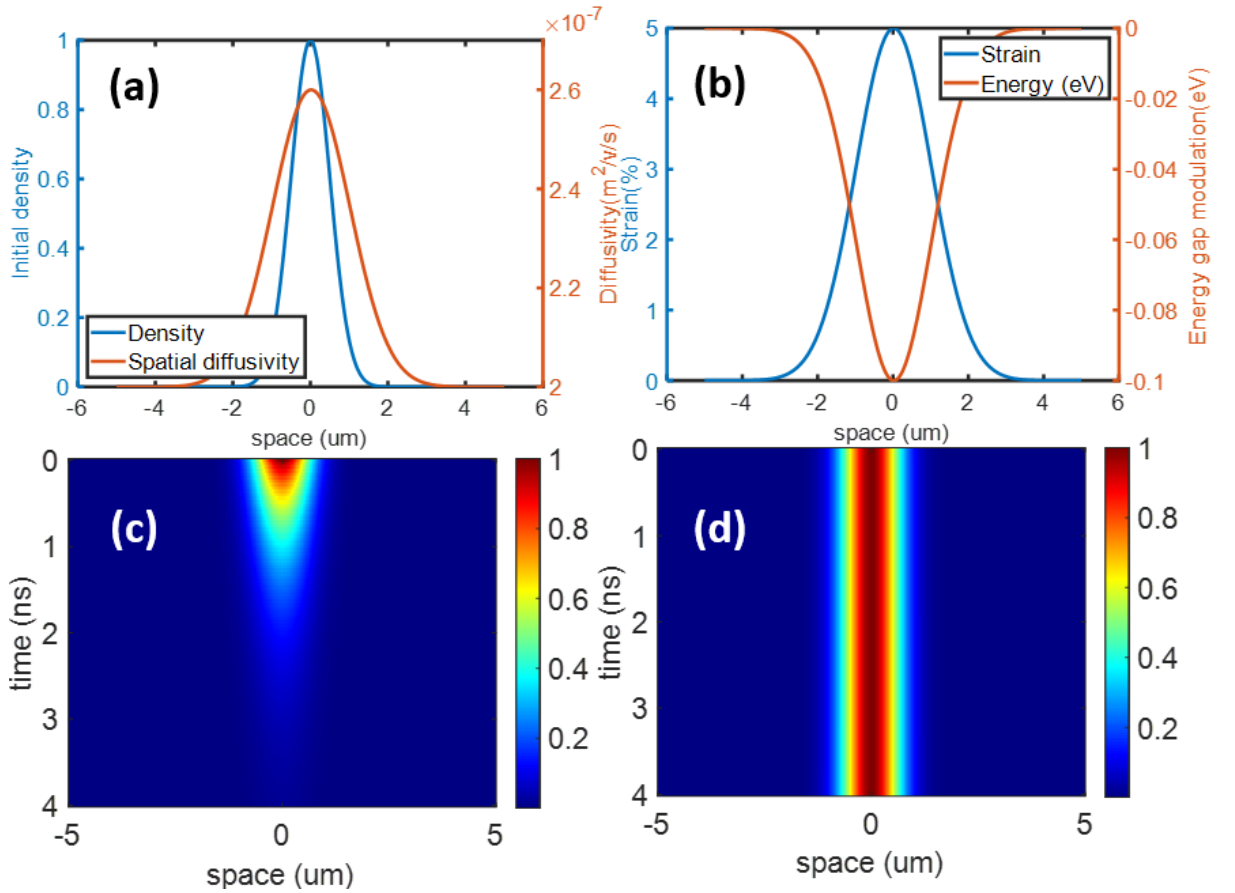

Figure 12: Simulated exciton dynamics in compressed lightly doped Alq3: DCM thin film under pulsed excitation. (a) Initial exciton density and spatial diffusivity profile. (b) Gaussian compressive strain profile and the corresponding modulation in energy gap under strain. (c) Exciton dynamics under pulsed excitation. (d) Normalized exciton density at each time slice. The gaussian static strain is centered at 10 nm (within the exciton diffusion length, $L_D = (D\tau)^{1/2} \approx 16$ nm).

(LUMO). Upon absorption of a photon, the molecules reach a higher energy excited state which is strongly localized at molecular sites due to weak dielectric. These excited states are called excitons and show binding energies in the region of 0.5 – 1.0 eV. Energy transfer in organic semiconductors is dominated by hopping like transport of these excited states between neighboring molecular sites which depends on intermolecular forces, molecular orientation in the thin film, molecular packing density, local dielectric properties of the organic semiconductor thin film, the spectral overlap between the molecular sites. Therefore, extrinsic diffusivity in these semiconductors is very low (~ 10^{-3} cm^2/s). Unlike organic semiconductors, strong band-like transport in inorganic semiconductors means that mobile carriers can reach very high mobilities. Therefore, exciton diffusivity in these materials is in the range of a few cm^2/s. High exciton diffusivity in these materials also leads to high exciton mobility and the excitons interact strongly with energy gap modulation under strain. Therefore, the exciton transport show drift like feature under external strain. Due to poor diffusivity and correspondingly weak exciton mobility, drift like features are not present in organic semiconductor exciton transport dynamics.

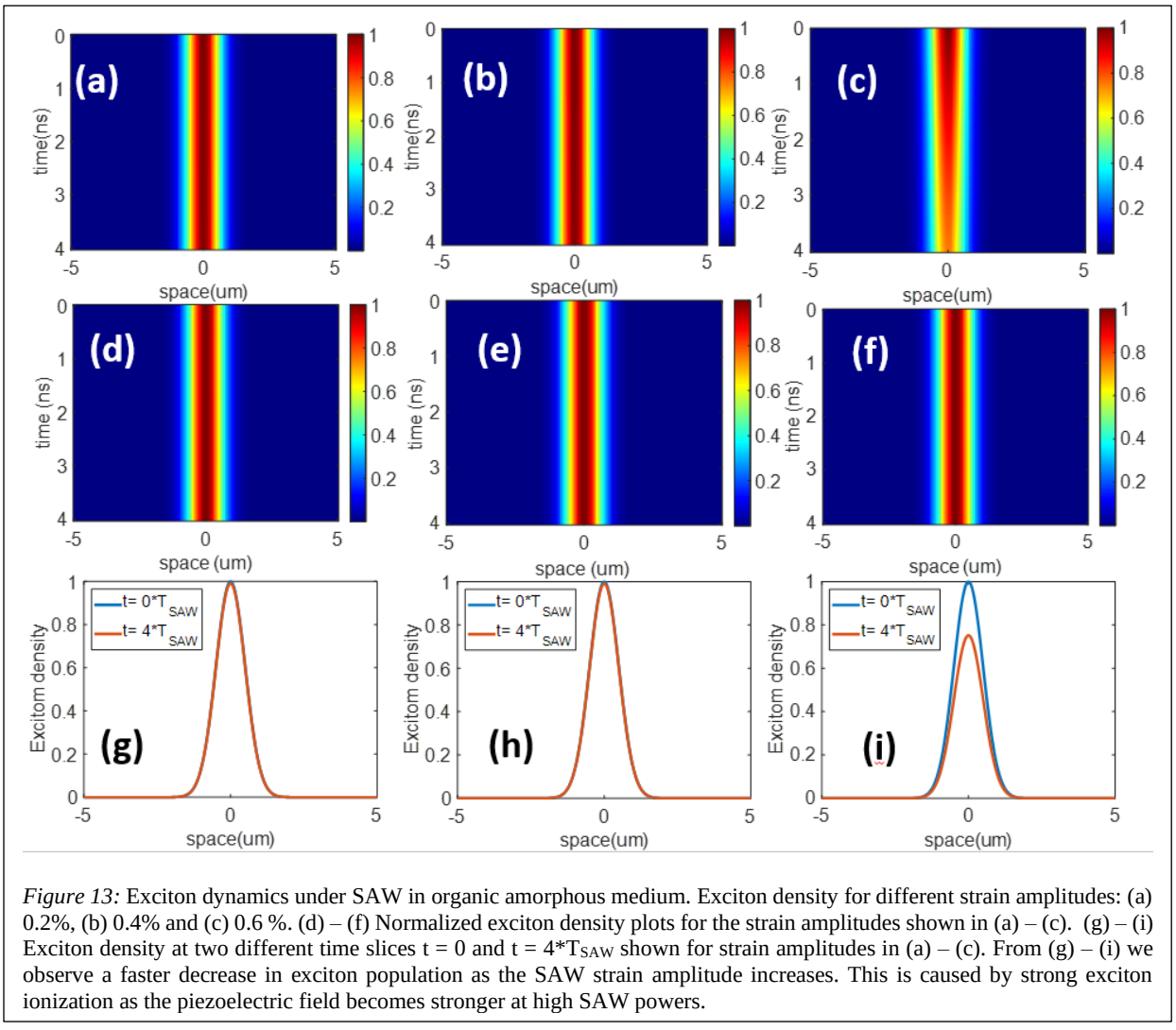

Figure 13: Exciton dynamics under SAW in organic amorphous medium. Exciton density for different strain amplitudes: (a) 0.2%, (b) 0.4% and (c) 0.6 %. (d) – (f) Normalized exciton density plots for the strain amplitudes shown in (a) – (c). (g) – (i) Exciton density at two different time slices t = 0 and t = 4*T_{SAW} shown for strain amplitudes in (a) – (c). From (g) – (i) we observe a faster decrease in exciton population as the SAW strain amplitude increases. This is caused by strong exciton ionization as the piezoelectric field becomes stronger at high SAW powers.

Exciton coupling to mechanical wave in organic medium:

We also simulated exciton dynamics in an amorphous organic medium under the influence of surface acoustic waves. Due to low diffusivity of the amorphous medium, like static strain, the dynamic strain wave does not interact with the exciton population and we do not see oscillation like features in the exciton dynamics. However, due to SAW piezoelectric field, we observe exciton dissociation as the SAW piezoelectric field becomes stronger. To study exciton dynamics under the influence of SAW we assume exciton lifetime, $\tau \approx 500$ ns, which is typical in thermally activated delayed fluorescence (TADF) based organic semiconducting systems[78, 79].

The simulation results under pulsed excitation conditions are shown in Figure 13. We show simulation results for three different SAW strain amplitudes: 0.2%, 0.4% and 0.6%. i.e. input SAW power Figure 13(a) – (c) shows the exciton density under different SAW strain amplitudes followed by normalized exciton density under the same SAW powers in Figure 13(d) – (f). Form Figure 13(a) – (c) we see a gradual increase in exciton dissociation as SAW input power is increased. At higher input power the piezoelectric field becomes stronger and so, an increase in exciton dissociation is observed. The increased dissociation with SAW power is more obvious in Figure 13(g) – (i) where exciton density at three different time slices t =0 and t = 4*T_{SAW} are shown. Exciton dissociation occurs at a much faster rate at SAW input power is increased i.e. SAW strain amplitude is increased.

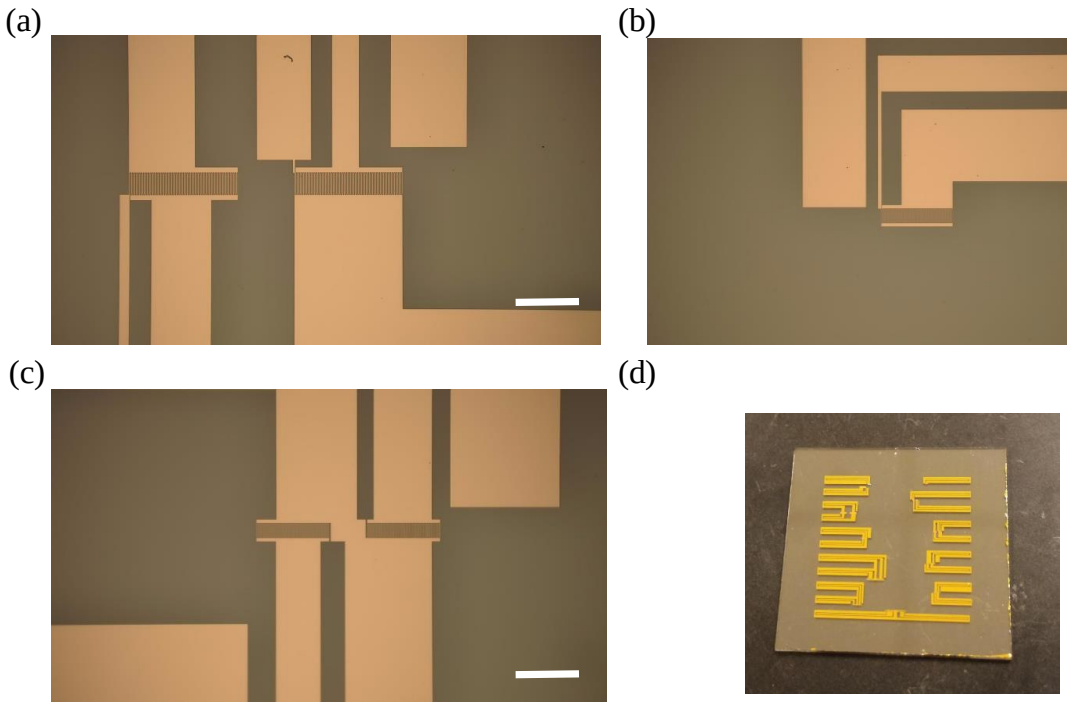

Figure 14: (a) SAW device with simple delay line; (b) SAW device with only input IDTs; (c) SAW device with a grounded metal thin film on top of the delay line; (d) Bird's eye view of the fabricated $LiNbO_3$ device chip. Scale bar is 175 μm.

In order to study the coupling of exciton to dynamically moving strain field, we designed and fabricated various surface acoustic wave (SAW) devices on piezoelectric 64° Y-cut $LiNbO_3$ Lithium Niobate ($LiNbO_3$) substrate for generating surface acoustic waves as shown in Figure 14. We performed photoluminescence intensity measurements on two different exciplex systems under CW excitation – m-MTDATA: TPBi and m-MTDATA: BPhen. We fabricated IDTs on 128° $LiNbO_3$ substrates and evaporated organic materials on top of the substrates using thermal evaporation. We applied rf – signal to the IDTs using a network analyzer to resonantly excite the devices and generate surface acoustic waves.

We first measure the photoluminescence signal from thin films of m-MTDATA: TPBi, m-MTDATA: BPhen blend as well as m-MTDATA/ TPBi, m-MTDATA/ BPhen bilayer samples. We perform photoluminescence measurements under 405 nm pulsed excitation. The results of PL measurement are shown in Figure 15. We observe emission from the long-lived exciplex state from neat thin films of m-MTDATA: TPBi (1:1) and m-MTDATA: BPhen (1:1) blend as shown in Figure 15(a). The exciplex

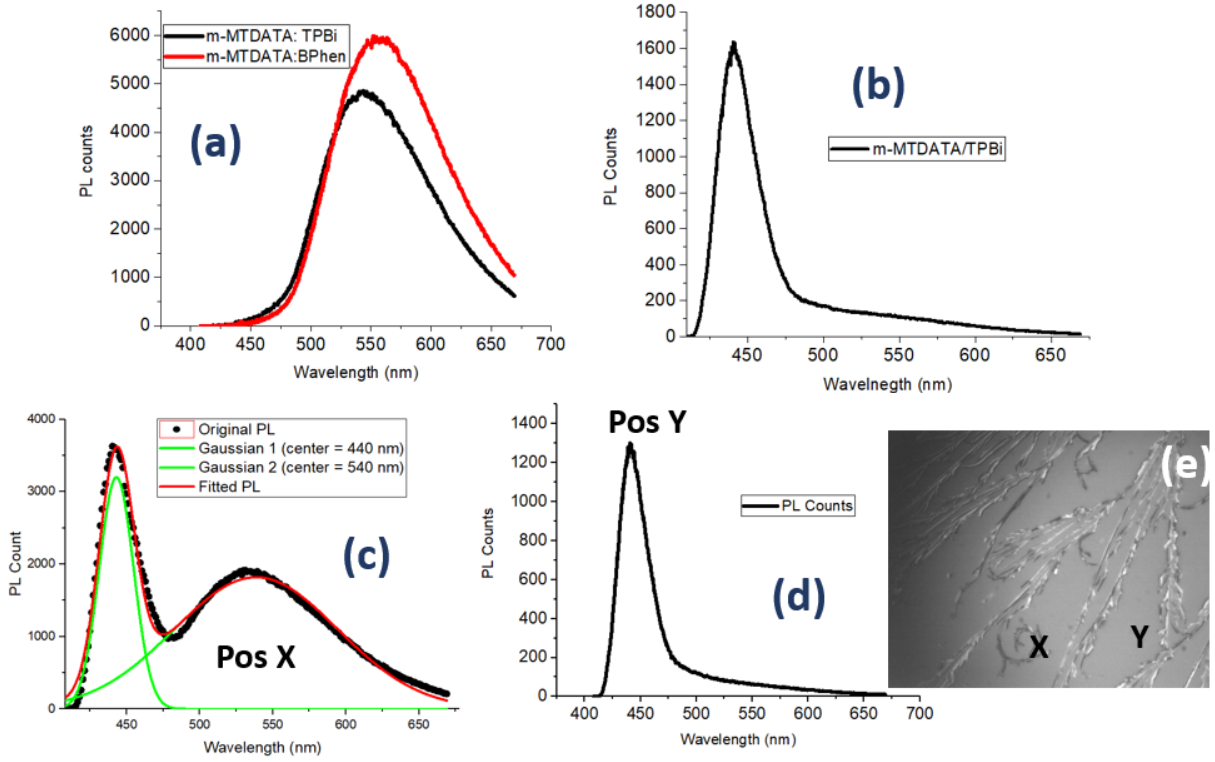

Figure 15: Photoluminescence(PL) measurement on neat exciplex samples on SiO_2 substrates. The excitation wavelength is 405 nm. (a) 25 nm m-MTADAT:TPBi (1:1) blend and m-MTADAT:BPhen (1:1) blend. For same excitation power and collection conditions, we see a stronger PL response from m-MTADAT:BPhen belnd due to lower singlet-triplet energy separation ($\Delta E_{ST} \approx 0$). The emission is centered at around 550 nm which corresponds to emission from long lived exciplex state;(b) m-MTDATA/TPBi (15 nm/15 nm) bilayer; The PL response is dominated by emission from m-MTDATA neat film. Strong exciplex signal is not present due to inefficient electron transfer from m-MTDATA to TPBi after excitation. (c) – (d) PL measurements at two different positions of m-MTDATA/BPhen (15 nm/15 nm) bilayer sample at two positions. The positions are marked in optical image of the same bilayer thin film shown in (e). Due to self-assembled aggregate formation of BPhen after evaporation, concentrated spiral shape regions are observed on the thin film that shows strong and efficient exciplex formation.

emission from m-MTDATA: BPhen (1:1) blend is much stronger due to the lower energy separation between singlet and triplet states *($\Delta E_{ST} \approx 0$)* that increases the rate of reverse intersystem crossing and increases fluorescence yield[79]. We also observe and study the PL signal from bilayer thin films of m-MTDATA/ TPBi and m-MTDATA/ BPhen. Due to inefficient charge transfer at m-MTDATA/ TPBi interface upon the excitation of only m-MTDATA, the m-MTDATA/ TPBi bilayer emission is dominated by emission from m-MTDATA(Figure 15 (b)). However, in the case of m-MTDATA/ BPhen thin film we see strong emission from the long-lived exciplex state at positions(Pos X in Figure 15(e)) where BPhen molecules form aggregate like states[80–82]. These aggregate regions are formed as a result of self- assembled crystallization of BPhen when m-MTDATA is used as an underlayer and help efficient charge transfer from m-MTDATA to BPhen after excitation and therefore strong emission from the exciplex states. Such strong exciplex emission is not observed from positions (position Y in Figure 15(e)) where BPhen aggregates are not formed.

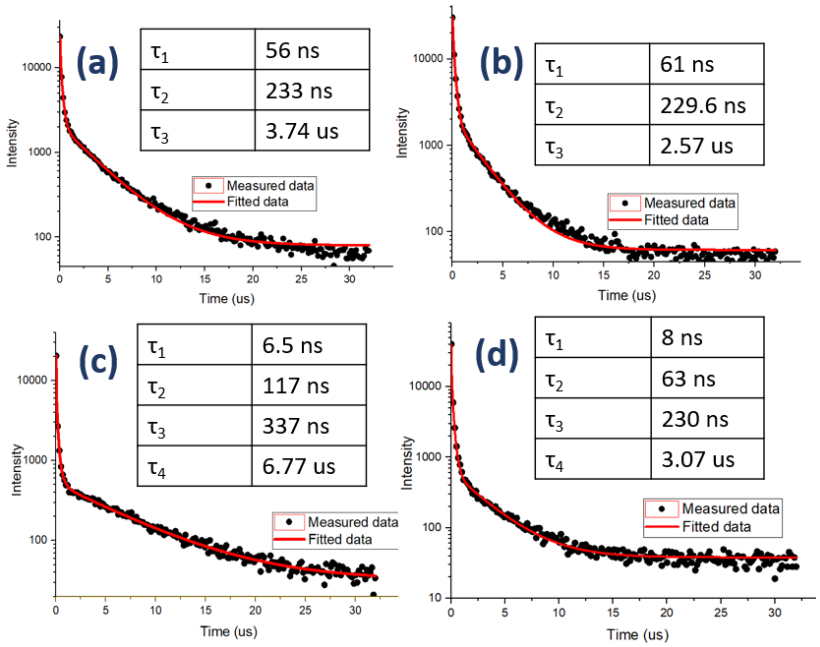

Figure 16: Measured and fitted transient photoluminescence data from thermally evaporated thin-films of (a) m-MTDATA: TPBi (1:1) blend; (b) m-MTDATA: BPhen (1:1) blend; (c) m-MTDATA/ TPBi bilayer; (d) m-MTDATA/ BPhen bilayer. The samples were excited with a 405 nm pulsed laser with 31.25 kHz repetition rate. The measured data were fitted with a multi-exponential function shown in eq. (3.12) in the main text.

To understand the exciton formation dynamics in the blend and bilayer exciplex material system, we perform transient fluorescence measurement under pulsed excitation on thermally evaporated blend and bilayer thin-films. We use the excitation wavelength of 405 with a 31.25 kHz repetition rate that excites m-MTDATA only. The measured transient fluorescence intensity plots are fitted with a multi-exponential function to understand the dynamics of different excitonic species:

$$I(t) = I_0 + \sum_i A_i exp(-\frac{t_i}{\tau_i}) \qquad (3.12)$$

The results of transient photoluminescence measurement are shown in Figure 16. The lifetime components measured from our fit is also shown in the figure. We can fit the transient fluorescence data measured form

the 1:1 m-MTDATA: TPBi and m-MTDATA: BPhen blend samples using a three component exponential function as shown in eq. (3.12). From our fitting, the first component ~60 ns correspond to prompt fluorescence from the donor-acceptor blend. The second and third components (~ 230 ns and > 2μs) correspond to delayed fluorescence from the thin film due to triplet - singlet transition following reverse intersystem crossing. On the contrary, for the bilayer thin- films, to get a better fit of the measured data we have to use four-component exponential functions. We also observe a stark difference in our fit of transient fluorescence data for m-MTDATA/ TPBi and m-MTDATA/BPhen bilayer thin films of the same thickness and measured under the same experimental conditions. For the m-MTDATA/ TPBi bilayer, the fastest component of about 6.5 ns corresponds to pure m-MTDATA emission. The second component in the region of 117 ns corresponds to prompt fluorescence from the exciplex state formed at the bilayer interface. However, compared to the prompt fluorescence component measured for blend thin films (~ 60 ns) the higher prompt fluorescence lifetime in bilayer samples indicates inefficient electron transfer from m-MTDATA to TPBi and therefore, exciplex formation. This observation is also consistent with higher lifetime components of the delayed fluorescence process (~330 ns and > 6 μs). On the contrary, when we fit the m-MTDATA/ BPhen bilayer data, the fast lifetime component was found to be ~ 11 ns. Since we see strong emission from m-MTDATA in the m-MTDATA/ BPhen bilayer thin-film we attribute this component to emission from m-MTDATA. However, this fast component was found to be higher than the fast component found from m-MTDATA/ TPBi bilayer. This can be explained by the efficient charge transfer mechanism at the m-MTDATA/ BPhen interface as BPhen aggregates are formed due to the self-crystallization of BPhen following thermal evaporation. The charge transfer process competes with the fluorescence exciton recombination process in neat m-MTDATA and decreases the fluorescence yield from m-MTDATA emission. The BPhen aggregates formed at the m-MTDATA/ BPhen interface greatly improves the charge transfer from m-MTDATA to BPhen molecule and assist in the formation of exciplex species. The efficient formation of exciplex species is also verified from the remaining lifetime components extracted from the fitted data. The lifetime components for prompt and delayed fluorescence processes from

Table 1: Lifetime components extracted from multi-exponential function shown in eq. (3.15) of the transient photoluminescence data measured from thin-films of 1:1 blend and bilayer samples.

Material system	Component 1	Component 2	Component 3	Component 4
m-MTDATA: TPBi blend	56 ns	233 ns	3.74 us	
m-MTDATA: BPhen blend	61 ns	229.6 ns	2.57 us	
m-MTDATA/ TPBi bilayer	6.5 ns	117 ns	337 ns	6.77 us
m-MTDATA/ BPhen bilayer	8 ns	63 ns	230 ns	3.07 us

m-MTDATA/ BPhen thin film were found to be similar to those from m-MTDATA: BPhen (1:1) blend samples. The lifetime components extracted from our fit are shown in Table 1.

We have performed fluorescence imaging measurements under SAW excitation for both blend and bilayer exciplex samples. Figure 17 shows measurement results from m-MTDATA: TPBi (1:1) blend sample under SAW excitation. Figure 17(a) shows the S11 measurement from one of the representative devices. The measurement shows a resonance at around 890 MHz. Figure 17(b) shows Fluorescence imaging measured on one of the off-axis locations. The off-axis and on-axis locations on the device are shown in Figure 17(c). Since off-axis locations are outside the lateral width of the SAW device IDTs, the exciton density generated at these locations by optical excitation should not show any modulation under SAW excitation. From Figure 17(b), we observe no modulation of the fluorescence intensity at different SAW power. Figure 17(d) shows intensity measurement on an on-axis location under different SAW power. From this figure, we see modulation in the excitation density as SAW power is varied. As we increase the input RF power we see a gradual quenching in the fluorescence intensity. We attribute this modulation to exciton dissociation by the

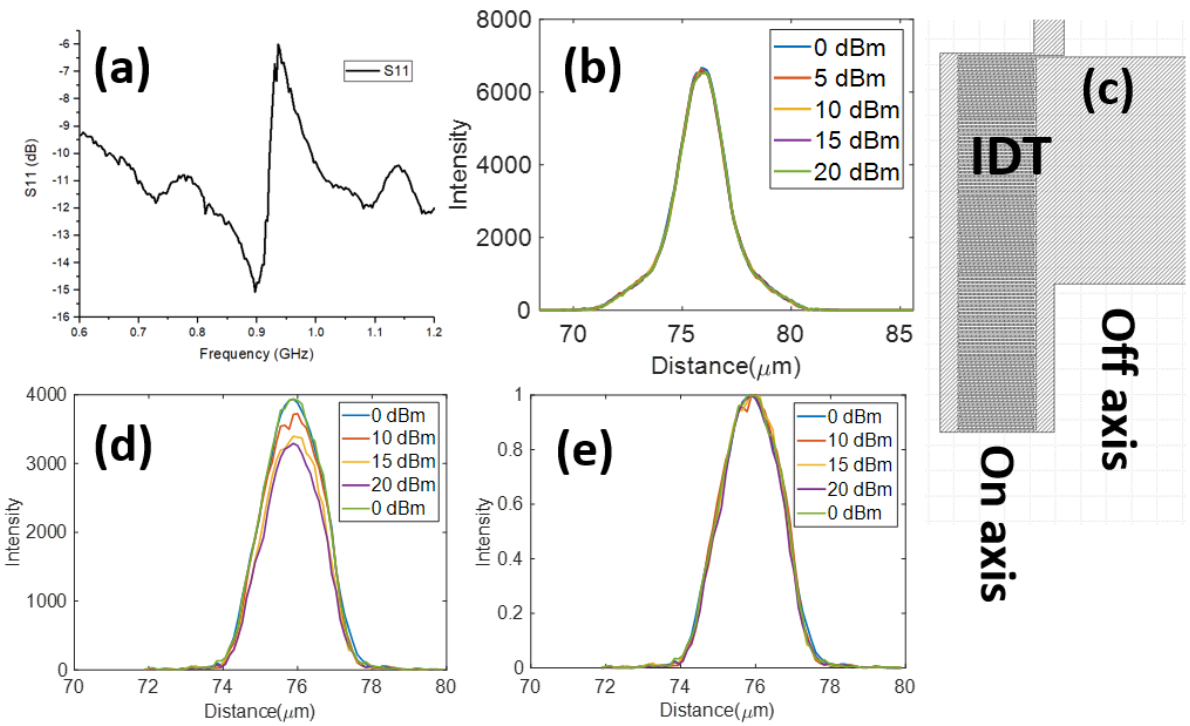

Figure 17: Experimental observation of exciton dynamics in amorphous organic medium under SAW. (a) Measured reflection co-efficient that shows a resonance at about 900 MHz. (b) Fluorescence intensity at off-axis position under different SAW powers. As we can see, at off- axis position, no modulation in the fluorescence emission is observed with SAW power. (c) A schematic image of the SAW IDTs showing the off-axis and on-axis measurement positions. (d) Fluorescence intensity measurements at an on-axis position at different SAW powers. A clear modulation of SAW intensity is observed with SAW power. As SAW power is increased from 0 dBm, the fluorescence intensity decreases gradually. The intensity recovers as the SAW power is tuned back to 0 dBm. (e) Normalized intensity plot at the same measurement position of and at the same power levels mentioned in (d). As no distortion is observed in the normalized intensity plot, its obvious that the exciton population show no displacement i.e. spatial modulation with increased SAW power. Here, we show results for m-MTDATA: TPBi (1:1) blend. Similar results are observed for m-MTDATA: BPhen(1:1) blend.

electric field of the traveling surface acoustics wave which has been reported in other excitonic media[83–85]. Figure 17(e) shows normalized intensity plots at different SAW powers. From the normalized intensity plot, we observe no spatial distortion in the intensity profile under SAW power. This is also consistent with the earlier simulation results that shows no modulation of exciton density under increased amplitude of the SAW strain wave i.e. increased SAW power. We also observed similar results from our measurements on m-MTDATA: BPhen (1:1) blend samples and bilayer m-MTDATA/ TPBi and m-MTDATA/ BPhen samples.

From our study on exciton dynamics control by mechanics, we have been able to trigger solid-state solvation effect in lightly doped Alq_3: DCM solid-state thin film. We have been able to relate the optical response of strained solid-state amorphous thin film to its mechanical properties and extract Young's modulus of the thin film. However, we could not achieve active control of excitation dynamics under mechanical excitation. We attribute the lack of control over spatial exciton dynamics under external strain to the amorphous nature of the organic semiconductor. As mentioned in the main text, in the amorphous medium the molecular excitons are strongly bound to molecular sites and exciton diffusion takes place by hopping mechanism from one molecular site to another. Control of intermolecular distance would, therefore, change the hopping rate and trigger a change in the exciton diffusion. However, to obtain a directional feature in the spatial exciton dynamics, the generated exciton density needs to couple to the energy landscape of the solid-state medium. This coupling is defined by the strain mobility which is derived from the intrinsic mobility of the medium. Due to the amorphous nature of the medium, when compared to crystalline inorganic semiconductors, the intrinsic mobility in organic semiconductors are a few orders of magnitude smaller and therefore, to obtain directional control over exciton dynamics organic semiconductors with large exciton diffusivity are required.

However, as seen from the results in TMDs, the exciton dynamics can be controlled by applying static and dynamic mechanical stimuli, and materials that sustain exciton at room temperature can be exploited in this regard. Since dynamic exciton modulation strongly depends on exciton mobility, TMDs and their heterostructures with organics can be used as promising candidates for dynamic exciton modulation under SAW. As described in the next section, the hybrid excitons formed at the TMD/organic interface has higher diffusivity than excitons in individual systems and could be an ideal platform for future work.

4 Organic – TMD hybrid platform for enhanced transport:

While we have looked into organic guest host systems as well as TMD's, we explored the feasibility of hybrid heterointerfaces formed between organic and TMD monolayers. The hybrid heterojunction formed by combining inorganic and organic semiconductors offers a unique platform that can reap the benefits of both the material systems. For instance, organics are well known for the strong absorption but have poor charge mobility, whereas inorganics have comparably low absorption but excellent charge transport properties. Pairing these disparate systems can not only lead to a new material system that is highly absorptive with exception mobility but also enable control over band-like transport in inorganics to charge hopping transport in organics.[86, 87] However, before using the hybrid material system for studying exciton mechanics interactions, we need to understand the energy dynamics associated with the Frenkel excitons in organics and Wannier-Mott exciton in inorganics at the hybrid heterojunctions.

To begin, we fabricated a hybrid photodetector based on an organic-inorganic heterojunction and use it as a platform to study the energy transfer (ET) process across the interface. The photodetector features a heterojunction made of highly absorbing j-aggregate thin film of organic dye TDBC (5,6-dichloro-2[3-[5,6-dichloro-1-ethyl-3-(3-sulfopropyl)-2(3H)-benzimidazolidene]-1-propenyl]-1-ethyl-3-(3-sulfopropyl) benzimidazolium hydroxide) and a monolayer Molybdenum disulphide (MoS_2). J-aggregates of organic dyes are formed due to dipole alignment of fluorescent molecules as shown in Figure 18(a). The absorption spectrum of TDBC shifts from a broad monomer band centered around 515 nm to a strong and narrow j-band peaked at 590 nm, while the photoluminescence (PL) peak is red shifted by just 4 nm as shown in Figure 18(b).[88] We use monolayers of MoS_2, as the inorganic material due to its atomic scale two-dimensionality, which is the physical limit that cannot be achieved using other engineered structures and excellent spectral overlap with TDBC j-aggregate. As shown in Figure 18(b), the *B*-excitonic[89] absorption peak of MoS_2 has high spectral overlap with the j-aggregate PL emission. The inset in Figure 18(b)

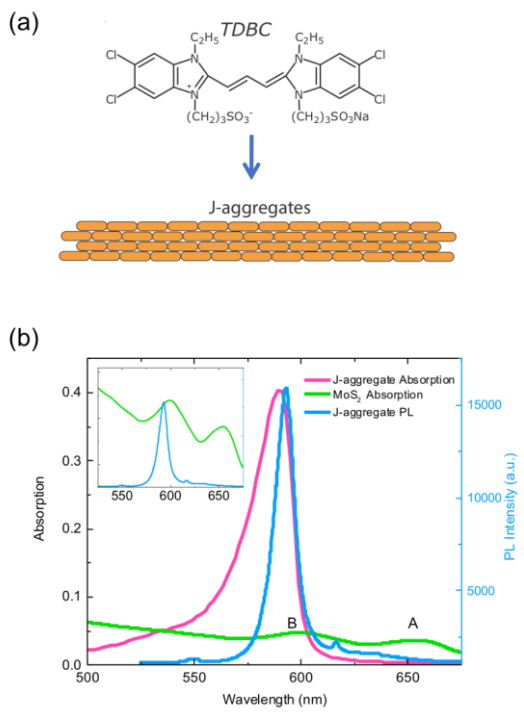

Figure 18: (a) Chemical structure of organic dye TDBC and the head-to-tail molecule orientation in its j-aggregate form. (b) Spectra showing j-aggregate absorption, PL emission, and MoS_2 absorption. A and B excitonic resonances of MoS_2 at 655 and 599 nm were denoted on the figure, respectively. The inset figure shows the normalized spectra, highlighting the spectral overlap between j-aggregate emission and MoS_2 B-exciton absorption.

shows the normalized MoS_2 absorption and j-aggregate PL spectra for easier visualization of the overlap. The MoS_2 resonances are very sensitive to the local dielectric environment (substrate).[90, 91] We found that the *B-excitonic* resonance were typically located at 595 nm for the photodetector samples further improving the overlap. The peak shown in Figure 18(b) is slightly red shifted, due to a different substrate (transparent) used for collecting the absorption data.

While energy transport between donor-acceptor pairs is traditionally studied by measuring photoluminescence (PL) quenching and exciton lifetime,[92–95] we demonstrate a new approach that can be used for studying material systems with short exciton lifetimes that fall beyond the measurement capabilities of the commonly used time correlated single photon counting (tcspc) technique. Photodetectors fabricated using the proposed material system with varying separation between the two materials, provides an excellent platform to study the ET process. Using this concept, we not only study the ET mechanism across the sharp organic-TMD interface but also use the hybrid platform to demonstrate the feasibility of the material platform for fabricating ultrasensitive photodetectors.

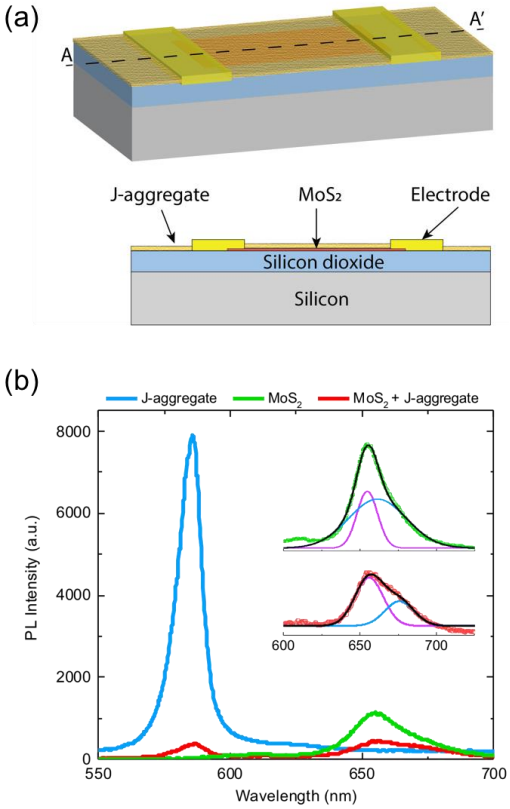

Figure 19: Monolayer MoS_2 photodetector sensitized by TDBC j-aggregate. (a) The schematic diagram of the device. (b) PL emission spectra from TDBC j-aggregate, monolayer MoS_2, and monolayer MoS_2/j-aggregate heterostructure. PL quenching is observed for both materials in the heterostructure region. The inset shows the Gaussian fitted neutral exciton (purple), trion (blue), and overall (black) peaks. The redshift of trion peak along with lowering of intensity of neutral exciton peak after TDBC j-aggregate deposition suggest n-doping of MoS_2 monolayer by TDBC j-aggregates.

Monolayers of MoS_2 were prepared on a 300 nm SiO_2/Si substrate using mechanical exfoliation and an all-dry transfer method. The dimensions of the monolayers ranged between 20 µm to 200 µm. Raman spectroscopy and atomic force microscopy (AFM) was used for confirming the thickness of exfoliated samples. The thickness of the monolayers was measured to be approximately 0.7 nm, which matched well with values reported in literature.[96] Electrodes were fabricated on the MoS_2 monolayers by photolithography followed by metal deposition and lift off. The schematic diagram of the device is shown in Figure 19(a). J-aggregate film was deposited on top of the monolayer MoS_2 using layer-by-layer deposition by immersing the device alternately in TDBC and polyelectrolyte solutions.[97] A thin film of

5.5 bilayers was deposited on all devices. Further information on device fabrication can be found in supporting information.

The PL spectra of monolayer MoS_2, TDBC j-aggregate, and MoS_2/j-aggregate at a constant excitation density are shown in Figure 19(b). A significant decrease in the emission intensity of j-aggregate was observed in coupled MoS_2/j-aggregate hetero-region. As mentioned earlier, near perfect spectral overlap between j-aggregate PL and monolayer MoS_2 absorption provides a suitable condition for the photo generated excitons in j-aggregate thin film to transfer its energy to MoS_2 layer through Förster Resonance Energy Transfer (FRET).[92, 94, 95, 98] ET through charge exchange can also occur at short distances due to wave function overlap through Dexter mechanism (DET).[99] Both mechanisms result in the significant decrease of j-aggregate PL emission intensity, as seen in Figure 19(b). In spite of the efficient ET from j-aggregate thin film, the monolayer MoS_2 PL appears to be quenched. This PL quenching is due to the charge transfer across the interface and has been reported as mutual photoluminescence quenching[100] due to type II energy band alignment between two materials. To support the argument, the PL spectra from bare monolayer MoS_2 and monolayer MoS_2/j-aggregate hetero-junction are fitted with two Gaussians corresponding to neutral and charged exciton (trion) as shown in the inset of Figure 19b. The hetero-junction PL shows a red shifted trion peak and a reduced neutral exciton peak intensity suggesting *n-doping* of MoS_2 by j-aggregate thin film. This agrees well with reported work on doping dependent PL of TMDs.[101, 102]

The photoresponse of the intrinsic MoS_2 devices were measured under room temperature and ambient condition. An ON/OFF ratio of 10^7 and a photoresponsivity of ~20 A/W at 595 nm (corresponding to *B-exciton* peak) with a drain-source bias of 10 V and a back-gate voltage of 10 V was measured. Similar measurements were preformed after j-aggregate deposition in an inert nitrogen atmosphere to prevent photo oxidation. The deposited j-aggregate film is expected to absorb nearly 40 % of incident light at 590 nm and about 33 % at 595 nm (*B* exciton peak of MoS_2), contributing to the enhancement of the photoresponse of MoS_2 monolayer photodetector. Figure 20(a) compares the IV characteristics of a MoS_2 photodetector before and after j-aggregate deposition with a drain-source bias of 10 V and illumination at 595 nm (power density of 0.025 W/cm^2). As expected, higher photocurrent I_{ph}, which is defined as ($I_{light} - I_{dark}$), was observed in hybrid devices due to ET mechanisms discussed earlier. In addition, increase in the dark current after j-aggregate deposition is observed indicating *n-doping* of MoS_2 monolayer by TDBC molecules.

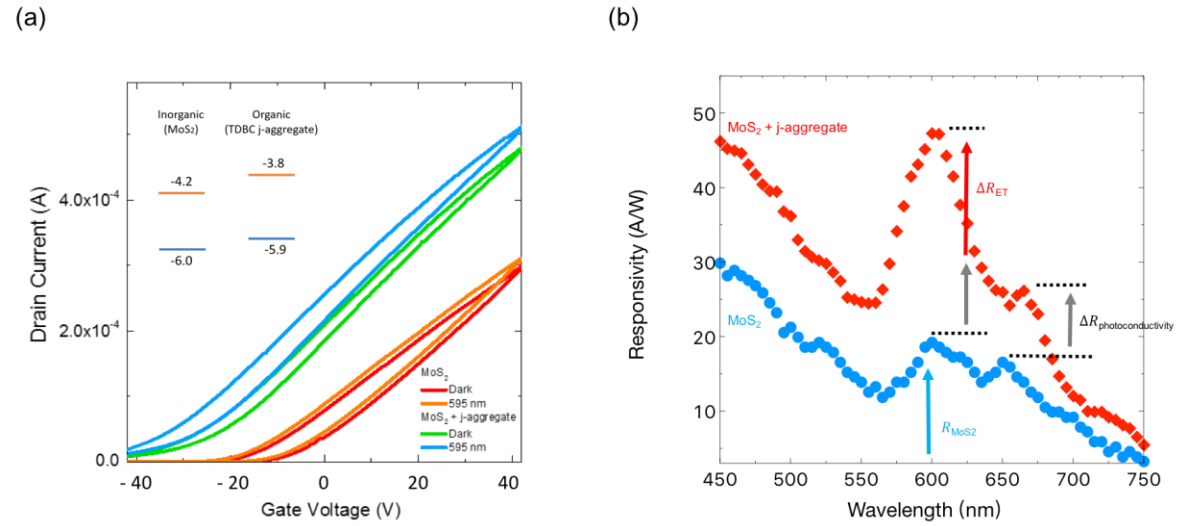

Figure 20: Enhanced photoresponse of monolayer MoS_2 photodetector after TDBC j-aggregate deposition. (a) IV characteristics of the photodetector before and after j-aggregate deposition. The excitation wavelength is 595 nm. Inset: optical band gaps of monolayer MoS_2 and TDBC j-aggregate show type II energy band alignment between two materials. (b) Wavelength dependent photoresponsivity before (blue) and after (red) j-aggregate deposition. The responsivity enhancement near j-aggregate absorption has contributions from ET and photoconductive gain increase, as shown in the figure.

Photoresponsivity (defined as the ratio of I_{ph} to incident power) of the photodetector before and after j-aggregate deposition were measured across the visible range (450-750 nm) as shown in Figure 20(b). The blue dots and red squares correspond to the bare MoS_2 and MoS_2/j-aggregate devices respectively. An overall enhancement in responsivity was observed across the spectrum. This was mainly due to the change in the photoconductive gain of the photodetector.[103] The photoconductivity gain is proportional to the dark current of the device and hence contributes equally throughout the spectrum above the lowest excitonic energy state (*A-exciton*).[104, 105] However, a much higher enhancement in responsivity was observed corresponding to j-aggregate absorption. The extra enhancement is attributed to the efficient ET from j-aggregate to MoS_2. We note that there is a small enhancement contribution to photoresponsivity at shorter wavelengths due to ET from the long absorption tail of the j-aggregate. Hence, to quantify the ET contribution at *B-excitonic* resonance, we subtract the overall responsivity enhancement by the enhancement at *A-excitonic* resonance. The enhancement seen at the *A-excitonic* resonance of MoS_2 is mostly due to photoconductivity gain. The enhancement due to ET, defined as the ratio of change in photoresponsivity after depositing j-aggregate (ΔR_{ET}) to the original bare MoS_2 (R_{MoS_2}) photoresponsivity is given by:

$$\boldsymbol{E_{ET}} = \frac{\Delta R_{total} - \Delta R_{photoconductivity}}{R_{MoS_2}} = \frac{\Delta R_{ET}}{R_{MoS_2}} \qquad (4.1)$$

A maximum enhancement of 93 ± 5 % at 600 nm was estimated due to the efficient ET between the dye molecules and the semiconducting monolayer. Both FRET and DET mechanisms contribute to the enhancement due to the proximity of the two materials. The maximum enhancement wavelength should correspond to the peak absorption wavelength of j-aggregates (590 nm). However, red shift (corresponding to the maximum enhancement wavelength) in j-aggregate absorption spectra was observed upon deposition over MoS_2 (confirmed from reflectivity measurements in supporting information). Similarly, red shift in MoS_2 *A-excitonic* resonance was also observed upon j-aggregate deposition as shown in Figure 20(b) due to the change in the dielectric screening. Similar shift is expected for *B-excitonic* resonance as well.

To quantify the FRET mechanism across the organic-inorganic interface, spacing between the MoS_2 monolayer and j-aggregate thin film was varied by introducing hexagonal Boron Nitride (h-BN) layers with varying thickness of 1.6, 2, 3, 5, and 10 nm. The thickness of each h-BN flake was measured by AFM. Figure 21(a) shows the schematic diagram for the hybrid photodetector with h-BN spacer along with a bright field image of the device with a 2 nm h-BN spacer. The h-BN flakes were introduced using the same approach as MoS_2 monolayers. h-BN is a two-dimensional insulator with a single layer thickness of approximately 0.4 nm and a bandgap of 6 eV[106, 107]. Thus, h-BN spacer prevents Dexter transfer (up to 1 nm) between the materials and helps to isolate the system to study the FRET process ($\boldsymbol{E_{ET} = E_{FRET}}$). We observed enhancement of MoS_2 PL for samples with thin hBN spacers (1.6 nm) confirming suppression of charge transfer and dominance of FRET (refer supporting information). FRET is a non-radiative emission-reabsorption process through a virtual photon that can occur within 10 nm of donor-to-acceptor

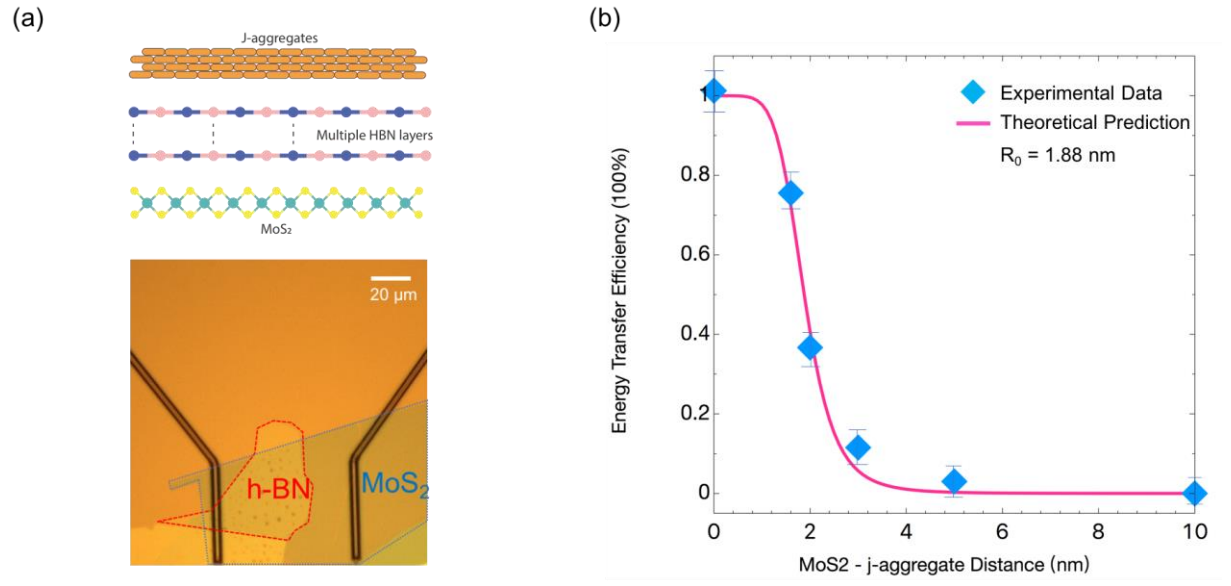

Figure 21: FRET efficiency between monolayer MoS_2 and TDBC j-aggregate film. (a) Schematic diagram showing the use of layered h-BN as a spacer and an optical image of a represented device with a 2 nm h-BN transferred on top of MoS_2. (b) FRET efficiency as a function of separation between MoS_2 monolayer and j-aggregate film. The solid line denoted the expected dependence using FRET theory.

distance.[95] To compare various devices, an optical excitation spot of 10 μm in diameter was used to illuminate specific regions of the sample and the devices were measured at a fixed current density of 10^{-8} A/μm^2 and a gate voltage of 10 V.

The FRET efficiency (η_{FRET}) can be derived from the responsivity enhancement by:

$$\eta_{FRET} = \frac{E_{FRET}}{6.3 * \eta_j * \kappa^2} \quad (4.2)$$

where $\eta_j = 0.2$ is the quantum yield of j-aggregate,[108] κ^2 is the dipole orientation factor,[109] and 6.3 is the absorption ratio of j-aggregate to MoS_2 at maximum responsivity (the maximum responsivity occurs at the maximum absorption of j-aggregate film). Since excitons in MoS_2 and j-aggregates are limited in-plane, we estimated the dipole orientation factor to be 0.7[110–112]. This is slightly higher than the generically used value of 2/3 for isotropic case. Figure 21b plots the FRET efficiency for photodetectors with different h-BN thicknesses. The figure compares the measured data with values estimated using FRET theory, where FRET efficiency is given by:

$$\eta_{FRET} = \frac{1}{1+(\frac{r}{R})^6} \quad (4.3)$$

where *r* is the donor-to-acceptor separation, and *R* is the Förster radius. *R* is defined as the distance where 50% of the energy is transferred from the donor to the acceptor molecule. The FRET radius for the TDBC j-aggregate – MoS_2 pair was estimated to be 1.88 nm across the hybrid interface. Typical FRET radius between organic-organic molecules lie between 2 to 7 nm[113]. Our experimental results show a smaller FRET distance in this hybrid organic-inorganic system which tallies with previous theoretical study.[114] This is possibly due to the small exciton Bohr radii as well as the well aligned orientations of excitons in both materials systems. The closely fitted experimental data along with their corresponding theoretical values shown in Figure 21(b) confirm that FRET dominates between the j-aggregate film and MoS_2 monolayer as the separation between them becomes larger than 1 nm. Less than 3% of the absorbed energy was transferred to the MoS_2 monolayer for donor-acceptor separation larger than 5 nm. As observed, the efficiency is close to 100 % for the devices without h-BN due to contributions from both FRET and DET mechanisms.

While we now have a good understanding on the energy transfer across the hybrid interface, the transport at the interface remains unknown. Knowing the transport properties will enable us to determine the feasibility of using the material system for studying exciton dynamics.

Transport at Hybrid Interface:

The charge transfer process has been found to be extremely fast (on the order of a few pico-seconds or less)[86, 115–118] across type-II hybrid organic-TMD heterointerfaces. Due to the interfacial Coulomb potential, the spatially separated electron and hole form a tightly-bound excitons with binding energies of hundreds of millielectron volts.[115, 119] While such interlayer excitons, also referred to as hybrid charge transfer excitons (HCTE), have been reported across hybrid organic-TMD heterostructures before, the energy transport associated with HCTE states combining Frenkel excitons in organics and Wannier-Mott excitons in inorganics remains an underexplored territory of research. This is especially true in the time regime immediately following the formation of HCTE states, where ultrafast transport has been observed.[115] Unraveling the unknown physics associated with such ultrafast transport of HCTE is imperative to the development of a material platform for next generation energy conversion and optoelectronic devices with superior and targeted performance. In this work, we study the transport of HCTEs in the sub-nanosecond time regime following optical excitation at a hybrid organic-inorganic heterojunction, featuring single layer molybdenum disulfide (MoS_2) and a highly absorbing j-aggregate thin film of organic dye TDBC (5,6-dichloro-2[3-[5,6-dichloro-1-ethyl-3-(3-sulfopropyl)-2(3H)-benzimidazolidene]-1-propenyl]-1-ethyl-3-(3-sulfopropyl) benzimidazolium hydroxide), to understand the contribution behind the observed ultrafast exciton transport. Our findings suggest the formation of fast-moving *hot* HCTE states as the primary reason behind the ultrafast transport and phonon bottleneck causing the slow thermalization of those *hot* HCTE states.

Figure 22(a) shows a schematic illustration of the hybrid 2D interface. The efficient energy transfer reported earlier enables the experiment to be performed at much lower excitation densities (avoiding sample damage). The heterojunction was formed by mechanically exfoliating a MoS_2 monolayer on a cover glass, followed by a layer-by-layer deposition of a thin layer (~5 nm) of j-aggregate.[97] Figure 22(b) shows the PL spectra of the hybrid structure. Upon deposition of the j-aggregate film, a new peak at around 760 nm (1.63 eV), corresponding to the HCTE state was observed in the heterojunction's PL spectrum. The inset shows the type II energy band alignment of the hybrid heterojunction forming the HCTE. The offset (0.28 eV) between MoS_2 valence band and j-aggregate highest occupied molecular orbital (HOMO) is greater than MoS_2 *A* exciton binding energy (0.27 eV), thus providing the driving force for *A* exciton dissociation and hole transfer. A similar mechanism applies to j-aggregate electron transfer upon photoexcitation. The charge transfer is confirmed by their respective PL quenching. We note that the j-aggregate PL spectrum remains unchanged in the presence/absence of MoS_2 except for the intensity drop due to charge transfer. Figure 22(c) shows the spectrally-integrated PL intensity map of HCTE emission under 532 nm CW

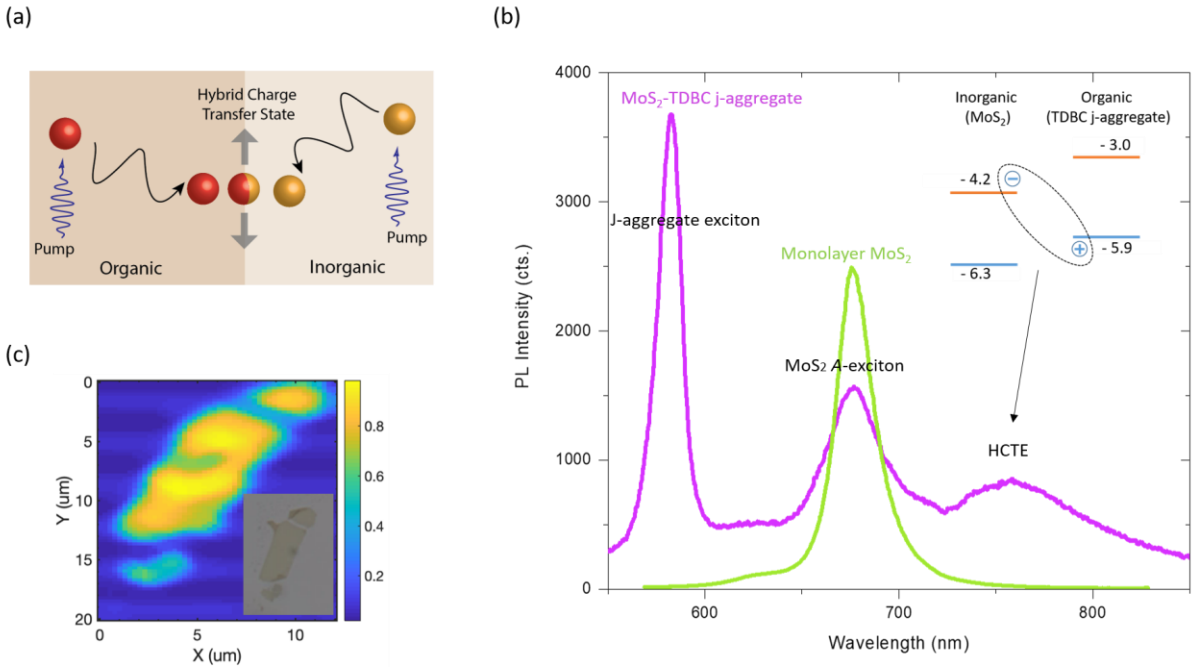

Figure 22: Charge transfer exciton in hybrid TDBC j-aggregate and MoS_2 2D interface. (a) Schematic illustration demonstrating the formation of hybrid charge transfer excitons (HCTE). The HCTEs consist of electrons from MoS_2 conduction band and holes from j-aggregate's HOMO. (b) PL spectra of monolayer MoS_2 (green) and hybrid MoS_2/j-aggregate heterojunction (purple) with a 532 nm CW laser excitation. MoS_2 A exciton at 670 nm and TDBC j-aggregate emission at 590 nm are identified in the hybrid sample. The third resonance at 760 nm is the HCTE formed by charge transfer across the hetero-interface with type II energy band alignment, as shown in the inset. Due to favorable energy levels, interfacial transfer of electrons to MoS_2 and holes to j-aggregate occurs within a few pico-seconds after excitation. (c) PL peak intensity map of the hybrid MoS_2 and j-aggregate at the HCTE wavelength range. The HCTE emission is observed throughout the entire MoS_2 flake as confirmed by the inset optical image of the monolayer.

photoexcitation. The emission of the HCTE state is observed across the entire MoS_2 flake as confirmed by the inset micrograph image of monolayer MoS_2 on cover glass.

Formation of HCTEs:

We estimate the formation efficiency of HCTEs by adopting an indirect approach based on aggregate time-resolved photoluminescence (TRPL) measurements. The TRPL dynamics (measured using time-correlated single photon counting (TCSPC) with a pulsed 405 nm laser) of j-aggregate's singlet excitons (595 nm), MoS_2 *A* excitons (670 nm), and HCTEs (760 nm) are shown in Figure 23(a). Due to the its spatially indirect nature, the HCTE exhibits an overall lifetime of 0.28 ns that is longer than that of j-aggregate and MoS_2's *A* exciton's lifetime. Inset of Figure 23(a) shows that the HCTEs are formed 40 ps after the laser excitation (the maximum value of TDBC j-aggregate's TRPL intensity is referenced as t = 0 throughout the manuscript). A similar delay was measured across several samples with an average formation delay of 36 $\pm$ 6.8 ps for the HCTEs.

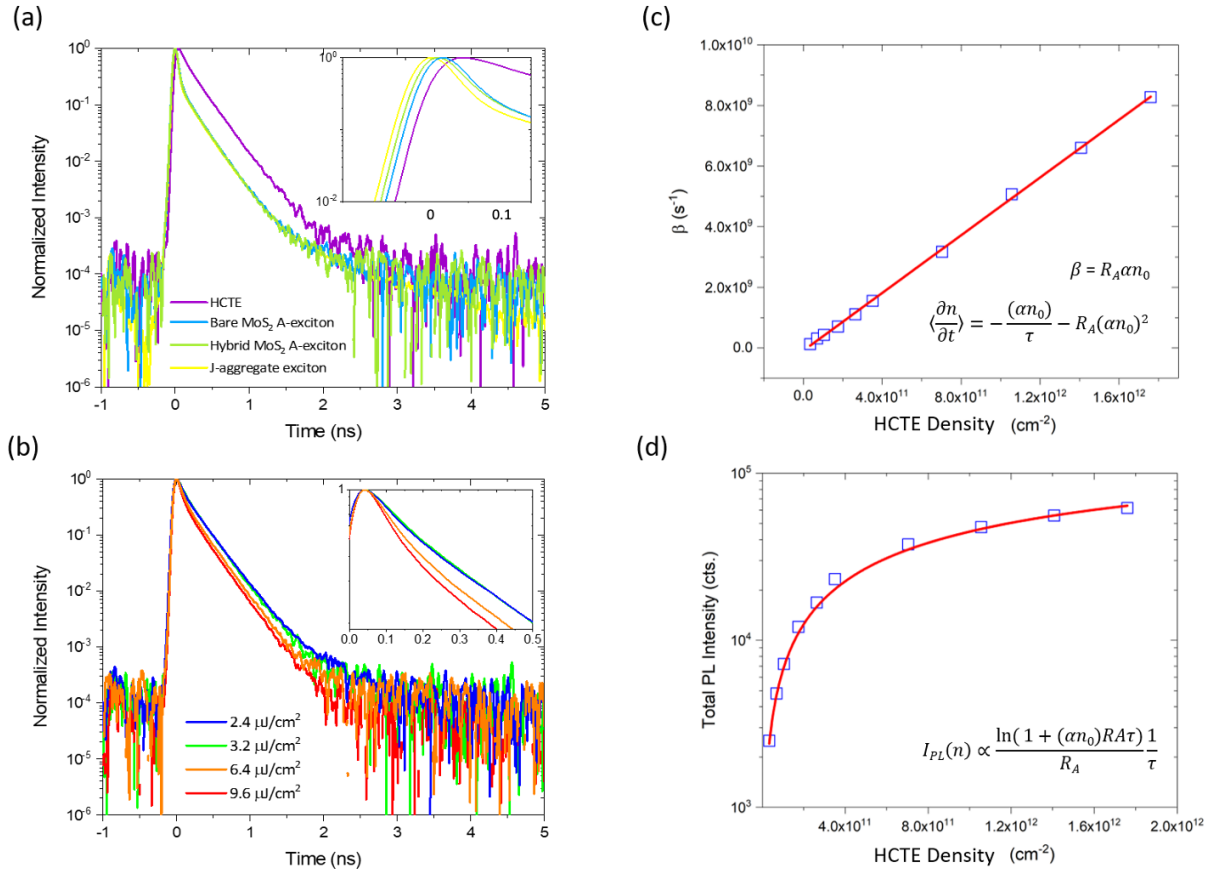

Figure 23: Lifetime and formation efficiency of HCTEs (a) Time-resolved PL dynamics of j-aggregate exciton, MoS_2 A exciton in bare monolayer and in the hybrid film, and HCTE. HCTEs decay much more slowly than A excitons due to their interlayer formation. The inset highlights the significant formation delay of HCTE of 40 ps as compared to j-aggregate excitons. (b) Time-resolved PL measurements of HCTEs at different excitation densities. The exciton density decay rate increases as the excitation power density increases, which can be attributed to Auger recombination. HCTE lifetime fitting with (c) exciton recombination rate and (d) PL yield. Both equations are functions of the Auger constant R_A, exciton lifetime τ, and HCTE density n (αn_o). Note that n_o is the density of all absorbed photons on the hybrid sample, and α is the formation ratio of HCTE. By fitting our data with the intensity and lifetime models, we find a single α that can satisfy both equations with identical Auger constant R_A. HCTE formation efficiency of 40% and Auger coefficient of 0.005 cm^2/s were estimated.

Next, we monitor the excitation density dependent TRPL of the HCTE as shown in Figure 23(b). The initial HCTE population decay rate increases with increasing excitation density, as emphasized in the inset plot, due to increased non-radiative contribution from Auger recombination (exciton-exciton annihilation). Such time evolution of the HCTE population can be modeled with the following rate equation:[37, 120]

$$\frac{\partial n}{\partial t} = -\frac{(n)}{\tau} - R_A(n)^2 \qquad (4.4)$$

where n is the HCTE density, τ is the exciton lifetime, and R_A is the Auger coefficient. We note that the TRPL data shown in Figure 23(a) and (b) were obtained by summing up the PL intensities of all the spatially diffused excitons, eliminating the need to include the diffusion term in equation (4.4). We define the HCTE density as $n \equiv \alpha n_0$, where n_0 and n are the density of absorbed photons and corresponding HCTEs

respectively, and α is the formation efficiency of HCTEs. In addition, the steady state PL intensity of excitons in the presence of Auger recombination can be modelled as:[120]

$$I_{PL}(n) \propto \frac{\ln(1+(n)R_A\tau)}{R_A}\frac{1}{\tau} \tag{4.5}$$

We fit the experimental data with equations (4.4) and (4.5) simultaneously and extract the HCTE formation efficiency of 40% and an Auger coefficient of 0.005 cm^2/s. The fitting curves obtained from the solution to equation (4.4) given by:

$$n(t) = \frac{n_0}{e^{\left[\left(\frac{t}{\tau}\right)(1+n_0R_A)\right]} - n_0R_A\tau} \tag{4.6}$$

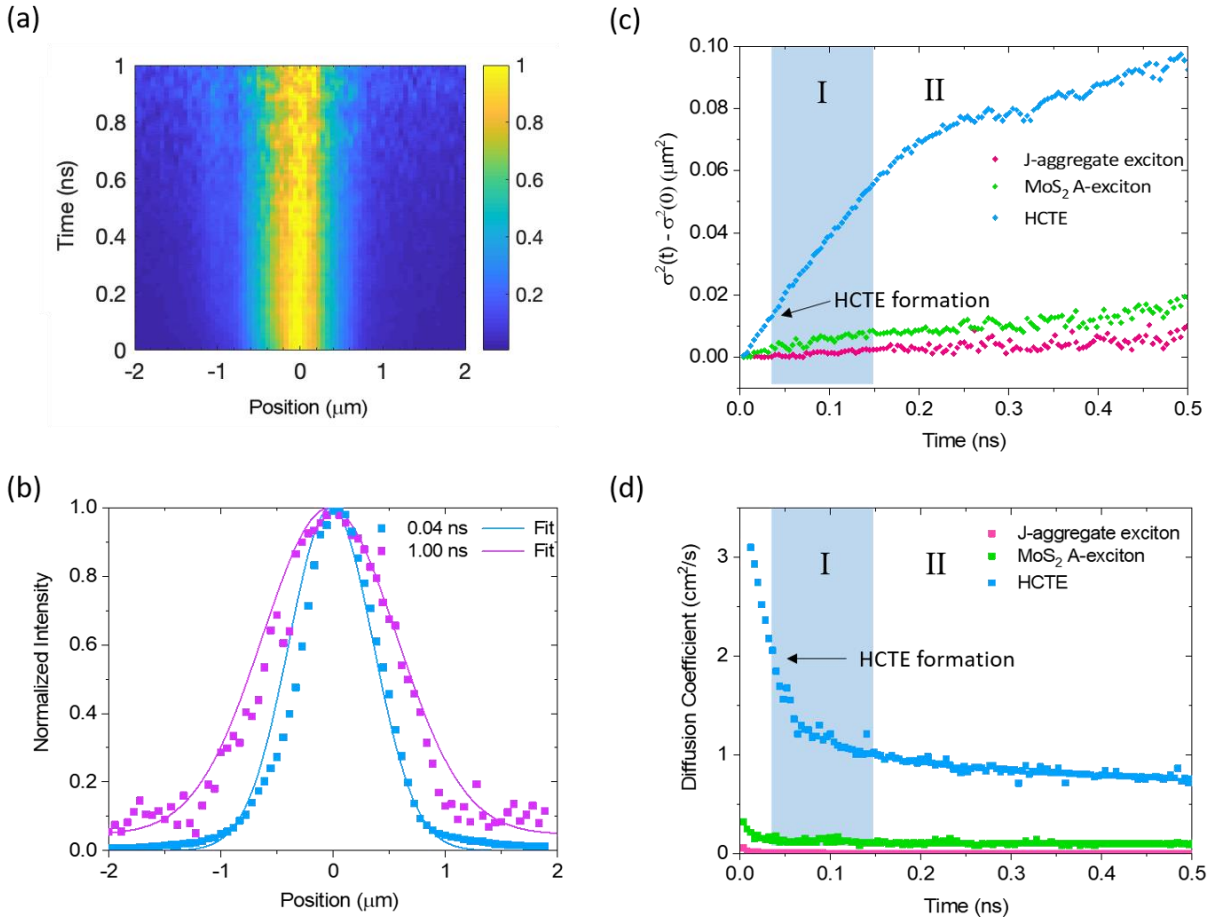

Figure 24: Transport of j-aggregate exciton, MoS_2 A exciton, and HCTE. (a) Temporally and spatially resolved exciton density map of HCTE. The data were obtained by TCSPC and a 405 nm pulsed laser. Highly diffusive HCTEs are observed compared to non-mobile j-aggregate and MoS_2 A excitons (Figure S4). (b) Normalized HCTE population profiles extracted from (a) at 0 ns (blue) and 1 ns (purple), respectively. At 0 ns, j-aggregate has the largest spot (FWHM of 0.85□m) while MoS_2 A exciton has the smallest (FWHM of 0.6□m) as shown in Figure S4. (c) MSD change of exciton density as a function of time. HCTEs diffuse faster within region I, indicating contributions from both hot carriers and Auger scattering broadening. (d) Time dependent diffusion coefficients. HCTEs diffuse an order of magnitude faster than MoS_2 A excitons. J-aggregate excitons are immobile.

and equation (4.4) and (4.5) are shown as solid lines in Figure 23(c) and (d), respectively. It is worth noting that the Auger recombination rate of HCTEs at the current hybrid interface is an order of magnitude lower than the rate of MoS_2 *A* exciton. The technique outlined here demonstrates a simpler alternative to the complex pump-probe techniques typically used to estimate exciton formation efficiencies.

Transport of HCTEs:

Figure 24(a) shows the temporally and spatially resolved PL intensity map of HCTEs obtained using a diffusion imaging microscope reported in our earlier work[121] (excitation fluence of 3.2 μJ/cm^2 and a corresponding HCTE density of 3.52×10^{11} cm^{-2} using a pulsed 405 nm laser). Figure 24(b) plots the exciton distribution at different times emphasizing the broadening of the initial distribution. The evolution of the exciton population's spatial profile created by a laser with a Gaussian intensity profile can be described with the equation:[37]

$$n(x,t) = \frac{n_{\mathrm{i}}}{\sqrt{4\sigma Dt}} exp\left(\frac{x^2}{2\sigma^2(0)+4Dt}\right) \quad (4.7)$$

where *D* is the diffusion coefficient, n_i is the initial total exciton density, *t* denotes the time, and $2\sigma(t)$ is the FWHM of the Gaussian exciton density profile. Using this result, the time-dependent mean-squared displacement (MSD) change of the exciton density (defined as $[\Delta x^2(t)] \equiv \sigma^2(t) - \sigma^2(0) = 2Dt$) can be calculated and the diffusion coefficient can be extracted. However, in a 2D semiconductor system with intrinsic defects and impurities, the diffusion process is not linear with time and the MSD change is better described by the power law $[\Delta x^2(t)] = Gt^{\alpha}$, where G and α are the transport factor and anomalous coefficient,[122] respectively. The time-dependent diffusion coefficient is then defined as $D(t) = (\alpha G t^{\alpha-1})/2$.

Figure 24(c) and (d) plot the MSD of the exciton density distribution and the extracted time dependent diffusivity as a function of time respectively for j-aggregate excitons, MoS_2 *A* excitons, and HCTEs. Initially, HCTE are highly mobile when compared to j-aggregate and MoS_2 *A* excitons (we note, that while j-aggregate excitons do not diffuse much, the initial exciton density distribution is largest (0.85 μm with 0.5 μm excitation spot) for j-aggregates. This is consistent with reported ultrafast diffusion of excitons in j-aggregates in short time scales that are not captured in the current experiments).[88] We notice a non-linear evolution of MSD for HCTEs, characterized by two regimes (after the formation of HCTE states) (I) 40-150 ps (110 ps) of highly mobile HCTEs, and (II) slow moving HCTE states where diffusivity appears to asymptote to 0.77 ± 0.21 cm^2/s, a value that is higher than MoS_2 *A* excitons' diffusivity, indicating the intrinsically more diffusive nature of HCTEs in the TMD/organic system. The observed nonlinearity in MSD could be explained by possible contributions from Auger broadening and/or *hot* exciton

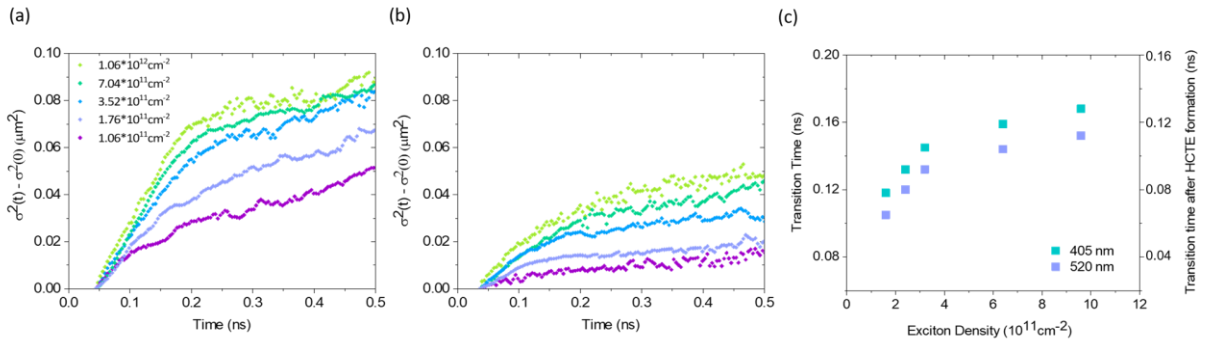

Figure 25: Highly mobile hot HCTEs. Power density dependent MSD of HCTEs as a function of time with (a) 405 nm pulsed and (b) 520 nm pulsed excitations. The curves with the same colors in (a) and (b) correspond to the same exciton densities, and thus same Auger recombination rates. Despite having same exciton-exciton annihilation rate, MSD of HCTEs pumped with 405 nm laser is still larger than that pumped with 520 nm laser in region I, confirming the contribution from hot HCTEs. (c) Hot exciton relaxation times (transition time) versus excitation fluences. We observe evidence of saturation above exciton densities of 4×10^{11} cm^{-2}.

transport.[123] Auger broadening is caused by exciton-exciton annihilation.[124] Due to higher exciton density at the center of the excitation beam, the exciton-exciton annihilation rate is also higher, causing the PL intensity at the center to drop faster than at the surrounding area. As a result, the Gaussian exciton density profile appears to broaden faster. We estimate such contribution from the measured Auger coefficient and find that it is small below 3.52×10^{11} cm^{-2}. Nevertheless, minor contributions from Auger exists and cannot be easily subtracted from the data. On the other hand, since high energy photons (3.1 eV, much higher than MoS_2's optical band gap) are used to excite the sample, high energy excitons can be formed after interacting with phonons (in organics as well as in inorganics). These excitons with excess energy can dissociate into free *hot* carriers or form *hot* HCTEs (excitons with high kinetic energy). Since we know the HCTEs are formed in about 40 ps after photoexcitation as shown in Figure 23(a), we attribute the transport observed in regime I to be dominated by *hot* HCTE states. The higher diffusivity observed prior to regime I could possibly be due to *hot* carriers. However, we ignore the analysis in the short time regime as it is very close to the limits of the TCSPC technique. Further dissociation of HCTEs into free carriers, following its formation is also possible but unlikely due to high binding energy of HCTE (~90 meV based on energy level calculations and PL emission). However, in this case, we would expect the diffusivity to be similar to that observed prior to regime I and relaxation time to be much shorter, further justifying that the observed transport is from HCTEs.

We also studied the effect of excitation photon energy and density on transport. The fluence dependent MSD of HCTE as a function of time using 3.06 eV (405nm) and 2.38 eV (520 nm) pulsed lasers are shown in Figure 25(a) and (b). The curves with the same color from Figure 25(a) and (b) correspond to the same HCTE density. This condition is achieved by exciting the samples with fluences that result in identical rates of emission of HCTE photons in both cases. The inset numbers in Figure 25(a) are the HCTE densities. Furthermore, the ratio of average power of the 520 nm to 405 nm lasers remained constant (2.7

$\pm$ 0.12) throughout the measurements, confirming that the contribution from Auger broadening remained identical for each excitation fluence as the Auger scattering rate is proportional to exciton density only.[124] Under such condition, we observed that the net MSD and rate of change of the MSD (corresponding to diffusivity) of HCTEs pumped with 405 nm laser was larger than their MSD rate of change when pumped with the 520 nm laser despite having the same exciton-exciton annihilation rate, validating the conclusion of *hot* exciton transport as the responsible mechanism for the high diffusivity. In addition, we observe that the time for HCTE transport to transition from regime I (*hot*) to II (*cold*) was higher for 405 nm excitation than 520 nm excitation as shown in Figure 25(c), further supporting the existence of *hot* HCTEs as discussed in the next section.

Relaxation dynamics of HCTEs:

Figure 26 shows a schematic illustration of the plausible formation and relaxation paths of HCTEs at the organic-inorganic hybrid interface. Exciton formation in j-aggregates and MoS_2 is a very fast process and based on other reports,[88, 116, 117] we expect charge transfer to occur within the first few picoseconds after optical excitation[117] across the hybrid interface due to the favorable energy band alignments and form high energy HCTEs. The higher HCTE states have lower binding energy than MoS_2 excitons and hence there is a high probability of dissociation into *hot* carriers. Whether the relaxation from higher-energy HCTE states to the lowest-energy HCTE state is mediated through *hot* carriers or directly through bound CT states remains unclear. In either case, the relaxation creates lowest-energy HCTEs that possess non-zero kinetic energy, which results in the observed ultrafast transport. The relaxation rate of such *hot* HCTEs to *cold* HCTEs is (step 3 in Figure 26) governed by exciton-phonon interactions.[125–130] If the dielectric screening is small, the direct effect of the dipole field can dominate, and so the polar

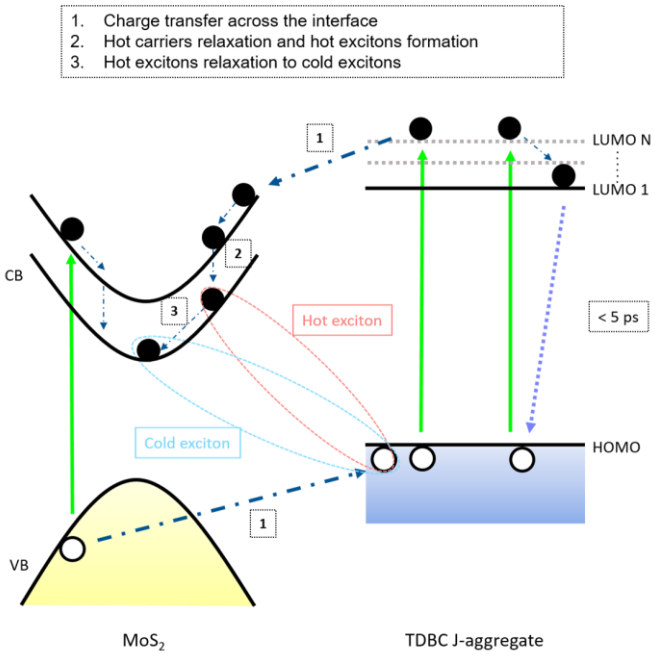

Figure 26: Hot exciton formation and relaxation paths for HCTEs. J-aggregate and MoS_2 exciton formation is instantaneous (compared to the time-scales of our measurement) after photoexcitation with a 3.1 eV source. 1. Within a few pico-seconds, interfacial charge transfer occurs due to the energy band alignment as electrons move to the conduction band of MoS_2 while holes move to the HOMO of j-aggregate. The j-aggregate lifetime is less than 5 ps. 2. The hot carriers of MoS_2 relax and form hot HCTEs within the first 40 ps assisted by polar optical phonons. 3. The hot excitons then relax their extra energy through acoustic exciton-phonon scattering, as discussed in the main text.

optical phonon (LO) interaction is typically the major scattering channel in polar materials at room temperature, which best describes our case and is confirmed from our theoretical calculations detailed in the supplementary materials. It is worth noting that the transition time of *hot* HCTEs is longer than that of *hot* MoS_2 *A* excitons at an excitation density of 3.2 μJ/cm^2. A similar trend is observed with higher power densities. Such variation in transition time stems from different extents of exciton-phonon interactions and can be better understood by estimating the relative strength of the Fröhlich and deformation potential interactions for MoS_2 *A* and HCT excitons with optical and acoustic phonons.

The Fröhlich optical phonon coupling model for charge carriers defines a dimensionless coupling constant δ that depends on the carrier mass and the dielectric environment.[131–136] An estimate of the exciton-phonon Fröhlich interaction strength can be obtained with a modified version of the Fröhlich coupling constant defined as:

$$\delta = \left| \frac{e^2}{2\hbar} \sqrt{\frac{2M}{\hbar\omega_{LO}}} \left(\frac{1}{\varepsilon_\infty} - \frac{1}{\varepsilon_0} \right) \right| \tag{4.8}$$

where ε_0 is the static dielectric constant, ε_∞ is the optical dielectric constant, M is the translational mass, and ω_{LO} is the LO phonon angular frequency. A larger δ suggests a stronger exciton-phonon interaction that will result in a faster relaxation. With the assumption that the MoS_2 monolayer and HCTE experience identical dielectric environments and interact with the same optical phonons, the ratio of the Fröhlich constants depends solely on the ratio of the exciton translational masses, as shown below:

$$\frac{\delta_{CT}}{\delta_{MoS_2}} = \frac{\left| \frac{e^2}{2\hbar} \sqrt{\frac{2M_{CT}}{\hbar\omega_{LO}}} \left(\frac{1}{\varepsilon_\infty} - \frac{1}{\varepsilon_s} \right)_{CT} \right|}{\left| \frac{e^2}{2\hbar} \sqrt{\frac{2M_{MoS_2}}{\hbar\omega_{LO}}} \left(\frac{1}{\varepsilon_\infty} - \frac{1}{\varepsilon_s} \right)_{MoS_2} \right|} \approx \sqrt{\frac{M_{CT}}{M_{MoS_2}}} \tag{4.9}$$

While we are not able to estimate the translational mass of HCTEs due to the lack of hole effective mass in j-aggregate form, we expect the translational mass of HCTEs to be considerably lower than the translational mass of MoS_2 excitons since HCTEs are characterized by their exceptionally high diffusivities. However, it remains unclear why HCTEs have small translational mass. Complex molecular dynamics simulations could provide insight but remains beyond the scope of the current work. As a result, we expect the Fröhlich coupling of HCTEs to be weaker than the Fröhlich coupling of MoS_2 excitons, resulting in a longer relaxation time for HCTEs. However, the Fröhlich coupling constant of MoS_2 *A* exciton, estimated to be 19.1 and corresponding to femtosecond relaxation time as detailed in the supplementary section, cannot explain the 100 ps relaxation that we observed. This suggest that at 300 K, the Fröhlich interaction is the dominant exciton-phonon scattering mechanism until the exciton's excess energy drops below the optical

phonon energy. Once below the optical phonon energy, the excess exciton energy is relaxed *via* the slower acoustic phonon scattering process (relaxation time for MoS_2 exciton *via* acoustic phonon scattering is in the sub picosecond regime).

Using the expressions for carrier-phonon scattering rate *via* the deformation potential interaction with the substitution of exciton translational mass for effective carrier masses, the ratio of acoustic phonon scattering rates of MoS_2 excitons and HCTEs depends on the ratio of their respective elastic properties, exciton translational masses, and deformation potential differences as shown below (refer to the supplementary material for more details):

$$\frac{\left(\frac{1}{\tau_{\mathbf{k},LA}}\right)_{CT}}{\left(\frac{1}{\tau_{\mathbf{k},LA}}\right)_{MoS_2}} = \frac{M_{CT}}{M_{MoS_2}} \frac{\rho_{MoS_2} s_{MoS_2}^2}{\rho_{CT} s_{CT}^2} \frac{\left(\Xi_{1,e} - \Xi_{1,h}\right)_{CT}^{\ 2}}{\left(\Xi_{1,e} - \Xi_{1,h}\right)_{MoS_2}^{\ 2}} \tag{4.10}$$

While we are unable to explicitly calculate the ratio of acoustic phonon scattering rates of HCTE and MoS_2 excitons due to the unavailability of hole deformation potentials and effective mass of TDBC J-aggregates, based on our experimental observations, we are able to estimate this ratio to be about 0.7. That is, HCTEs relax their excess energy *via* acoustic phonon scattering at a rate that is about 70% of the rate of MoS_2 excitons. This value corresponds to the ratio of the times at which the slopes of the MSD curves transition from their initial (high) to final (lower) value. We associate these transition times with the average exciton-acoustic phonon scattering times that characterize the pico-second time scales of *hot* exciton energy relaxation of our observations. It is worth noting that the calculations of average scattering time are estimates based on the expressions for carrier-phonon scattering and do not take into account other many-body interactions that may affect the relaxation dynamics of MoS_2 excitons. Therefore, those calculations serve as a qualitative rather than quantitative guide to explain the results.

Moreover, for a given optical phonon Fröhlich coupling constant, the transition time should be shorter when excited using lower energy photons due to the lower kinetic energy of excitons. This is consistent with our findings and is confirmed from the data shown in Figure 27(c). Furthermore, we observe that the time for HCTEs transport to transition from regime I to regime II increases linearly with exciton density. This trend is due to the limited phonon density of states available for relaxation, also referred to as phonon bottleneck.[137, 138] The transition time begins to saturate for higher excitation densities, which is possibly due to Auger recombination as more excitons begin to annihilate.[123] This is consistent with our observations: as contributions from Auger scattering become non-negligible at high exciton densities.

In conclusion, we show that the energy transport at organic-inorganic hybrid interfaces is dominated by HCTEs. We find that following photoexcitation, hot HCTEs are formed in about 36 ps via scattering

with optical phonons. Based on the estimated relaxation time for acoustic and optical phonon scattering processes via deformation potential and Fröhlich interaction, we conclude that once the energy falls below the optical phonon energy, the excess kinetic energy is relaxed slowly via acoustic phonon scattering. During this time, fast-moving, hot HCTEs dominate the energy transport. While there could be contributions from free carriers arising from dissociation of HCTEs, we believe it is small due to high binding energy of HCTEs. Further investigation based on temperature dependent transport measurements along with transient absorption spectroscopy could shed light into the distribution of free carrier and HCTEs. The transition to cold excitons occurred at about 110 ps after formation (which is much longer than what is typically observed at organic/organic interfaces) and increased with excitation density, suggesting phonon bottleneck. We note that the diffusivity of HCTEs in both of the regions of transport was higher than MoS_2 A excitons. This work not only provides significant insight into the initial energy transport of HCTEs at organic-inorganic hybrid interfaces, but also contributes towards forming a complete physical picture of HCTE dynamics from formation to recombination. In conjunction with phonon engineering, we believe such high diffusivities in hybrid structures could enrich the applications from energy conversion to optoelectronic devices.

5 Applications:

Here, we utilize our knowledge of nanoscale strain engineering to create a self-erasable and rewritable platform for anti-tamper hardware. The reversible structural change between *trans* and *cis* isomers in azobenzene (A3) molecules is utilized to strain the overlying tungsten diselenide (WSe_2) monolayer, thereby affecting its optical bandgap. Using such hybrid material combination we generate large (>1%) local effective strain that results in dramatic shift (> 11 nm) in photoluminescence wavelength. The strain in layered A3 films can be rapidly relaxed under exposure to visible light or can be retained up to seven days under dark condition. Thus, by utilizing hyperspectral imaging, we demonstrate a self-erasable and rewritable optoexcitonic platform that responds to environmental changes (light/temperature) to detect

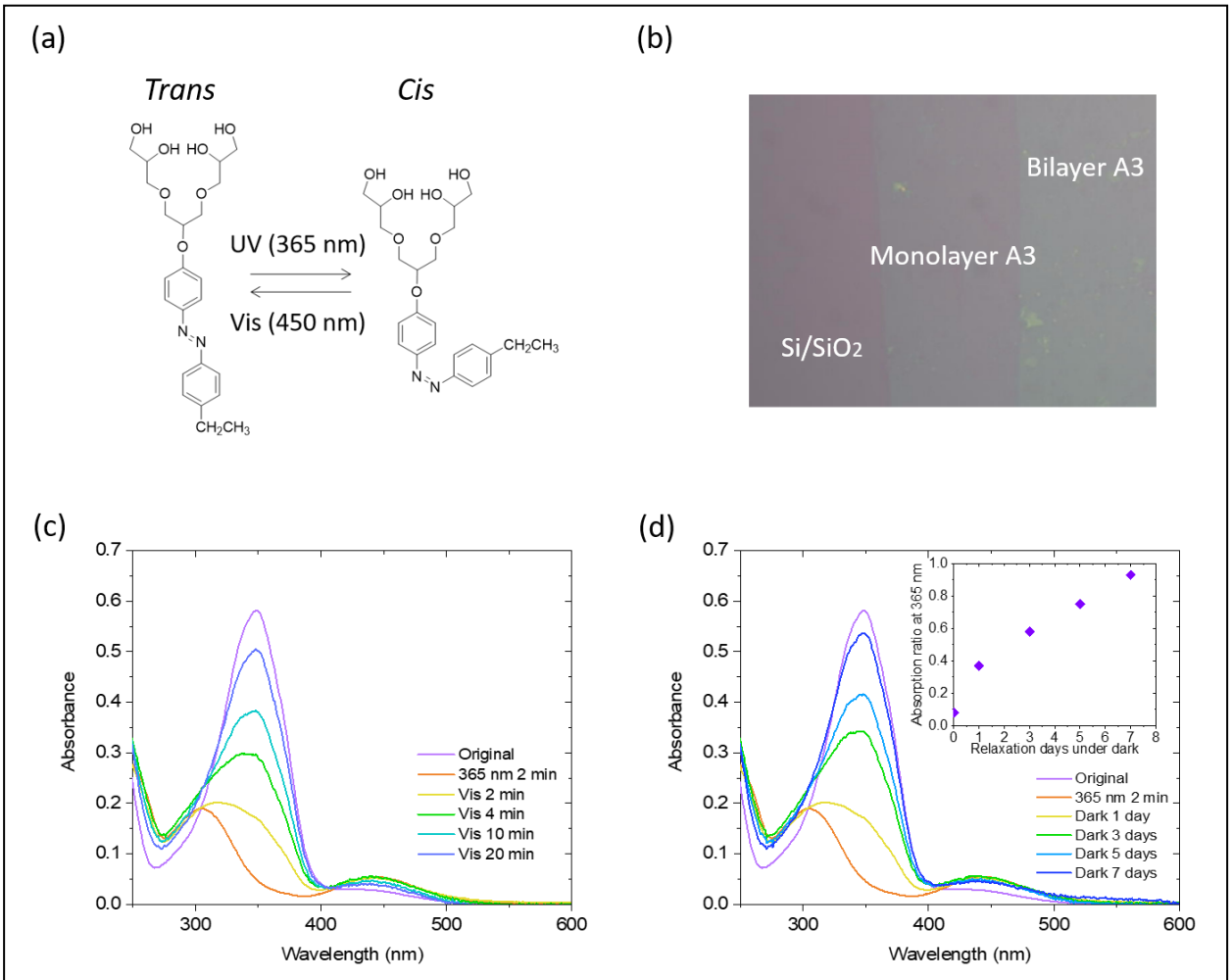

Figure 28: Photoisomerization of A3 films under visible light and dark environment at room temperature. (a) Chemical structures of A3 in trans and cis states. The thermally stable trans isomer (9 Å) can be switched to cis isomer (5.5 Å) upon UV irradiation, and reverted back gradually with visible light. (b) Optical micrograph of monolayer and bilayer A3 films on Si/SiO_2 substrate. The A3 films are prepared using Langmuir-Blodgett (LB) method. (c) UV-Vis absorption evolution of A3 film (5.4 nm) after UV treatment and visible light relaxation. (d) UV-Vis absorption evolution of the same A3 film under dark environment. The inset in (d) shows the percentage of cis A3 molecules relaxing back to tans state over time. It took 7 days for 95% of the A3 molecules to relax back to trans state under dark environment.

tampering of hardware system. In addition, the results open avenues for varied applications in information storage, time sensitive self-destructive memories to light detection.

In this work, we create a compact self-erasable and rewritable optoexcitonic platform using monolayer WSe_2 on top of thin layers of an azobenzene based molecule, (*E*)-3,3'-((2-(4-((4-ethylphenyl)diazenyl)phenoxy)propane-1,3-diyl)bis(oxy))bis(propane-1,2-diol) (A3) (Molecular structures of *trans* state and *cis* isomers are shown in Figure 28(a). We induce local strain in monolayer WSe_2 by photoactivating underlying A3 molecules with irradiation of UV light, followed by selective exposure to visible light that reversibly switch the molecules between *trans* and *cis* state. The resulting strain in monolayer WSe_2 shifts the optical bandgap thereby causing a spectral shift in the photoluminescence signal. The strain can be instantaneously released by exposure to visible light or gradually over a period of time due to thermal relaxation.

Figure 28(a) shows molecular structures of the azobenzene based molecule, A3, in *trans* state and *cis* state. The thermally stable *trans* azobenzene isomer undergoes structural change to *cis* isomer upon irradiation of UV light, resulting in reduction of molecular length from 0.9 nm to 0.55 nm. The reverse transformation is gradual at ambient environment conditions but can be expedited by intense visible light irradiation or heat. We note that, the reaction of *cis* state to *trans* state is a much slower process as compared to the reverse reaction. This is partially due to the relative high absorption strength of *trans* isomer in UV regime than *cis* isomer in visible regime and the spectral intensities of the light sources used in the experiments.

Figure 28(b) shows the optical micrograph of monolayer and bilayer A3 films deposited on Si/SiO_2 substrate using Langmuir-Blodgett (LB) method[139]. The A3 molecule is highly polarized with a hydrophobic head and a hydrophilic tail, and as a result uniform layers of A3 can be achieved through specified treatments. We monitor the A3 thin film isomerization dynamics over time using UV-Vis spectroscopy at room temperature. The UV-Vis absorption evolution of approximate 6 layers of A3 films (~12 nm) on cover glass following UV irradiation under visible light (Amscope series halogen lamp with an average fluence of $120 \mu W/cm^2$) relaxation is shown in Figure 28(c). We follow it by monitoring the transition under dark condition as shown in Figure 28(d). We observe that 99% of the molecules remain in *cis* state within first 120 minutes as compared to less than 1% when exposed to visible light. In fact, only 20% of the molecules relax back to *trans* state after 24 hours. The inset of Figure 28(d) plots the percentage of molecules relaxing back to *trans* state over 7 days. We observe that under dark conditions, 95% of the *cis* A3 molecules reverted back to *trans* state in 7 days. Thus, a message engraved on such an optoexcitonic platform would automatically disappear in about 7 days.

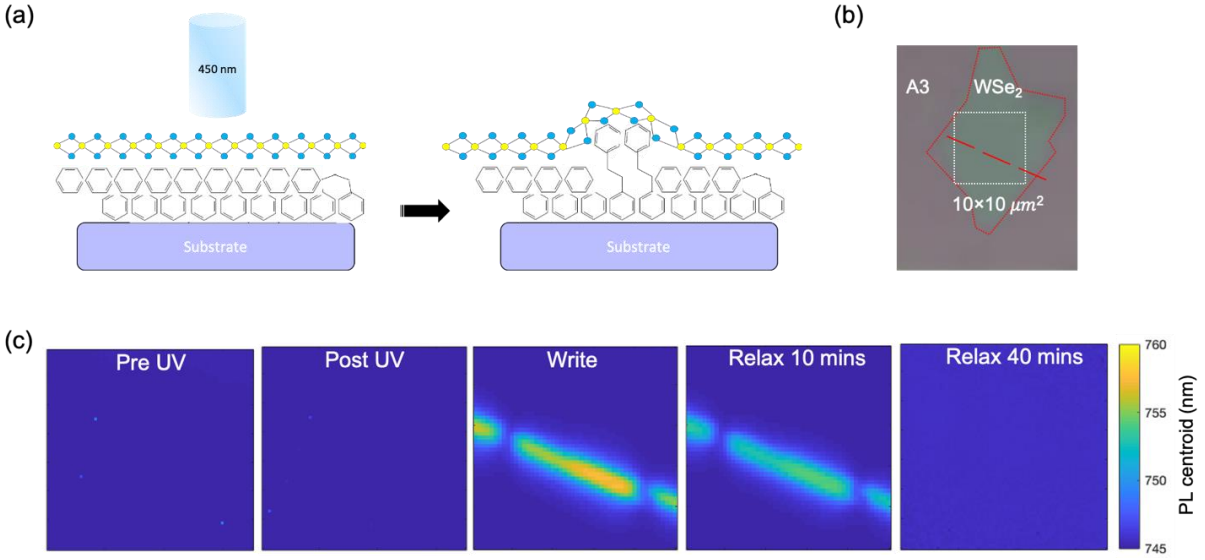

Figure 29: A3-initiated strain engineering on WSe_2 monolayer. (a) An illustration showing the creation of local strain on a monolayer WSe_2 by partially reverting some of the underlying cis molecules back to trans state using a 450 nm laser. We transfer a monolayer WSe_2 on top of bilayer A3 films and monitor the photoemission property. The induced strain in monolayer WSe_2 is translated into PL spectral shift. We observe a redshift of 11 nm that corresponds to 1.1% of tensile strain. The sample image is shown in (b). A sequence of PL spectral centroid map of the square region marked in (b) are shown in (c) where strained regions are mapped red shifted in energy indicating tensile strain. The sample is first irradiated with UV light for 5 minutes, where the complete underlying A3 bilayer undergoes trans to cis transformation that results in zero spectral shift in the PL spectrum. It is then followed by a writing process along the marked red lines in (b), where a 450 nm laser is used to partially relax the molecules back to trans state. This creates local strain as shown schematically in (a) and its effects are observed in the shift of the PL spectral centroid map. The strain resulted PL shift pattern disappears after 40 minutes of white light treatment.

The samples were prepared by first transferring a mechanically exfoliated monolayer WSe_2 on top of bilayer A3 films. The sample were then irradiated with 365 nm UV light (with an average fluence of 100 $\mu W/cm^2$) for 5 minutes to completely convert the underlying A3 bilayer to *cis* state. A 450 nm laser was then used to achieve targeted relaxation of some of the molecules as *cis* A3 molecules shows higher absorption at this wavelength among the visible regime. The selective relaxation thus created local strain on the overlying monolayer and the process is illustrated in Figure 29(a). We visualize the strain by conducting a sequence of PL spectral centroid map of the sample using a 532 nm excitation laser. The brightfield image of the sample is shown in Figure 29(b). The marked square region (10×10 μm^2) represents the scanned area for monitoring the PL shift, whereas the red line marks the linear profile scanned by the 450 nm laser during the write cycle. Figure 29(c) shows the PL centroid map monitoring the initializing of the film using UV, followed by the write cycle, and finally the relaxing phase. The transformation of all the molecules from *trans* to *cis* state is uniform and results in zero spectral shift in the PL spectrum as shown in Figure 29(c) (post UV). It is then followed by a write cycle, where a 450 nm laser (spot size of 2 μm, fluence of 25 $\mu J/cm^2$) is linearly scanned (dashed line) to create the local strain. Finally, the sample is exposed to white light to initiate relaxation and all the information is erased in ~ 40 minutes.

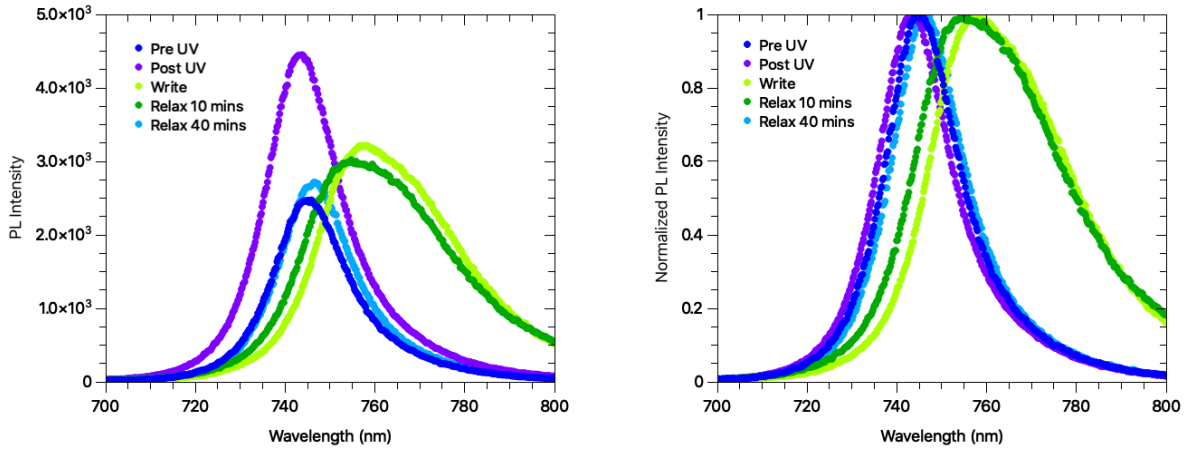

Figure 30: The PL spectral shift caused by strain in monolayer WSe_2. The spectra were taken at the center of the dashed line in Figure 2(c) for each step. (a) Non-normalized (b) Normalized PL spectra. We observe a redshift of 12 nm that corresponds to 1.1% of tensile strain in the writing phase. The PL redshift gradually disappears after relaxation process. The intensity drop at the strain area is caused by the direct to indirect transition of optical band gap in TMD monolayer.

The strained regions are red shifted in energy due to tensile strain generated on the monolayer during the process[34, 140]. Figure 30(a) shows the non-normalized PL spectrum of each step (on the dashed line). The observed PL intensity drop and broader linewidth after the write cycle (creation of local strain) are possibly due to contributions from the inhomogeneous broadening over the strained area as well as direct-to-indirect transition of the optical band gap of TMD monolayer under high strain. The observation is consistent with reported studies based on strain[141–143]. In fact, the observed redshift of 11 nm translates to a very high effective tensile strain value of ~1.1 %. The effective strain created by just 2 layers of A3 molecules (0.7 nm in isomerized length change) is significantly higher when compared to other reported studies that used mechanical setups to induce strain on TMDs. We also note that the PL intensity enhances from pre UV (*trans* state) to post UV (*cis* state) phase, and vice versa. This phenomenon has been observed by other group and is associated with doping in TMD materials[144, 145]. It has also been reported that azobenzene based molecules in *trans* state provide pathways for doping while the photoisomerization from *trans* to *cis* configuration weakens such pathways[146, 147]. In our case, the lowering emission intensity of WSe_2 monolayer by *trans* A3 molecules indicates p-doping where neutral excitons are suppressed by excess positive trions[144]. which is confirmed by the electric current-voltage transfer characterization.

To further quantify the strain relationship with the underlying layer, we transfer monolayer WSe_2 on 1, 2, 3, and 4 layers of A3 films and induce local point strain using the method described earlier. Figure 31 compares the strain induced by A3 films of different layers (3 samples for each layer). As expected, the induced strain that is translated to PL shift, increases with A3 film thickness. The observation also confirms that the molecules in each deposited layer of A3 undergo photoisomerization. However, we observe that

the increase in PL shift with number of layers appears to asymptote for higher number of A3 layers, possibly due to inability of A3 molecules to fully stretch with increased layers, thereby reducing the effective strain on the monolayer. Nevertheless, we could achieve a maximum effective strain of 1.4 % using four layers of A3 molecules.

A self-erasable and rewritable optoexcitonic platform

The ability to reversibly modulate the optical bandgap of monolayer WSe_2 by up to 1.4 % can be utilized to develop an optoexcitonic platform for an anti-tamper hardware system where the information is erased due to change in environmental condition (such as opening the system and exposing to light). Figure 32 demonstrates such an idea where letters *U* and *M* are sequentially written and erased on a 20 µm x 20 µm square region of monolayer WSe_2 with underlying bilayer A3. Letters are defined using a 450 nm laser (spot size ~ 2 µm) with 2 µm pixel pitch and are erased using white light irradiation. We have confirmed the repeatability of writing and erasing process over multiple samples. Such a platform can also be used to create self-destructible messages where critical information is erased at the end of expiry time.

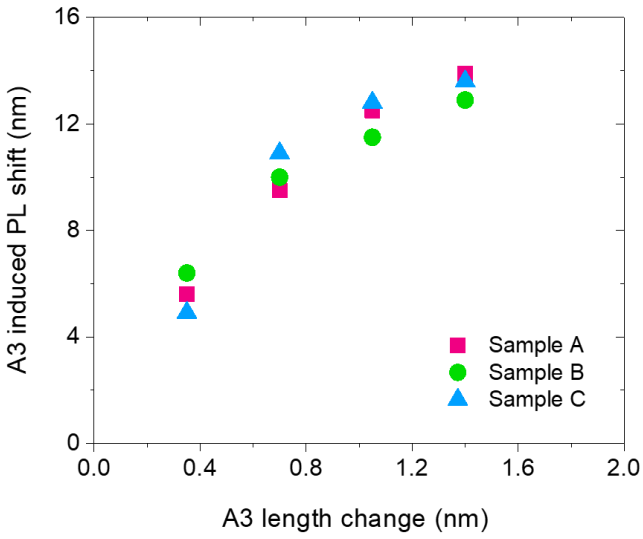

Figure 31: The strain created on monolayer WSe_2 is dependent on the thickness change of A3 films caused by photoisomerization. We compare the strains induced by A3 films of 1, 2, 3, and 4 layers (3 samples each) with the thickness of each layer switching from 0.9 nm (*trans* state) to 0.55 nm (*cis* state) or vice versa upon UV or white light treatment. A 0.7 nm height difference (bilayer) on the film produces an average of 9.5 nm PL red shift (1% tensile strain) on monolayer WSe_2. The PL shift increases with A3 film thickness, as expected. We observe that the PL shift increase starts to saturate for 3 and 4 layers of A3 films.

In summary, the work demonstrates a potential anti-tamper hardware platform based on strain engineering excitonic properties of monolayer WSe_2 using underlying thin layers of A3 molecules. The induced tensile strain can be controlled using layer by layer approach and we report effective tensile strain as high as 1.4 % for 4 layers of A3 molecules. The self-erasable and rewritable optoexcitonic platform has promising applications in self-destructible memory and anti-tamper hardware following further research on optimizing the A3 films for faster and more sensitive response. We believe that such an optoexcitonic platform can further benefit applications such as self-destruction of sensitive data over time, optical scratch pads to sensitive light detectors.

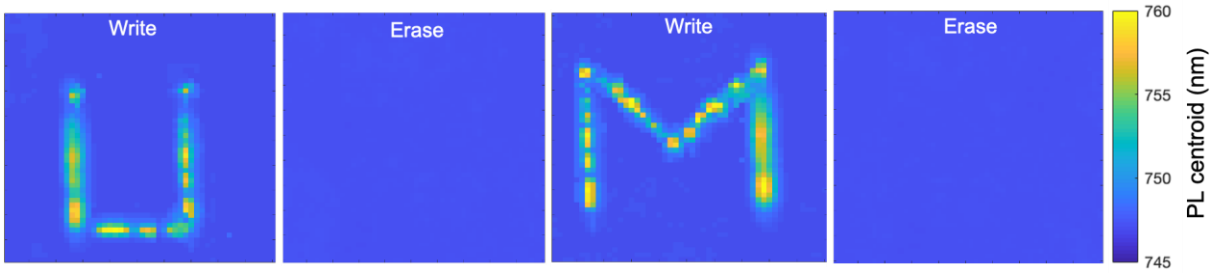

Figure 32: A demonstration of self-erasable and rewritable photonic platform that shows a writing and erasing sequence of letters U and M inscribed using the method described above on a 20 × 20 μm^2 area of monolayer WSe_2 on top of bilayer A3 films. Letters are written using 450 nm laser and are erased with 40 minutes of white light relaxation. (1) Write *U*. (2) Erase. (3) Write *M*. (4) Erase.

6 References:

1. Balar N, O'Connor BT (2017) Correlating Crack Onset Strain and Cohesive Fracture Energy in Polymer Semiconductor Films. *Macromolecules*, 50(21):8611–8618. https://doi.org/10.1021/acs.macromol.7b01282

2. Rodriquez D, Savagatrup S, Valle E, Proctor CM, McDowell C, Bazan GC, Nguyen TQ, Lipomi DJ (2016) Mechanical Properties of Solution-Processed Small-Molecule Semiconductor Films. *ACS Applied Materials and Interfaces*, 8(18):11649–11657. https://doi.org/10.1021/acsami.6b02603

3. Stafford CM, Harrison C, Beers KL, Karim A, Amis EJ, Vanlandingham MR, Kim HC, Volksen W, Miller RD, Simonyi EE (2004) A buckling-based metrology for measuring the elastic moduli of polymeric thin films. *Nature Materials*, 3(8):545–550. https://doi.org/10.1038/nmat1175

4. Tank D, Lee HH, Khang DY (2009) Elastic moduli of organic electronic materials by the buckling method. *Macromolecules*, 42(18):7079–7083. https://doi.org/10.1021/ma900137k

5. Tang CW, Vanslyke SA (1987) Organic electroluminescent diodes. *Applied Physics Letters*, 51(12):913–915. https://doi.org/10.1063/1.98799

6. Hung LS, Chen CH (2002) Recent progress of molecular organic electroluminescent materials and devices. *Materials Science and Engineering R: Reports*, 39(5–6):143–222. https://doi.org/10.1016/S0927-796X(02)00093-1

7. Kozlov VG, Bulovic V, Burrows PE, Baldo M, Khalfin VB, Parthasarathy G, Forrest SR, You Y, Thompson ME (1998) Study of lasing action based on Förster energy transfer in optically pumped organic semiconductor thin films. *Journal of Applied Physics*, 84(8):4096–4108. https://doi.org/10.1063/1.368624

8. Mori T, Mizutani T (1997) Application of energy transfer model to partially DCM-doped Alq3 light-emitting diode. *Polymers for Advanced Technologies*, 8(7):471–476. https://doi.org/10.1002/(SICI)1099-1581(199707)8:7<471::AID-PAT675>3.0.CO;2-G

9. Hoshi T, Kumagai K ichi, Inoue K, Enomoto S, Nobe Y, Kobayashi M (2008) Electronic absorption and emission spectra of Alq3 in solution with special attention to a delayed fluorescence. *Journal of Luminescence*, 128(8):1353–1358. https://doi.org/10.1016/j.jlumin.2008.01.003

10. Xiang J, Varanytsia A, Minkowski F, Paterson DA, Storey JMD, Imrie CT, Lavrentovich OD, Palffy-Muhoray P (2016) Electrically tunable laser based on oblique heliconical cholesteric liquid crystal.

Proceedings of the National Academy of Sciences of the United States of America, 113(46):12925–12928. https://doi.org/10.1073/pnas.1612212113

11. Lippert E (1955) Dipolmoment und Elektronenstruktur von angeregten Molekülen. *Zeitschrift fur Naturforschung - Section A Journal of Physical Sciences*, https://doi.org/10.1515/zna-1955-0707

12. Mataga N, Kaifu Y, Koizumi M (1956) Solvent Effects upon Fluorescence Spectra and the Dipolemoments of Excited Molecules. *Bulletin of the Chemical Society of Japan*, 29(4):465–470. https://doi.org/10.1246/bcsj.29.465

13. Onsager L (1936) Electric Moments of Molecules in Liquids. *Journal of the American Chemical Society*, https://doi.org/10.1021/ja01299a050

14. Green AP, Butler KT, Buckley AR (2013) Tuning of the emission energy of fluorophores using solid state solvation for efficient luminescent solar concentrators. *Applied Physics Letters*, 102(13)https://doi.org/10.1063/1.4799338

15. Meyer M, Mialocq JC (1987) Ground state and singlet excited state of laser dye DCM: Dipole moments and solvent induced spectral shifts. *Optics Communications*, 64(3):264–268. https://doi.org/10.1016/0030-4018(87)90390-7

16. Lippert E (1955) Dipolmoment und Elektronenstruktur von angeregten Molekülen. *Zeitschrift fur Naturforschung - Section A Journal of Physical Sciences*, 10(7):541–545. https://doi.org/10.1515/zna-1955-0707

17. Luridiana A, Pretta G, Chiriu D, Carbonaro CM, Corpino R, Secci F, Frongia A, Stagi L, Ricci PC (2016) A facile strategy for new organic white LED hybrid devices: Design, features and engineering. *RSC Advances*, https://doi.org/10.1039/c6ra00999a

18. Lakowicz JR (2006) Principles of fluorescence spectroscopy. *Principles of Fluorescence Spectroscopy*, https://doi.org/10.1007/978-0-387-46312-4

19. Rysselberghe P Van (1932) Remarks concerning the clausius-mossotti law. *Journal of Physical Chemistry*, https://doi.org/10.1021/j150334a007

20. Senturia SD (2005) Introduction. *Microsystem Design*, :3–14. https://doi.org/10.1007/0-306-47601-0_1

21. Farchioni R, Grosso G (2001) Organic Electronic Materials: Conjugted Polymers and Low Molecular

Weight Electronic Solids. https://doi.org/10.1007/978-3-642-56425-3

22. Ooshika Y (1954) Absorption Spectra of Dyes in Solution. *Journal of the Physical Society of Japan*, https://doi.org/10.1143/JPSJ.9.594

23. Madigan CF, Bulović V (2003) Solid state solvation in amorphous organic thin films. *Physical Review Letters*, 91(24):1–4. https://doi.org/10.1103/PhysRevLett.91.247403

24. Chang W, Akselrod GM, Bulović V (2015) Solid-State Solvation and Enhanced Exciton Diffusion in Doped Organic Thin Films under Mechanical Pressure. *ACS Nano*, (4):150413150541000. https://doi.org/10.1021/acsnano.5b00938

25. COMSOL Multiphysics® Modeling Software.

26. (2005) Microsystem Design. *Microsystem Design*, https://doi.org/10.1007/b117574

27. Torres JM, Bakken N, Stafford CM, Li J, Vogt BD (2010) Thickness dependence of the elastic modulus of tris(8-hydroxyquinolinato) aluminium. *Soft Matter*, https://doi.org/10.1039/c0sm00364f

28. Khang D-Y, Rogers JA, Lee HH (2009) Mechanical Buckling: Mechanics, Metrology, and Stretchable Electronics. *Advanced Functional Materials*, 19(10):1526–1536. https://doi.org/10.1002/adfm.200801065

29. Chiang CJ, Bull S, Winscom C, Monkman A (2010) A nano-indentation study of the reduced elastic modulus of Alq3 and NPB thin-film used in OLED devices. *Organic Electronics: physics, materials, applications*, 11(3):450–455. https://doi.org/10.1016/j.orgel.2009.11.026

30. Zhang YJ, Oka T, Suzuki R, Ye JT, Iwasa Y (2014) Electrically Switchable Chiral Light-Emitting Transistor. *Science*, 344(6185):725–728. https://doi.org/10.1126/science.1251329

31. Gong S-H, Alpeggiani F, Sciacca B, Garnett EC, Kuipers L (2018) Nanoscale chiral valley-photon interface through optical spin-orbit coupling. *Science (New York, N.Y.)*, 359(6374):443–447. https://doi.org/10.1126/science.aan8010

32. Chen H, Liu M, Xu L, Neshev DN (2018) Valley-selective directional emission from a transition-metal dichalcogenide monolayer mediated by a plasmonic nanoantenna. *Beilstein journal of nanotechnology*, 9:780–788. https://doi.org/10.3762/bjnano.9.71

33. Novoselov KS, Jiang D, Schedin F, Booth TJ, Khotkevich V V, Morozov S V, Geim AK (2005) Two-dimensional atomic crystals. *Proceedings of the National Academy of Sciences of the United States of*

America, 102(30):10451–3. https://doi.org/10.1073/pnas.0502848102

34. Desai SB, Seol G, Kang JS, Fang H, Battaglia C, Kapadia R, Ager JW, Guo J, Javey A (2014) Strain-induced indirect to direct bandgap transition in multilayer WSe2. *Nano Letters*, 14(8):4592–4597. https://doi.org/10.1021/nl501638a

35. Chae WH, Cain JD, Hanson ED, Murthy AA, Dravid VP (2017) Substrate-induced strain and charge doping in CVD-grown monolayer MoS2. *Applied Physics Letters*, 111(14):143106. https://doi.org/10.1063/1.4998284

36. Deotare PB, Chang W, Hontz E, Congreve DN, Shi L, Reusswig PD, Modtland B, Bahlke ME, Lee CK, Willard AP, Bulović V, Voorhis T Van, Baldo MA (2015) Nanoscale transport of charge-transfer states in organic donor–acceptor blends. *Nature Materials*, 14(11):1130–1134. https://doi.org/10.1038/nmat4424

37. Akselrod GM, Deotare PB, Thompson NJ, Lee J, Tisdale W a, Baldo M a, Menon VM, Bulović V (2014) Visualization of exciton transport in ordered and disordered molecular solids. *Nature communications*, 5:3646. https://doi.org/10.1038/ncomms4646

38. Fu X, Jacopin G, Shahmohammadi M, Liu R, Benameur M, Ganière JD, Feng J, Guo W, Liao ZM, Deveaud B, Yu D (2014) Exciton drift in semiconductors under uniform strain gradients: Application to bent ZnO microwires. *ACS Nano*, 8(4):3412–3420. https://doi.org/10.1021/nn4062353

39. Brennan KF (1999) The Physics of Semiconductors with applications to optoelectronic devices. *Cambridge University Press*,

40. Singh J (2003) Electronic and optoelectronic properties of semiconductor structures. *Cambridge University Press*, https://doi.org/10.1017/CBO9780511805745

41. Wolfe JP (1982) Thermodynamics of excitons in semiconductors. *Physics Today*, 35(17):2463–2346. https://doi.org/10.1063/1.2814656

42. Dong L, Namburu RR, O'Regan TP, Dubey M, Dongare AM (2014) Theoretical study on strain-induced variations in electronic properties of monolayer MoS2. *Journal of Materials Science*, 49(19):6762–6771. https://doi.org/10.1007/s10853-014-8370-5

43. Ruini A, Caldas MJ, Bussi G, Molinari E (2002) Solid State Effects on Exciton States and Optical Properties of PPV. *Physical Review Letters*, https://doi.org/10.1103/PhysRevLett.88.206403

44. Scheidler M, Lemmer U, Cleve B, Mahrt R, Bässler H, Göbel E, Thomas P, Kersting R, Kurz H (1996) Monte Carlo study of picosecond exciton relaxation and dissociation in poly(phenylenevinylene). *Physical Review B - Condensed Matter and Materials Physics*, https://doi.org/10.1103/PhysRevB.54.5536

45. Köhler A, Bässler H (2009) Triplet states in organic semiconductors. *Materials Science and Engineering R: Reports*, https://doi.org/10.1016/j.mser.2009.09.001

46. Luhman WA, Holmes RJ (2011) Investigation of energy transfer in organic photovoltaic cells and impact on exciton diffusion length measurements. *Advanced Functional Materials*, https://doi.org/10.1002/adfm.201001928

47. Koeppe R, Sariciftci NS (2006) Photoinduced charge and energy transfer involving fullerene derivatives. *Photochemical and Photobiological Sciences*, https://doi.org/10.1039/b612933c

48. Gong X, Lim SH, Ostrowski JC, Moses D, Bardeen CJ, Bazan GC (2004) Phosphorescence from iridium complexes doped into polymer blends. *Journal of Applied Physics*, https://doi.org/10.1063/1.1635976

49. Kawamura Y, Brooks J, Brown JJ, Sasabe H, Adachi C (2006) Intermolecular interaction and a concentration-Quenching mechanism of phosphorescent Ir(III) complexes in a solid film. *Physical Review Letters*, https://doi.org/10.1103/PhysRevLett.96.017404

50. Kalinowski J, Stampor W, Cocchi M, Virgili D, Fattori V, Marco P Di (2004) Triplet energy exchange between fluorescent and phosphorescent organic molecules in a solid state matrix. *Chemical Physics*, https://doi.org/10.1016/j.chemphys.2003.09.041

51. Kawamura Y, Yanagida S, Forrest SR (2002) Energy transfer in polymer electrophosphorescent light emitting devices with single and multiple doped luminescent layers. *Journal of Applied Physics*, https://doi.org/10.1063/1.1479751

52. Dexter DL (1953) A theory of sensitized luminescence in solids. *The Journal of Chemical Physics*, https://doi.org/10.1063/1.1699044

53. Mikhnenko O V., Cordella F, Sieval AB, Hummelen JC, Blom PWM, Loi MA (2008) Temperature dependence of exciton diffusion in conjugated polymers. *Journal of Physical Chemistry B*, 112(37):11601–11604. https://doi.org/10.1021/jp8042363

54. Fennel F, Lochbrunner S (2012) Förster-mediated spectral diffusion in disordered organic materials.

Physical Review B - Condensed Matter and Materials Physics, 85(9):1–12. https://doi.org/10.1103/PhysRevB.85.094203

55. Anni M, Caruso ME, Lattante S, Cingolani R (2006) The role of excitons' quasiequilibrium in the temperature dependence of the poly(9,9-dioctylfluorene) B phase photoluminescence. *Journal of Chemical Physics*, https://doi.org/10.1063/1.2179795

56. Bjorklund TG, Lim SH, Bardeen CJ (2001) Use of picosecond fluorescence dynamics as an indicator of exciton motion in conjugated polymers: Dependence on chemical structure and temperature. *Journal of Physical Chemistry B*, https://doi.org/10.1021/jp0124746

57. Athanasopoulos S, Hoffmann ST, Bässler H, Köhler A, Beljonne D (2013) To hop or not to hop? Understanding the temperature dependence of spectral diffusion in organic semiconductors. *Journal of Physical Chemistry Letters*, https://doi.org/10.1021/jz400480a

58. Hoffmann ST, Athanasopoulos S, Beljonne D, Bässler H, Köhler A (2012) How do triplets and charges move in disordered organic semiconductors? A Monte Carlo study comprising the equilibrium and nonequilibrium regime. *Journal of Physical Chemistry C*, https://doi.org/10.1021/jp305062p

59. Emelianova E V., Athanasopoulos S, Silbey RJ, Beljonne D (2010) 2D Excitons as primary energy carriers in organic crystals: The case of oligoacenes. *Physical Review Letters*, https://doi.org/10.1103/PhysRevLett.104.206405

60. Movaghar B, Ries B, Gŕnewald M (1986) Diffusion and relaxation of energy in disordered systems: Departure from mean-field theories. *Physical Review B*, https://doi.org/10.1103/PhysRevB.34.5574

61. Bässler H (1993) Charge Transport in Disordered Organic Photoconductors a Monte Carlo Simulation Study. *physica status solidi (b)*, https://doi.org/10.1002/pssb.2221750102

62. Athanasopoulos S, Emelianova E V., Walker AB, Beljonne D (2009) Exciton diffusion in energetically disordered organic materials. *Physical Review B - Condensed Matter and Materials Physics*, 80(19):1–7. https://doi.org/10.1103/PhysRevB.80.195209

63. Raisys S, Kazlauskas K, Daskeviciene M, Malinauskas T, Getautis V, Jursenas S (2014) Exciton diffusion enhancement in triphenylamines via incorporation of phenylethenyl sidearms. *Journal of Materials Chemistry C*, https://doi.org/10.1039/c4tc00262h

64. Menke SM, Luhman W a, Holmes RJ (2013) Tailored exciton diffusion in organic photovoltaic cells for enhanced power conversion efficiency. *Nature materials*, 12(2):152–7.

https://doi.org/10.1038/nmat3467

65. Lunt RR, Giebink NC, Belak AA, Benziger JB, Forrest SR (2009) Exciton diffusion lengths of organic semiconductor thin films measured by spectrally resolved photoluminescence quenching. *Journal of Applied Physics*, 105(5):53711. https://doi.org/10.1063/1.3079797

66. Ahn TS, Wright N, Bardeen CJ (2007) The effects of orientational and energetic disorder on Forster energy migration along a one-dimensional lattice. *Chemical Physics Letters*, https://doi.org/10.1016/j.cplett.2007.08.003

67. Mikhnenko O V., Blom PWM, Nguyen TQ (2015) Exciton diffusion in organic semiconductors. *Energy and Environmental Science*, 8(7):1867–1888. https://doi.org/10.1039/c5ee00925a

68. Wang H, Yue B, Xie Z, Gao B, Xu Y, Liu L, Sun H, Ma Y (2013) Controlled transition dipole alignment of energy donor and energy acceptor molecules in doped organic crystals, and the effect on intermolecular Förster energy transfer. *Physical Chemistry Chemical Physics*, https://doi.org/10.1039/c3cp43800g

69. Menke SM, Holmes RJ (2014) Exciton diffusion in organic photovoltaic cells. *Energy and Environmental Science*, https://doi.org/10.1039/c3ee42444h

70. Kubo T, Häusermann R, Tsurumi J, Soeda J, Okada Y, Yamashita Y, Akamatsu N, Shishido A, Mitsui C, Okamoto T, Yanagisawa S, Matsui H, Takeya J (2016) Suppressing molecular vibrations in organic semiconductors by inducing strain. *Nature Communications*, 7https://doi.org/10.1038/ncomms11156

71. Nguyen TP, Shim JH (2016) Hydrostatic pressure effect on charge transport properties of phenacene organic semiconductors. *Physical Chemistry Chemical Physics*, https://doi.org/10.1039/c6cp00127k

72. Okada Y, Sakai K, Uemura T, Nakazawa Y, Takeya J (2011) Charge transport and Hall effect in rubrene single-crystal transistors under high pressure. *Physical Review B - Condensed Matter and Materials Physics*, https://doi.org/10.1103/PhysRevB.84.245308

73. Rang Z, Haraldsson A, Kim DM, Ruden PP, Nathan MI, Chesterfield RJ, Frisbie CD (2001) Hydrostatic-pressure dependence of the photoconductivity of single-crystal pentacene and tetracene. *Applied Physics Letters*, https://doi.org/10.1063/1.1410878

74. Datta K, Deotare PB (2020) Optical Determination of Young's Modulus of Nanoscale Organic Semiconductor Thin Films for Flexible Devices. *ACS Applied Nano Materials*, 3(2):992–1001.

https://doi.org/10.1021/acsanm.9b01997

75. Bulović V, Deshpande R, Thompson M., Forrest SR (1999) Tuning the color emission of thin film molecular organic light emitting devices by the solid state solvation effect. *Chemical Physics Letters*, 308(3–4):317–322. https://doi.org/10.1016/S0009-2614(99)00580-1

76. Bulovic) CM (V. Solid State Solvation Effect. :42–45.

77. Forrest SR (2020) Organic Electronics: Foundations to Applications.

78. Sarma M, Wong KT (2018) Exciplex: An Intermolecular Charge-Transfer Approach for TADF. *ACS Applied Materials and Interfaces*, 10(23):19279–19304. https://doi.org/10.1021/acsami.7b18318

79. Monkman A (2018) Photophysics of thermally activated delayed fluorescence. *Highly Efficient OLEDs: Materials Based on Thermally Activated Delayed Fluorescence*, :425–463. https://doi.org/10.1002/9783527691722.ch12

80. Nagai M, Nozoye H (2007) Crystallization and Aggregation Processes of Vacuum-Evaporated TPD Films. *Journal of The Electrochemical Society*, https://doi.org/10.1149/1.2744137

81. Choi YH, Jeon YP, Choo DC, Kim TW (2015) Enhancement of out-coupling efficiency due to an organic scattering layer in organic light-emitting devices. *Organic Electronics*, 22:197–201. https://doi.org/10.1016/j.orgel.2015.03.044

82. Keum CM, Kronenberg NM, Murawski C, Yoshida K, Deng Y, Berz C, Li W, Wei M, Samuel IDW, Gather MC (2018) The Role of Metallic Dopants in Improving the Thermal Stability of the Electron Transport Layer in Organic Light-Emitting Diodes. *Advanced Optical Materials*, 6(17):1–8. https://doi.org/10.1002/adom.201800496

83. Fuhrmann DA, Wixforth A, Curran A, Morrod JK, Prior KA, Warburton RJ, Ebbecke J (2009) Surface acoustic wave mediated exciton dissociation in a ZnCdSe/ LiNbO 3 hybrid. *Applied Physics Letters*, https://doi.org/10.1063/1.3136862

84. Zhuravlev KS, Gilinskiĭ AM, Tsarev A V., Nikolaenko AE (2001) Photoluminescence kinetics in GaAs under the influence of surface acoustic waves. *Semiconductors*, https://doi.org/10.1134/1.1393023

85. Gulyaev D V., Toropov AI, Zhuravlev KS (2007) Effect of an electric field on photoluminescence kinetics of type II GaAs/AlAs superlattices. *AIP Conference Proceedings*, https://doi.org/10.1063/1.2729945

86. Homan SB, Sangwan VK, Balla I, Bergeron H, Weiss EA, Hersam MC (2017) Ultrafast exciton dissociation and long-lived charge separation in a photovoltaic pentacene-MoS2van der Waals heterojunction. *Nano Letters*, 17(1):164–169. https://doi.org/10.1021/acs.nanolett.6b03704

87. Zheng YJ, Huang YL, Chen Y, Zhao W, Eda G, Spataru CD, Zhang W, Chang YH, Li LJ, Chi D, Quek SY, Wee ATS (2016) Heterointerface Screening Effects between Organic Monolayers and Monolayer Transition Metal Dichalcogenides. *ACS Nano*, 10(2):2476–2484. https://doi.org/10.1021/acsnano.5b07314

88. Lee J-H, Min C-K, Joo T (2001) Ultrafast optical dynamics of excitons in J-aggregates Optical dynamics of excitons in aggregates of a carbocyanine dye Ultrafast optical dynamics of excitons in J-aggregates. *The Journal of Chemical Physics*, 1141(10)https://doi.org/10.1063/1.1329133،

89. Castellanos-Gomez A, Quereda J, Meulen HP van der, Agraït N, Rubio-Bollinger G (2016) Spatially resolved optical absorption spectroscopy of single- and few-layer MoS $_2$ by hyperspectral imaging. *Nanotechnology*, 27(11):115705. https://doi.org/10.1088/0957-4484/27/11/115705

90. Prins F, Goodman AJ, Tisdale WA (2014) Reduced dielectric screening and enhanced energy transfer in single- and few-layer MoS2. *Nano Letters*, 14(11):6087–6091. https://doi.org/10.1021/nl5019386

91. Chernikov A, Berkelbach TC, Hill HM, Rigosi A, Li Y, Aslan OB, Reichman DR, Hybertsen MS, Heinz TF (2014) Exciton Binding Energy and Nonhydrogenic Rydberg Series in Monolayer WS2. *Physical Review Letters*, 113(7):076802. https://doi.org/10.1103/PhysRevLett.113.076802

92. Clapp AR, Medintz IL, Mattoussi H (2006) Förster resonance energy transfer investigations using quantum-dot fluorophores. *European journal of chemical physics and physical chemistry*, 7(1):47–57. https://doi.org/10.1002/cphc.200500217

93. Medintz IL, Mattoussi H (2009) Quantum dot-based resonance energy transfer and its growing application in biology. *Physical chemistry chemical physics : PCCP*, 11(1):17–45. https://doi.org/10.1039/b813919a

94. Shirasaki Y, Anikeeva PO, Tischler JR, Scott Bradley M, Bulović V (2010) Efficient F??rster energy transfer from phosphorescent organic molecules to J-aggregate thin films. *Chemical Physics Letters*, 485(1–3):243–246. https://doi.org/10.1016/j.cplett.2009.12.017

95. Blum C, Zijlstra N, Lagendijk A, Wubs M, Mosk AP, Subramaniam V, Vos WL (2012) Nanophotonic control of the förster resonance energy transfer efficiency. *Physical Review Letters*,

109(20):1–5. https://doi.org/10.1103/PhysRevLett.109.203601

96. Mak KF, Lee C, Hone J, Shan J, Heinz TF (2010) Atomically thin MoS2: A new direct-gap semiconductor. *Physical Review Letters*, 105(13)https://doi.org/10.1103/PhysRevLett.105.136805

97. Bradley MS, Tischler JR, Bulović V (2005) Layer-by-layer J-aggregate thin films with a peak absorption constant of 106 cm-1. *Advanced Materials*, 17(15):1881–1886. https://doi.org/10.1002/adma.200500233

98. Zhou D, Piper JD, Abell C, Klenerman D, Kang D-J, Ying L (2005) Fluorescence resonance energy transfer between a quantum dot donor and a dye acceptor attached to DNA. *Chemical communications (Cambridge, England)*, (38):4807–9. https://doi.org/10.1039/b508911e

99. Murphy CB, Zhang Y, Troxler T, Ferry V, Martin JJ, Jones WE (2004) Probing Förster and Dexter Energy-Transfer Mechanisms in Fluorescent Conjugated Polymer Chemosensors. *The Journal of Physical Chemistry B*, 108(5):1537–1543. https://doi.org/10.1021/jp0301406

100. Shastry TA, Balla I, Bergeron H, Amsterdam SH, Marks TJ, Hersam MC (2016) Mutual Photoluminescence Quenching and Photovoltaic Effect in Large-Area Single-Layer MoS2-Polymer Heterojunctions. *ACS Nano*, 10(11):10573–10579. https://doi.org/10.1021/acsnano.6b06592

101. Mak KF, He K, Lee C, Lee GH, Hone J, Heinz TF, Shan J (2013) Tightly bound trions in monolayer MoS 2. *Nature Materials*, 12(3):207–211. https://doi.org/10.1038/nmat3505

102. Li Z, Ye R, Feng R, Kang Y, Zhu X, Tour JM, Fang Z (2015) Graphene Quantum Dots Doping of MoS_2 Monolayers. *Advanced Materials*, 27(35):5235–5240. https://doi.org/10.1002/adma.201501888

103. Matsukura Y, Uchiyama Y, Yamashita H, Nishino H, Fujii T (2009) Responsivity-dark current relationship of quantum dot infrared photodetectors (QDIPs). *Infrared Physics and Technology*, 52(6):257–259. https://doi.org/10.1016/j.infrared.2009.05.023

104. Matsukura Y, Uchiyama Y, Yamashita H, Nishino H, Fujii T (2009) Responsivity-dark current relationship of quantum dot infrared photodetectors (QDIPs). *Infrared Physics and Technology*, 52(6):257–259. https://doi.org/10.1016/j.infrared.2009.05.023

105. Furchi MM, Polyushkin DK, Pospischil A, Mueller T (2014) Mechanisms of photoconductivity in atomically thin MoS2. *Nano Letters*, 14(11):6165–6170. https://doi.org/10.1021/nl502339q

106. Dean CR, Young AF, Meric I, Lee C, Wang L, Sorgenfrei S, Watanabe K, Taniguchi T, Kim P,

Shepard KL, Hone J (2010) Boron nitride substrates for high-quality graphene electronics. *Nature Nanotechnology*, 5(10):722–726. https://doi.org/10.1038/nnano.2010.172

107. Henck H, Pierucci D, Fugallo G, Avila J, Cassabois G, Dappe YJ, Silly MG, Chen C, Gil B, Gatti M, Sottile F, Sirotti F, Asensio MC, Ouerghi A (2017) Direct observation of the band structure in bulk hexagonal boron nitride. *Physical Review B*, 95(8):1–6. https://doi.org/10.1103/PhysRevB.95.085410

108. Shirasaki Y, Anikeeva PO, Tischler JR, Scott Bradley M, Bulović V (2010) Efficient Forster energy transfer from phosphorescent organic molecules to J-aggregate thin films. *Chemical Physics Letters*, 485(1–3):243–246. https://doi.org/10.1016/j.cplett.2009.12.017

109. Moll J, Daehne S, Durrant JR, Wiersma DA (1995) Optical dynamics of excitons in J aggregates of a carbocyanine dye. *The Journal of Chemical Physics*, 102(16):6362–6370. https://doi.org/10.1063/1.1703017

110. Walczewska-Szewc K, Corry B (2014) Accounting for dye diffusion and orientation when relating FRET measurements to distances: three simple computational methods. *Phys. Chem. Chem. Phys.*, 16(24):12317–12326. https://doi.org/10.1039/C4CP01222D

111. Dale RE, Eisinger J, Blumberg WE (1979) The orientation freedom of molecular probes. *Biophys. J.*, 26:161–93.

112. Steinberg IZ (1971) Long-range nonradiative transfer of electronic excitation energy in proteins and polypeptides. *Annual review of biochemistry*, 40:83–114. https://doi.org/10.1146/annurev.bi.40.070171.000503

113. Ploetz E, Lerner E, Husada F, Roelfs M, Chung S, Hohlbein J, Weiss S, Cordes T (2016) Förster resonance energy transfer and protein-induced fluorescence enhancement as synergetic multi-scale molecular rulers. *Scientific Reports*, 6(August):1–18. https://doi.org/10.1038/srep33257

114. Stöferle T, Mahrt RF (2009) Energy transfer in hybrid organic/inorganic nanocomposites. :73930C. https://doi.org/10.1117/12.825256

115. Zhu T, Yuan L, Zhao Y, Zhou M, Wan Y, Mei J, Huang L (2018) Highly mobile charge-transfer excitons in two-dimensional WS2/tetracene heterostructures. *Science Advances*, 4(1):1–9. https://doi.org/10.1126/sciadv.aao3104

116. Hong X, Kim J, Shi S-F, Zhang Y, Jin C, Sun Y, Tongay S, Wu J, Zhang Y, Wang F (2014) Ultrafast charge transfer in atomically thin MoS2/WS2 heterostructures. *Nature Nanotechnology*,

9(9):682–686. https://doi.org/10.1038/nnano.2014.167

117. Petoukhoff CE, Krishna MBM, Voiry D, Bozkurt I, Deckoff-Jones S, Chhowalla M, O'Carroll DM, Dani KM (2016) Ultrafast Charge Transfer and Enhanced Absorption in MoS2-Organic van der Waals Heterojunctions Using Plasmonic Metasurfaces. *ACS Nano*, 10(11):9899–9908. https://doi.org/10.1021/acsnano.6b03414

118. Zhu T, Yuan L, Zhao Y, Zhou M, Wan Y, Mei J, Huang L (2018) Highly mobile charge-transfer excitons in two-dimensional WS $_2$ /tetracene heterostructures. *Science Advances*, 4(1):eaao3104. https://doi.org/10.1126/sciadv.aao3104

119. Renshaw CK, Forrest SR (2014) Excited state and charge dynamics of hybrid organic/inorganic heterojunctions. I. Theory. *Physical Review B - Condensed Matter and Materials Physics*, 90(4):1–15. https://doi.org/10.1103/PhysRevB.90.045302

120. Kulig M, Zipfel J, Nagler P, Blanter S, Schüller C, Korn T, Paradiso N, Glazov MM, Chernikov A (2018) Exciton Diffusion and Halo Effects in Monolayer Semiconductors. *Physical Review Letters*, 120(20):207401. https://doi.org/10.1103/PhysRevLett.120.207401

121. Cordovilla Leon DF, Li Z, Jang SW, Cheng CH, Deotare PB (2018) Exciton transport in strained monolayer WSe 2. *Applied Physics Letters*, 113(25)https://doi.org/10.1063/1.5063263

122. Bouchaud J-P, Georges A (1990) Anomalous diffusion in disordered media: Statistical mechanisms, models and physical applications. *Physics Reports*, 195(4–5):127–293. https://doi.org/10.1016/0370-1573(90)90099-N

123. Cordovilla Leon DF, Li Z, Jang SW, Deotare PB (2019) Hot exciton transport in WS e2 monolayers. *Physical Review B*, 100(24):1–6. https://doi.org/10.1103/PhysRevB.100.241401

124. Sun D, Rao Y, Reider GA, Chen G, You Y, Brézin L, Harutyunyan AR, Heinz TF (2014) Observation of rapid exciton-exciton annihilation in monolayer molybdenum disulfide. *Nano Letters*, 14(10):5625–5629. https://doi.org/10.1021/nl5021975

125. Kaasbjerg K, Bhargavi KS, Kubakaddi SS (2014) Hot-electron cooling by acoustic and optical phonons in monolayers of MoS2 and other transition-metal dichalcogenides. *Physical Review B*, 90(16):165436. https://doi.org/10.1103/PhysRevB.90.165436

126. Nie Z, Long R, Teguh JS, Huang CC, Hewak DW, Yeow EKL, Shen Z, Prezhdo O V., Loh ZH (2015) Ultrafast Electron and Hole Relaxation Pathways in Few-Layer MoS2. *Journal of Physical*

Chemistry C, 119(35):20698–20708. https://doi.org/10.1021/acs.jpcc.5b05048

127. Miller B, Lindlau J, Bommert M, Neumann A, Yamaguchi H, Holleitner A, Högele A, Wurstbauer U (2019) Tuning the Fröhlich exciton-phonon scattering in monolayer MoS 2. *Nature Communications*, 10(1)https://doi.org/10.1038/s41467-019-08764-3

128. Sohier T, Calandra M, Mauri F (2016) Two-dimensional Fröhlich interaction in transition-metal dichalcogenide monolayers: Theoretical modeling and first-principles calculations. *Physical Review B*, 94(8):1–13. https://doi.org/10.1103/PhysRevB.94.085415

129. Chow CM, Yu H, Jones AM, Schaibley JR, Koehler M, Mandrus DG, Merlin R, Yao W, Xu X (2017) Phonon-assisted oscillatory exciton dynamics in monolayer MoSe2. *npj 2D Materials and Applications*, 1(1):33. https://doi.org/10.1038/s41699-017-0035-1

130. Sengupta A, Chanana A, Mahapatra S (2015) Phonon scattering limited performance of monolayer MoS2 and WSe2 n-MOSFET. *AIP Advances*, 5(2)https://doi.org/10.1063/1.4907697

131. Miyata K, Meggiolaro D, Tuan Trinh M, Joshi PP, Mosconi E, Jones SC, Angelis F De, Zhu XY (2017) Large polarons in lead halide perovskites. *Science Advances*, 3(8)https://doi.org/10.1126/sciadv.1701217

132. Kaasbjerg K, Thygesen KS, Jacobsen KW (2012) Phonon-limited mobility in n-type single-layer MoS 2 from first principles. *Physical Review B - Condensed Matter and Materials Physics*, 85(11):1–16. https://doi.org/10.1103/PhysRevB.85.115317

133. You A, Be MAY, In I (2017) Polarons. 3(August 2003)

134. Zheng F, Wang LW (2019) Large polaron formation and its effect on electron transport in hybrid perovskites. *Energy and Environmental Science*, 12(4):1219–1230. https://doi.org/10.1039/c8ee03369b

135. Feynman 1918-1988. RP (Richard P (1998) Statistical mechanics : a set of lectures. *Statistical mechanics : a set of lectures*, (Boulder, Colo. :)

136. Leburton JP (1984) Size effects on polar optical phonon scattering of 1-D and 2-D electron gas in synthetic semiconductors. *Journal of Applied Physics*, 56(10):2850–2855. https://doi.org/10.1063/1.333820

137. Yang Y, Ostrowski DP, France RM, Zhu K, Lagemaat J Van De, Luther JM, Beard MC (2016) Observation of a hot-phonon bottleneck in lead-iodide perovskites. *Nature Photonics*, 10(1):53–59.

https://doi.org/10.1038/nphoton.2015.213

138. Yang J, Wen X, Xia H, Sheng R, Ma Q, Kim J, Tapping P, Harada T, Kee TW, Huang F, Cheng YB, Green M, Ho-Baillie A, Huang S, Shrestha S, Patterson R, Conibeer G (2017) Acoustic-optical phonon up-conversion and hot-phonon bottleneck in lead-halide perovskites. *Nature Communications*, 8https://doi.org/10.1038/ncomms14120

139. Hussain SA, Dey B, Bhattacharjee D, Mehta N (2018) Unique supramolecular assembly through Langmuir – Blodgett (LB) technique. *Heliyon*, 4(12):e01038. https://doi.org/10.1016/j.heliyon.2018.e01038

140. Aslan OB, Deng M, Heinz TF (2018) Strain tuning of excitons in monolayer WSe2. *Physical Review B*, 98(11):115308. https://doi.org/10.1103/PhysRevB.98.115308

141. Conley HJ, Wang B, Ziegler JI, Haglund RF, Pantelides ST, Bolotin KI (2013) Bandgap Engineering of Strained Monolayer and Bilayer MoS2. *Nano Letters*, 13(8):3626–3630. https://doi.org/10.1021/nl4014748

142. Lloyd D, Liu X, Christopher JW, Cantley L, Wadehra A, Kim BL, Goldberg BB, Swan AK, Bunch JS (2016) Band Gap Engineering with Ultralarge Biaxial Strains in Suspended Monolayer MoS2. *Nano Letters*, 16(9):5836–5841. https://doi.org/10.1021/acs.nanolett.6b02615

143. Li Y, Wang T, Wu M, Cao T, Chen Y, Sankar R, Ulaganathan RK, Chou F, Wetzel C, Xu CY, Louie SG, Shi SF (2018) Ultrasensitive tunability of the direct bandgap of 2D InSe flakes via strain engineering. *2D Materials*, 5(2)https://doi.org/10.1088/2053-1583/aaa6eb

144. Nguyen DA, Oh HM, Duong NT, Bang S, Yoon SJ, Jeong MS (2018) Highly Enhanced Photoresponsivity of a Monolayer WSe2 Photodetector with Nitrogen-Doped Graphene Quantum Dots. *ACS Applied Materials and Interfaces*, 10(12):10322–10329. https://doi.org/10.1021/acsami.7b18419

145. Wang Y, Slassi A, Stoeckel MA, Bertolazzi S, Cornil J, Beljonne D, Samorì P (2019) Doping of Monolayer Transition-Metal Dichalcogenides via Physisorption of Aromatic Solvent Molecules. *Journal of Physical Chemistry Letters*, 10(3):540–547. https://doi.org/10.1021/acs.jpclett.8b03697

146. Li J, Wierzbowski J, Ceylan Ö, Klein J, Nisic F, Anh T Le, Meggendorfer F, Palma CA, Dragonetti C, Barth J V., Finley JJ, Margapoti E (2014) Tuning the optical emission of MoS2 nanosheets using proximal photoswitchable azobenzene molecules. *Applied Physics Letters*, 105(24)https://doi.org/10.1063/1.4904824

147. Kim M, Safron NS, Huang C, Arnold MS, Gopalan P (2012) Light-driven reversible modulation of doping in graphene. *Nano Letters*, 12(1):182–187. https://doi.org/10.1021/nl2032734